Characterization of lambda systems using superconducting qubits

by

Helen Percival

A thesis
presented to the University of Waterloo
in fulfillment of the
thesis requirement for the degree of
Master of Applied Science
in
Electrical and Computer Engineering

Waterloo, Ontario, Canada, 2017

I hereby declare that I am the sole author of this thesis. This is a true copy of the thesis, including any required final revisions, as accepted by my examiners.

I understand that my thesis may be made electronically available to the public.

Abstract

Lambda systems, with a metastable state in addition to the ground state, naturally occur in many atomic systems. Atomic lambda systems offer many potential applications in quantum information processing including single photon transistors and quantum memories [26][14][5][30]. In superconducting qubits, ladder type systems are most common, useful lambda systems, however, have remained elusive. An effective lambda system was created, formed from the Jaynes-Cummings dressed states of a superconducting qubit-cavity system. Using two-photon driving, the system can be controlled as a conventional lambda system. The performance of the device is characterized to determine the suitability of it for various applications, including the single photon regime.

A model was developed to investigate the effects of detuned two-photon drive. This model restricts the cavity-qubit system to only the three levels that are used in the lambda system. In the time domain, the drives interfere. Only when the drives are detuned by the same amount in opposite directions do they not interfere and the coupler invokes the transistion it is driving.

In this experiment, a 3D transmon was placed in a superconducting aluminum cavity with a decay rate $\kappa = 0.25$MHz. Qubit characterization demonstrate that the transmon has $T_1 = 17\mu$s and $T_2 = 35\mu$s. From this, the decay rate of the qubit was calculated to be $=62.5$Hz, indicating the system has $\kappa \gg \Gamma$, which is necessary to form an effective lambda system.

Using the two drives, it was shown that the detuning of the two-photon driving is linear. Holding one of these drives constant in frequency and drive power, it was demonstrated that the detuned frequency of the second drive changes quadratically with its drive amplitude. Suitability of the system to the single photon regime was investigated by using the two detuned drives: a strong, continuous wave drive, and a weaker, pulsed drive. Decreasing the pulsed drive amplitude, it was shown that the metastable state can be populated a pulse of only 3700 photons, suggesting with better signal isolation, and quantum-noise-limited signal amplification, the single photon regime may be achieved.

Acknowledgements

I would like to thank Vadiraj A. M. for the design and fabrication of the device used for these experiments, and Sandbo Chang for fabricating the essential Josephson junction. I would also like to thank the rest of our research group, EQSL, for support throughout my project, especially Pol Forn-Diaz whose help and guidance was invaluable.

My supervisor, Christopher Wilson, for always having his door open for discussion and the long nights debugging experiments. His explanations were essential to my understanding.

To my officemates, Chris Warren and Guillaume Verdon-Akzam, thank you for letting me bounce ideas off of them and for the distractions on long days.

Lastly, I would like to thank my parents for all the love, support, and food they gave me.

Table of Contents

List of Tables

List of Figures

List of Abbreviations

ATS Aulters-Townes splitting

BCS Bardeen, Cooper and Schrieffer

BJT bipolar junction transistor

BW bandwidth

CPB Cooper pair box

CPT coherent population trapping

cQED circuit quantum electrodynamics

DIT dipole induced transparency

EIT electromagnetically induced transparency

EM electromagnetic

FWHM full-width, half-max

JJ Josephson Junction

QI quantum information

QS QuickSyn

RWA Rotating Wave Approximation

SC superconducting

SHO simple harmonic oscillator

TLS two-level quantum system

List of Symbols

C_J Parasitic capacitance of a Josephson Junction

Δ_p Probe frequency detuning

Δ_c Coupler frequency detuning

E_C Charging energy

E_F Fermi energy

E_J Josephson energy

Γ_1 Relaxation rate

Γ_2 Dephasing rate

Γ_ϕ Pure dephasing rate

G Gain of the lambda system transistor

H Hamiltonian

I_C Superconducting critical current

I_S Supercurrent

L_J Inductance of a Josephson Junction

Ω_p Probe Rabi drive frequency

Ω_c Coupler Rabi drive frequency

Q Quality factor

T_1 Relaxation time

T_2^* Dephasing time

T_2 Pure dephasing time

T_C Superconducting transition temperature

T_F Fermi temperature

$\hat{a}^\dagger$ Creation operator

α Anharmonicity

$\hat{a}$ Annihilation operator

χ Dispersive shift in cavity resonance frequency due to qubit state

ϵ_m Charge dispersion

Γ Decay rate of the qubit

g Coupling between the qubit and cavity

$\hbar$ Reduced Planck's constant

k_B Boltzmann constant

κ Decay rate of the cavity

$\mathbf{k}$ Wave vector

Ψ Macroscopic wavefuntion

n_g Number of charges on the superconducting island in a Cooper Pair Box

ω_D DeBye frequency

ω_{bare} Cavity resonance frequency without shift due to presence of qubit

ω_{cav} Radial frequency of the cavity

$\omega_{control}$ Frequency of signal controlled by the lambda system transistor

ω_p Probe frequency: transition between $|e,0\rangle \leftrightarrow |e,1\rangle$

ω_c Coupler frequency: transition between $|g,0\rangle \leftrightarrow |e,1\rangle$

ω_{qb} Radial frequency of the qubit

R Reflection coefficient

Chapter 1

Introduction

Lambda systems are common in atomic physics. The characteristic metastable state leads to many interesting constructs, including single photon transistors and single photon detectors. Unfortunately, in circuit quantum electrodynamics (cQED) lambda systems are uncommon. Instead ladder systems are prevalent, offering precise control, but not the opportunity for population inversion that is characteristic to the decay rates in lambda system.

Following the work of Palmer's group [42], a lambda system was created using a combined cavity-qubit system. Using the relative decay rates of the cavity and the qubit the life-time of one of the excited states a state significantly longer than the other, forming a metastable state. It is this metastable state in atomic systems which creates the interference phenomena seen in semi-classical effects such as electromagnetically induced transparency (EIT) [2]. When the atomic system is replaced with a single-dipole emitter, such as a qubit, the same interference phenomena is seen, and is named dipole induced transparency (DIT) [58].

Using a transmon as the qubit in the system provides interesting opportunities to investigate other characteristics of a lambda system. As the transmon requires that the transition from the ground to the highest excited state of the lambda system be a two-photon transition, opportunities to investigate detuning the drive frequencies from the two-photon transition. Driving these detuned drives at different powers, offers the possibility of controlling the system with a single photon.

A model developed to simulate the time dynamics of the detuned probe drive. It is completed by restricting the space to only the states used in the lambda system.

1.1 Motivation

Although single photon detectors are common in optics, there is not a working detector for the microwave regime. One, using a lambda system has been proposed by Inomata et al [26]. This one, however, relies on knowing the time at which the photon will arrive. Here, we propose another system, also using a lambda system, that could be used for single photon detection.

The proposed system uses a single photon transistor to use a single photon to alter the transmission magnitude of a continuous-wave microwave signal. The probe drive acts as the gate of the transistor, shifting the system to the metastable state of the lambda system. When the system is in the metastable state it changes the magnitude of a second, continiously drive signal, the probe.

In this system, the probe is a two-photon transition. This allows for the the transition to be detuned. Each of these detuned drives on their own, do not invoke the transition, but together when driven simultaneously they will. It is predicted that as long as one of the detuned is continually driven hard enough the other drive can be reduced to a single photon.

Due to the lifetime of the metastable state, even a single photon will cause the system to sit in the metastable state for longer than the lifetime of the photon in the system. Therefore, the change in the magnitude of the transmission of the coupleris long enough to be detectable.

In this experiment, the effects of detuning the two photon drive is investigated, including the dependencies of the frequencies on the powers of the microwave drives to explore the feasibility of a detuned microwave transistor. Furthermore, to determine the feasibility of a single photon transistor and detector, the limits of ratios of the detuned drives are explored.

1.2 Quantum Information

Quantum information (QI) promises exponential speedup for certian complex tasks. Some of these, such as factoring, have implications in computer security, providing a major motivation to implement large scale QI systems. Classical bits store information in discrete states of 1s and 0s. QI is a superposition of these states $|\psi\rangle = \alpha\,|0\rangle + \beta\,|1\rangle$ where α and β are normalized as $\alpha^2 + \beta^2 = 1$ [31]. With classical bits, n bits would be needed to be

able to store the state to n precision. This is both inefficient and impractical; even with unlimited memory and time resources.

Instead, using a quantum system which can be mapped into a two-dimensional Hilbert space, the state can be stored on only one quantum bit or qubit. The superposition of the qubit allows for probabilistic algorithms to be run - non-deterministic algorithms that produce the correct answer only some of the time. Although they need to be run multiple times to gain the correct answer with any certainty, they still run much faster than classical algorithms.

1.3 Superconductivity

With the liquification of 4He came the ability to cool materials down to a few Kelvin and the discovery of superconductivity. Materials with this property are marked by near perfect conductivity. Although most superconductors have transition temperatures (T_C) in the 1-10 Kelvin range, more were later discovered in 1986 with much higher transition temperatures [7]. These high temperature superconductors are not fully understood or described by theory, while the low temperature ones have been well described by the theory proposed by Bardeen, Cooper and Schrieffer in 1956; the Bardeen, Cooper and Schrieffer (BCS) theory [6].

Superconductors described by the BCS theory are widely used in circuit quantum electrodynamics. They have low microwave loss and can be used to make resonators with very high quality factors (Q) [57][37][50][38][55]; current experiments have shown resonators with quality factors of up to 1 million [57]. The Q can be easily controlled through the coupling of the cavity to the transmission line allowing for control of the design of the system. The standardization of fabrication processes, makes them an approachable quantum system.

Chapter 2

Theoretical Background

2.1 Superconductivity

BCS Thoery

Superconductors can be understood by knowing that at $T = 0K$ electrons form a different ground state than in normal metals. Instead of using the Fermi gas model [56], an electron cloud with non-interacting particles, the theory includes weak attractive interactions between pairs of electrons. This pairing leads to the energy gap, $\Delta \sim k_B T_C \propto \hbar\omega_D$ (k_B is the Boltzmann constant, $\hbar$ is the reduced Planck's constand, and ω_D is the DeBye frequency), seen in the excitation spectrum.

Since, in the Fermi gas model, electrons are fermions, with spin $1/2$, with non-interacting particles one electron can occupy each single particle energy level and the ground state is found by placing electrons in states denoted by increasing integer wave vector, $\mathbf{k}$. The largest energy state occupied, the Fermi energy, is therefore $E_F = \hbar r^2 \mathbf{k}_F^2 / 2m$ where m is the mass of the electron and $\mathbf{k}_F$ is the wave vector of the largest state occupied. This energy defines the Fermi temperature,

$$T_F = \frac{E_F}{k_B} \tag{2.1}$$

In $\mathbf{k}$ space, the total number of electrons is

$$N_{el}(\mathbf{k_F}, V) = 2\frac{\frac{4\pi}{3}\mathbf{k_F}^3}{\frac{(2\pi)^3}{V}} \tag{2.2}$$

where the volume V is defined by the dimensions of a parallelepiped, $V = {(2\pi)^3}/{(L_1 L_2 L_3)}$.

Taking spin degeneracy into account, the number of electrons in terms of energy becomes

$$N_{el}(E, V) = 2\frac{\frac{4\pi}{3}\left(\frac{2mE}{\hbar^2}\right)^{\frac{3}{2}}}{\frac{(2\pi)^3}{V}} \tag{2.3}$$

When a weak attractive potential is added, and the temperature is much lower than the Fermi temperature ($T \ll T_F$), the electrons pair in states $|\mathbf{k}\uparrow\rangle$ and $|\mathbf{k}\downarrow\rangle$. These pairs can only form on the surface of the Fermi surface: the two-body wave function, $g(\mathbf{k})$, is 0 for $|\mathbf{k}| < \mathbf{k}_F$. Using the Schrodinger equation for two particles interactive via an attractive potential, V, with 0 centre of mass momentum, the binding energy of the state is given by

$$E \simeq -2\hbar\omega_D e^{-{2}/{N(0)V}} \tag{2.4}$$

where $N(0)$ is the density of states when ${\hbar^2\mathbf{k}^2}/{2m} - E_F = 0$. Since the energy is negative, the pair forms a bound state; the ground state of a degenerate ($T \ll T_F$) Fermi gas is unstable to the formation of Cooper pairs. As most superconductors have Fermi temperatures on the order of $10^4 K$ [25] at low temperatures this condition can easily be achieved.

This result then can be applied to a macroscopic number of Cooper pairs. With a thermal distribution of these pairs, moving at a thermal distribution of momenta, the energy gap is wiped out. To maintain the gap in excitation spectrum, the Cooper pairs must all have a very small momentum; the superconducting material must be at very low temperatures and the Cooper pairs must form a Bose-Einstein condensate.

By choosing a new ground state which preserves this pairing, Bardeen, Cooper and Schrieffer created a working model for most low temperature superconductors [6]. It defined the macroscopic wave function of the condensate in superconductor at a specific location ($r = (x, y, z)$) and time in space [43]

$$\Psi(\mathbf{r}, t) = |\Psi(\mathbf{r}, t)|e^{i\theta(\mathbf{r},t))} = \sqrt{n(\mathbf{r}, t)}e^{i\theta(\mathbf{r},t)} \tag{2.5}$$

which defined by the density of Cooper Pairs, $n(\mathbf{r}, t)$, and phase, $\theta(\mathbf{r}, t)$.

Josephson Junction

If a weak link, a thin barrier layer of insulator, normal material or a narrow section of superconductor, is placed between two pieces of superconductor as in Figure 2.1, a useful effect is shown. This type of structure is called a Josephson Junction (JJ).

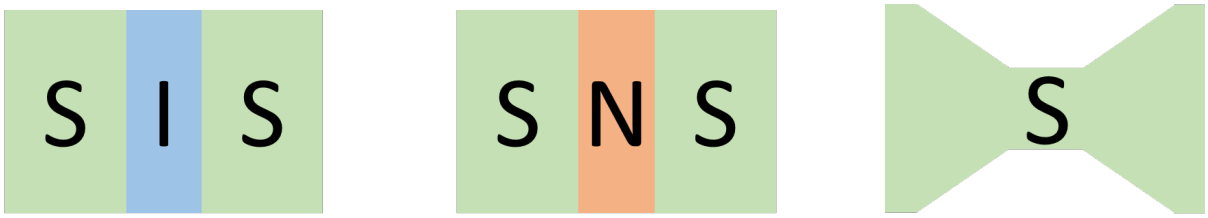

(a) (b) (c)

Figure 2.1: Superconducting weak links. **(a)** superconducting-insulator-superconducting **(b)** superconducting-normal-superconducting **(c)** superconducting microbridge.

Using the macroscopic wave function, Equation 2.5, as long as the barrier layer is thin, it can be seen that the wave functions of the two superconductors can overlap. This allows Cooper Pairs to tunnel across the barrier and a current to flow.

To quantify the effect of the weak connection, like any other electronic component the relationship between the current and voltage is examined. B.D. Josephson first made a set of predictions for the behaviour of the current and voltage in the structures in 1962 [29].

His first prediction was there is a dissipationless supercurrent (I_S) that can flow through the weak link due to tunneling of Cooper pairs, described by a critical current I_C.

$$I_S = I_C \sin\phi \tag{2.6}$$

where ϕ is the phase difference between the two superconductors, $\phi = \theta_2 - \theta_1$. The critical current is dependent on the material, barrier thickness and barrier surface size. It sets the maximum supercurrent that can flow through the superconductor without setting up a voltage differential. The voltage is then proportional to the time variance of the phase difference between the two superconductors.

$$\frac{d\phi}{dt} = \frac{2\pi}{\Phi_0} V \tag{2.7}$$

Defining $\Phi_0 = {}^{h}/_{2|e|}$, the Josephson inductance $L_J = {}^{\Phi_0}/_{2\pi I_c}$ can be introduced. The relation ${}^{h}/_{2|e|}$ comes from the charge of the Cooper pair, $2e$. The inductance stores an energy, the Josephson energy, just as any other inductor:

$$E_J = \frac{\Phi_0 I_C}{2\pi}(1 - \cos\phi) \tag{2.8}$$

Due to the parallel configuration of the superconducting surfaces, a capacitor is formed. The capacitor is also able to store energy, which is defined as

$$E_C = \frac{e^2}{2C_J} \tag{2.9}$$

where C_J is the capacitance of the junction. The Josephson and capacitive energies of the JJ are essential in the design of a qubit.

Using a canonical quantization and Kirchhoff's laws, the Hamiltonian of an isolated JJ can be defined:

$$H = \frac{1}{2}\frac{1}{C}p_\phi^2 + \frac{(\frac{\Phi_0}{2\pi})^2}{L_J}(1 - \cos\phi) \tag{2.10}$$

This gives us a washboard potential, periodic with ϕ.

A non-ideal JJ is modeled by a junction shunted by a capacitor and a resistor, Figure 2.2. Three currents flow through the junction: the tunneling current ($I_J = I_c \sin\phi$), the current through the capacitor ($I_c = \frac{d}{dt}(CV)$) and the resistive current ($I_R = \frac{V}{R}$). Adding a current source I_B the following equation is obtained:

$$I_B = I_C \cos\phi + \frac{d}{dt}(CV) + \frac{V}{R} \tag{2.11}$$

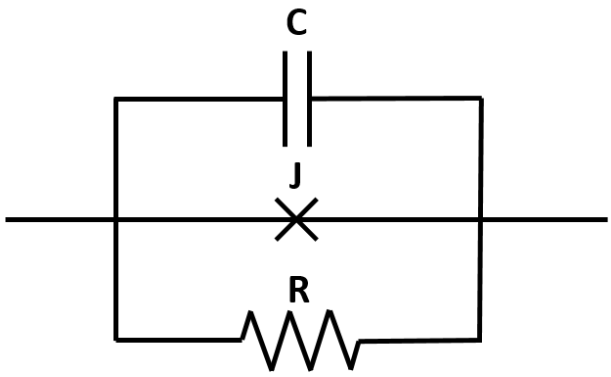

Figure 2.2: Model of JJ including the ideal JJ (J), capacitive coupling (C), and parasitic resistance (R).

Using the voltage relation of the JJ, the following equation is obtained:

$$C\phi_0^2\ddot{\phi} = -\frac{\delta U}{\delta \phi} - \frac{\phi_0^2}{R}\dot{\phi} \tag{2.12}$$

with a tilted washboard potential, $U(\phi) = -\phi_0 I_c \cos\phi - \Phi_0 I_B \gamma$ and reduced quantum flux Φ_0. With very large R, the problem is reduced back to the ideal JJ.

2.2 Superconducting Qubits

For experimentation, state preparation and control are two key considerations in choice of a quantum system. Reliable state preparation requires that at least two states must have dependable initialization sequences. Superconducting qubits make this easy if the thermal occupation is negligibly small, $k_B T \ll E_C, E_J$, which implies they need to be cooled down to low temperatures. With dilution refrigerators temperatures 10's mK are achievable, which is much less than the temperatures of 100's of mK enforced by the E_C and E_J. Qubit control is also straightforward as transition frequencies between energy levels are typically in the microwave regime. Microwave technology is well developed for other engineering fields and allows for the use of off-the-shelf equipment.

The transition frequencies of superconducting (SC) qubits can be designed such that they are of sufficiently different frequencies so that only one of these frequencies is within the envelope of frequencies produced by microwave equipment. Doing so allows for only one transition to be excited at a time, and more precise control to be managed.

The other consideration is the lifetime of the states. Dissipative loss and vacuum fluctuations can introduce undesired transitions between energy levels which limits the energy relaxation time, T_1. Limiting the interactions of the qubit with the environment maximizes the coherence time T_2.

$$T_1 = \frac{1}{\Gamma_1} \tag{2.13}$$

$$T_2^* = \frac{1}{\left(\frac{\Gamma_1}{2} + \Gamma_\phi\right)} \tag{2.14}$$

where Γ_1 is the relaxation rate, and Γ_ϕ is the pure dephasing rate.

2.2.1 The Cooper Pair Box

The Cooper pair box (CPB), or charge qubit, consists of a JJ connected to a voltage source through a gate capacitor, Figure 2.3. The JJ allows coherent tunneling from a superconducting island to the reservoir [10]. The states of the CPB are defined by the number of charges on the island. Again, using a canonical derivation the Hamiltonian can be found to be

$$H = \frac{1}{2}E_C(\hat{n} - n_g)^2 - E_J \cos\hat{\phi} \tag{2.15}$$

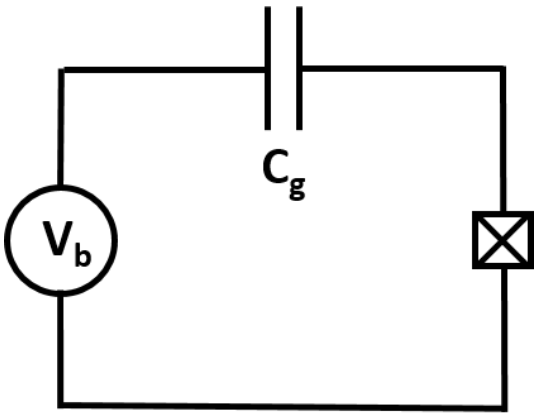

Figure 2.3: Schematic of the CPB superconducting qubit. The qubit is comprised of a JJ in series with a gate capacitor connected to a voltage source.

Using the quantum commutation relation $[\hat{n}, \hat{\phi}] = i$, the Hamiltonian can be rewritten in the charge basis [17][13].

$$\frac{1}{2}E_C(\hat{n} - n_g)^2 - \frac{E_J}{2}\sum_n (|n+1\rangle\langle n| + |n\rangle\langle n+1|) \tag{2.16}$$

where the charging energy is $E_C = {}^{(2e)^2}/_{C_s + C_g}$ and the Josephson energy is $E_J = \phi_0 I_C$. The charging energy is the energy required to add an electron to the island, and is determined by the total capacitance of the system. The gate charge $n_g = {}^{-C_g V_b}/_{2|e|}$ is the number of Cooper pairs on the gate island, while n is the number of Cooper pairs that have left the island.

In the charge regime, $E_C \gg E_J$ the first term of the Hamiltonian dominates and the energy levels are $E_n = {}^{E_C}/_2(\hat{n} - n_g)^2$. The energy levels would cross at half integer values of n_g. Here, the Josephson energy is important, creating avoided crossings, Figure 2.4.

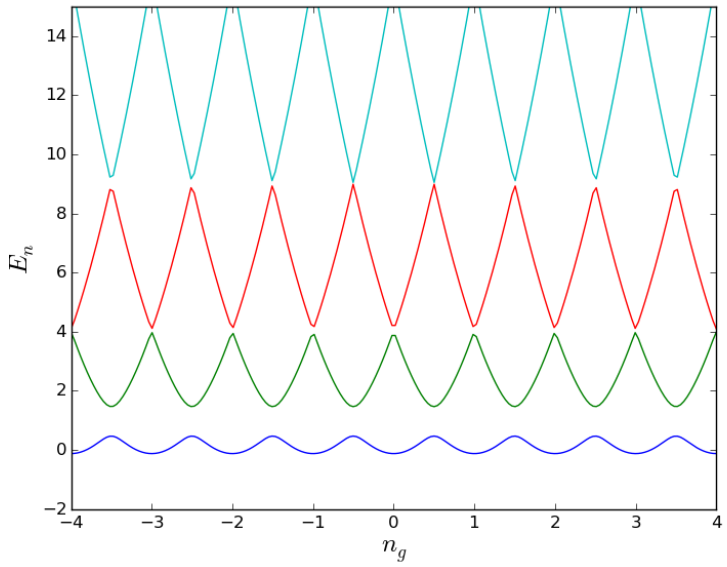

Figure 2.4: Energy spectrum (E_n) of the CPB as a function of charge on the island (n_g). The energy is dominated by the first term of Equation 2.16, but close to the degeneracy points the second term is important, causing the avoided level crossings.

To use the qubit, the coherence time needs to be as long as possible: T_1 and T_2 must be maximized. Both are dependent on the intensity of the dominant noise, the ${}^1/_f$ noise, Equations 2.17 and 2.18. From Figure 2.5, it is clear that the intensity of the ${}^1/_f$ at $\omega \sim 0$ is much larger than the intensity at the qubit frequency, $S_{n_g}(\omega \sim 0) \gg S_{n_g}(\omega_{qb})$.

$$\Gamma_1 = \frac{2\pi}{\hbar^2} E_Q^2 \sin^2\theta S_{n_g}(\omega_{qb}) \tag{2.17}$$

$$\Gamma_\phi = \frac{2\pi}{\hbar^2} E_g^2 \cos^2\theta S_{n_g}(0) \tag{2.18}$$

Referring to Equations 2.13 and 2.14, the coherence time depends more on the dephasing time than relaxation time since $\Gamma_\phi \gg \Gamma_1$. Therefore, the CPB is operated at $n_g = {}^n/_2$ where

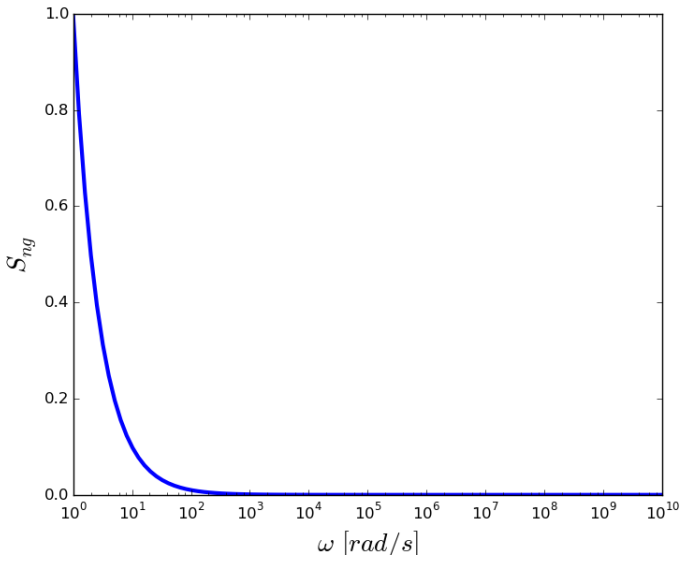

Figure 2.5: Intensity of the $1/f$ noise as a function of radial frequency ω. The intensity grows exponentially bigger as $\omega \to 0$, and tends to 0 at large frequencies.

the dephasing time is minimized and the relaxation time is maximized. This is often called the "sweet-spots" of operation.

This type of qubit was used in the first experiment where coherent oscillations were observed in a solid-state device in an experiment conducted by Nakamura et al. in 1999 [41].

2.2.2 The Transmon

The CPB is very sensitive to noise: $1/f$ noise comes from charge noise pushes it away from the "sweet spots" of operation [34]. Even a single quasiparticle event can completely dephase the qubit and excite other transitions [34]. This noise limits the coherence time of the qubit.

To extend the coherence time of the qubit, two factors must be balanced: anharmonicity and charge dispersion. Anharmonicity is how similar the energy spacing looks to that of a simple harmonic oscillator (simple harmonic oscillator (SHO)). The energy levels of a SHO are evenly spaced, meaning photons of the same energy can continue to push the state of the qubit into higher energy levels. The more anharmonic are the energy levels

of the qubit, the more control there is over the state of the qubit. A photon exciting the E_{01} transition will not excite the E_{12} transition, providing accurate state control. This is especially important for quick gate time. A short pulse will excite more frequencies and if the energy levels are close together, large amounts of filtering would be needed to ensure that only the desired transition is excited.

Charge dispersion relates to how flat the energy levels are as a function of gate charge. The lower the charge dispersion, the flatter the energy levels and therefore changes in the number of charges on the island do not effect the transition energies of the system as much and the system is immune to charge noise.

Overall, the anharmonicity should be maximized, while the charge dispersion needs to be minimized. This can be done through the E_J/E_C ratio. Increasing E_J/E_C decreases both anharmonicity and charge dispersion. As anharmonicity decreases with the root of E_J/E_C,

$$\alpha \propto \sqrt{8\frac{E_J}{E_C}} \tag{2.19}$$

while charge dispersion decreases exponentially

$$\epsilon_m \propto e^{-\sqrt{8\frac{E_J}{E_C}}} \tag{2.20}$$

the charge dispersion can be decreased effectively with little effect to the anharmonicity.

The Transmission Line Shunted Plasma Oscillation Qubit (transmon) was developed from this idea [34][52]. A shunt capacitor, C_S, was added in parallel with the JJ pair, as in Figure 2.6, decreasing E_C through the relation:

$$E_C = \frac{e^2}{2C_\Sigma} \tag{2.21}$$

where $C_\Sigma = C_J + C_S + C_g$.

The energy levels flatten out as E_J/E_C increases, Figure 2.7. Operating at high enough E_J/E_C, generally 40 to 100 provides a qubit that is almost immune to charge noise. C_S is chosen such that the charging energy is typically in the range 200MHz$\leq E_C/h \leq$ 500MHz. This change drastically increased the coherence times of the qubit, pushing them from μs [41] up to 100ms [48], but also increased the gate times of the qubit. Since their development, these qubits have been used in many SC qubit experiments.

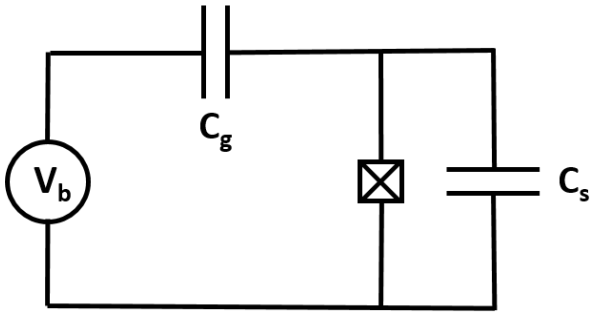

Figure 2.6: Schematic of the transmon. The transmon is a modified CPB with a shunt capacitor added in parallel to the JJ, to decrease the $E_C$of the system.

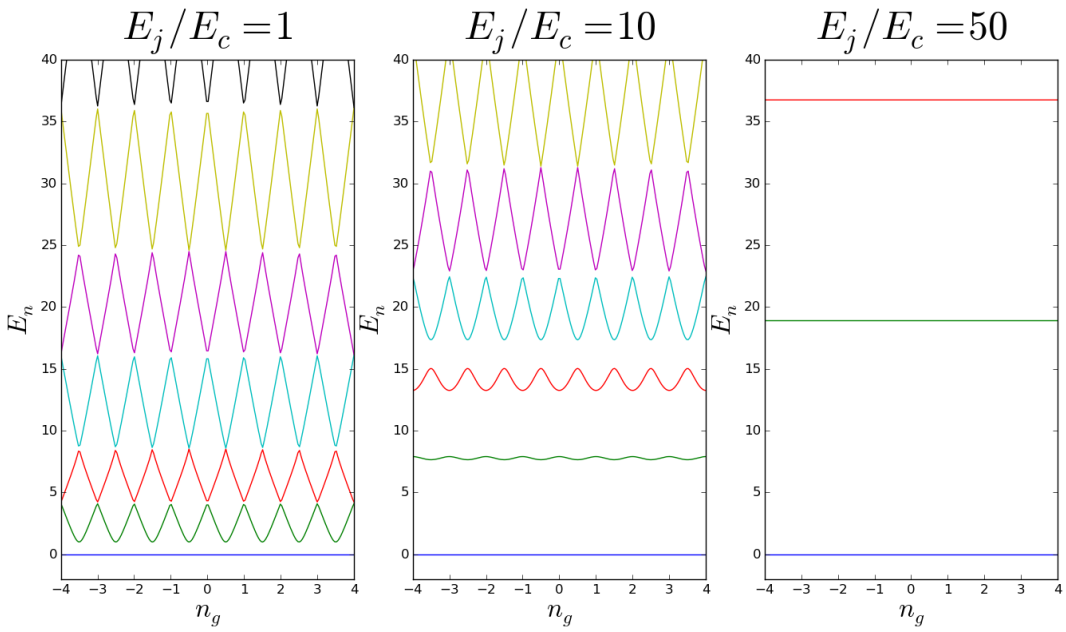

Figure 2.7: Energy levels of the CPB or transmon with increasing $^{E_J}/_{E_C}$. As $^{E_J}/_{E_C}$ increases the energy levels flatten out making the energy of the system more immune to changes in the number of charges on the island, n_g, flux noise.

2.3 The Bloch Sphere

The states of any two level system can conveniently be imagined as the surface of a unit-sphere, Figure 2.8, represented by Equation 2.22 [60]. Opposite sides of the sphere represent mutually exclusive, orthogonal states. Letting the negative z-axis represent the state $|0\rangle$ and the positive z-axis the state $|1\rangle$, moving along the surface of the sphere, the mixing of the two states is given.

$$|\psi\rangle = \cos\frac{\theta}{2}|0\rangle + e^{i\phi}\sin\frac{\theta}{2}|1\rangle \tag{2.22}$$

where $0 \leq \theta \leq \pi$ and $0 \leq \phi \leq 2\pi$.

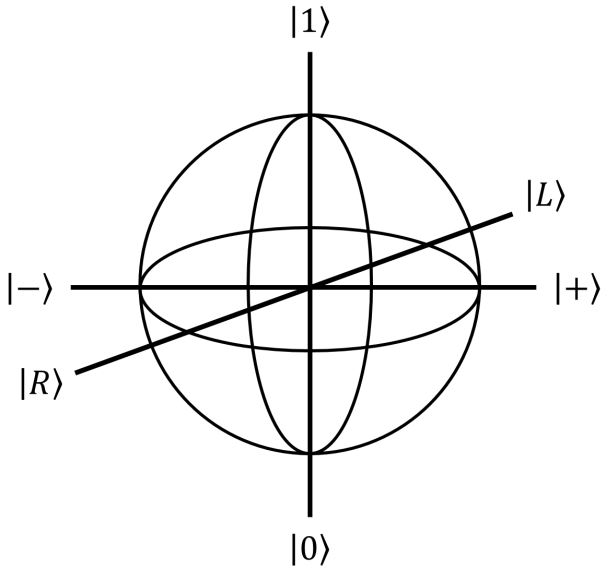

Figure 2.8: The Bloch sphere is a visual representation of the Hilbert space of a two level system. The mixing of the states $|0\rangle$ and $|1\rangle$ are given by the surface defined by Equation 2.22. Here, $|+/-\rangle = {}^{(|0\rangle \pm |1\rangle)}/\sqrt{2}$ and $|R/L\rangle = {}^{(|0\rangle \pm i\,|1\rangle)}/\sqrt{2}$.

2.4 Cavity QED

To attain longer coherence times, the qubit needs to be isolated from the environment. To accomplish this, the number of modes (frequencies) that the qubit can couple to are limited

by placing it in a cavity. The cavity acts as a SHO, with only certain EM frequencies able to resonate. These can be half or full wave, ddepending on whether the termination of the cavity is a short or open circuit. The reflection coefficient is

$$\mathbf{R} = \frac{Z_L - Z_S}{Z_L + Z_S} \tag{2.23}$$

where Z_L is the load (termination) impedance and Z_S is the impedance of the cavity [45]. If the cavity is terminated with a short circuit $Z_L = 0$ and $\mathbf{R} = 1$, then only frequencies that have wavelengths such that odd multiples of a quarter wave are the length of the resonator will resonate. All other frequencies will be suppressed. This is called a quarter-wave resonator. If the cavity is terminated with an open circuit, $Z_L = \infty$ and $\mathbf{R} = -1$, then the resonator is a half-wave resonator

Resonators are described by the quality factor, Q. This is a measurement of photon loss rate, defined as the ratio between energy stored in the electromagnetic (EM) field, U, to the energy loss, P_d, per period of oscillation, T, multiplied by 2π.

$$Q = \frac{2\pi}{T}\frac{U}{P_d} = \frac{\omega_{cav} U}{P_d} \tag{2.24}$$

where ω is the angular frequency of the oscillations.

The cavity transmission will take on a Lorentzian lineshape, centred around the resonant frequency, ω_{cav} as long as $Q \gg 1$, Figure 2.9. Then Q can be written as the ratio of ω_{cav} to the loss rate of the cavity, κ, Equation 2.25. κ can be experimentally measured as the bandwidth (BW), of the line shape, which is the difference of the frequencies at the full-width, half-max (FWHM) of the line shape. This gives an experimental technique to determine Q.

$$Q = \frac{\omega_{cav}}{\kappa} = \frac{\omega_{cav}}{BW} \tag{2.25}$$

The losses in the system come from both internal loss, such as surface losses, and external loss such as through coupling to the environment. The internal and external losses are related to the total Q of the system through

$$\frac{1}{Q} = \frac{1}{Q_{int}} + \frac{1}{Q_{ext}} \tag{2.26}$$

The reciprocal nature of the relation is due to the Qs being reciprocal to loss and the losses summing in a system. The total Q, including the losses through the coupling to the output lines, is called the loaded quality factor.

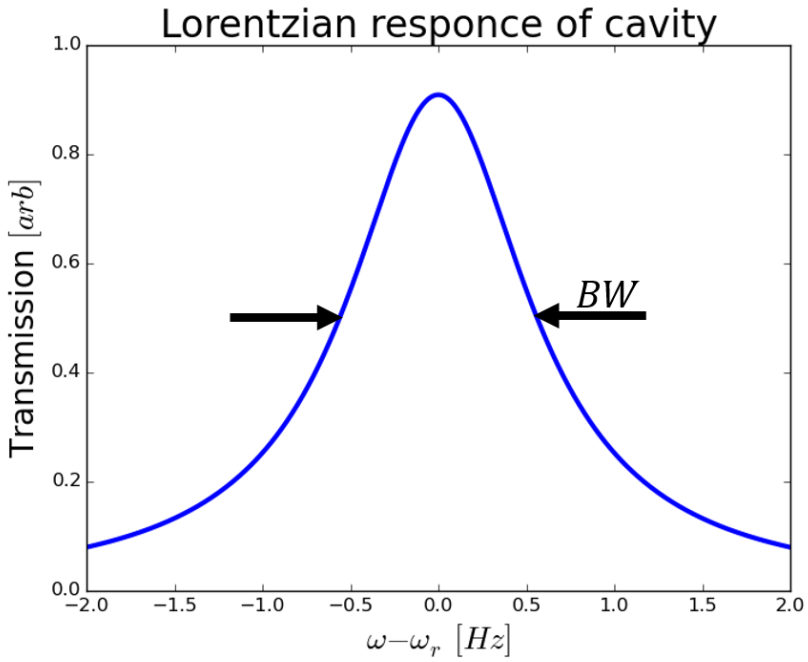

Figure 2.9: Transmission line shape of a resonator. The bandwidth of the Lorenzian line shape is determined by the loss rate of the cavity.

SC resonators are either planar, Figure 2.10, or 3D, Figure 2.11. The planar resonators are usually made from a section of co-planar waveguide capacitively coupled to transmission lines. A 3D resonator is cavity enclosed by metal, usually aluminum. The dimensions of the cavity determine the resonance frequencies. 3D cavities minimize photon losses due to two-level systems at the surface of the material and therefore are able to reach higher quality factors and thus longer coherence times.

2.4.1 Quantization of the Cavity

Using a rectangular SC cavity made of aluminum, the EM fields are defined by the boundary conditions. For experiments, the qubit must be at a node of the EM field, therefore the lowest modes that are relevant are the transverse electric. This implies the electric field is

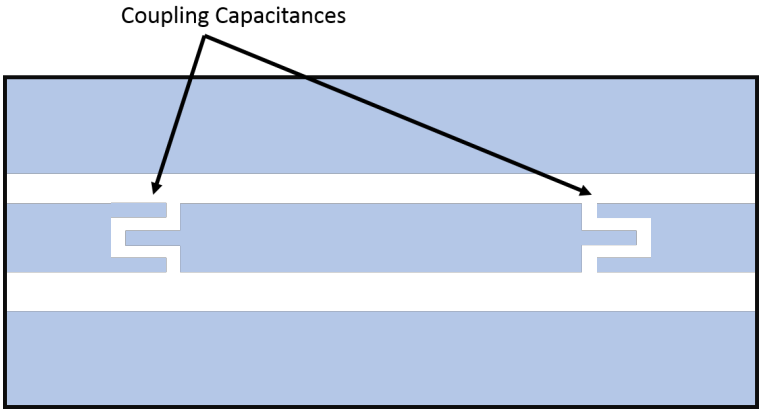

Figure 2.10: Planar resonator. The resonator is comprised of a co-planar waveguide which is capacitively coupled to a transmission line for experimentation.

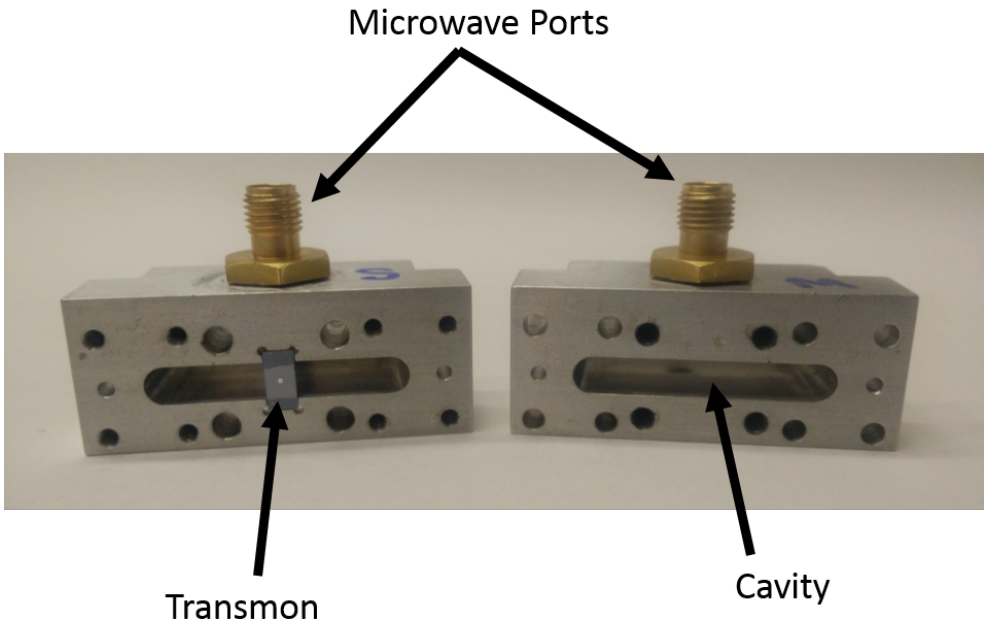

Figure 2.11: 3D cavity resonator made of aluminum. The hollowed cavity in the middle of the block of aluminum determines the resonance frequencies and the coupling of the cavity to the transmission line is determined by the depth that a pin is inserted into the cavity. This 3D cavity and transmon was used in experimentation. The cavity is $2.7cm \times 3.15cm \times 4.2mm$.

perpendicular to the direction of propagation. If the field is propagating in the z-direction, the field can be defined as $\hat{E} = E_z \hat{e_z}$ where E_z is the magnitude and $\hat{e_y}$ is the unit direction vector [45]. Therefore, the modes TE_{10n} is defined by

$$E_z = E_0 \sin \frac{\pi x}{a} \sin \frac{n\pi z}{b} \tag{2.27}$$

where a is the x dimension of the cavity, b is the y dimension and n defines the mode. Increasing n increases the number of nodes and defines a frequency that can resonate. As there are three dimensions in the cavity, there are resonant frequencies for each of the three dimensions with the lowest corresponding to the smallest dimension. The coupling of these frequencies also relates to the direction that the EM field is injected into the cavity. The strongest coupling will happen with the dimensions that correspond to the direction of propagation of the field. The superfluous modes that are not desired for the experiment should be designed to be higher than the desired mode, such that higher harmonics do not couple as extra decay channels.

The field within the resonator can be quantized as a SHO [51]. Each frequency defined by Equation 2.27 can be imagined to correspond to a rung on a ladder, the quantized states. Each rung is then separated by an energy $\hbar\omega_{cav}$ where ω_{cav} is the smallest resonant frequency of the resonator. Letting $\hat{a}$ be the operator that drops from one rung to the rung below (annihilation operator) and $\hat{a}^\dagger$ takes the state up one rung of the ladder, the Hamiltonian for the resonator is obtained.

$$H_{cav} = \hbar\omega_{cav}\hat{a}^\dagger\hat{a} \tag{2.28}$$

2.4.2 Qubit in a Cavity

Placing a transmon in a cavity, the Hamiltonian can be modelled as the sum of: the Hamiltonians of the cavity, the transmon, and an interaction term.

$$H = H_{cav} + H_{qb} + H_{int} \tag{2.29}$$

From 2.4 and Equation 2.28, it is known that the cavity term is Equation2.28. Restricting the qubit to the ground and first excited state, Hamiltonian can be modeled as $H_{qb} = (\hbar\omega_{qb}/2)\left(|e\rangle\langle e| - |g\rangle\langle g|\right) = (\hbar\omega_{qb}/2)\,\sigma_z$ where $|g\rangle$ and $|e\rangle$ are the ground and excited states of the qubit.

Using the bosonic quantization of an EM field from Section 2.4.1, $\hat{E} = \hat{a}^\dagger + \hat{a}$, and the coupling of the qubit to the field $\hat{S} = |e\rangle\langle g| + |g\rangle\langle e| = \sigma_+ + \sigma_-$ the interaction term is defined as

$$H_{int} = \frac{\hbar\Omega}{2}\hat{E}\hat{S} = \frac{\hbar\Omega}{2}(\hat{a}^\dagger + \hat{a})(\sigma_+ + \sigma_-) \tag{2.30}$$

Defining $\frac{\hbar\Omega}{2}$ as g, the coupling strength, the final form of the full Hamiltonian becomes [34]

$$H = \hbar\omega_{cav}\hat{a}^\dagger\hat{a} + \frac{\hbar\omega_{qb}}{2}\sigma_z + g(\hat{a}^\dagger + \hat{a})(\sigma_+ + \sigma_-) \tag{2.31}$$

This equation describes how energy: taken from the qubit creates a photon in the cavity through the energy conservation terms $\sigma_-\hat{a}^\dagger$ or an excitation of the qubit is created through the absorption of photon, $\sigma_+\hat{a}$. The two terms that do not conserve excitation number, $\sigma_-\hat{a}$ and $\sigma_+\hat{a}^\dagger$ describe a simultaneous excitation (or relaxation).

2.4.3 The Rotating Wave Approximation

When the coupling strength $g \ll \omega_{qb}, \omega_{cav}$, the Hamiltonian can be simplified so that it becomes analytically solvable [61]. To simplify the interaction part of the Hamiltonian, the reference frame is switched to a frame rotating with the qubit and cavity, $H_0 = H_{cav} + H_{qb}$. This approximation is called the Rotating Wave Approximation (RWA).

The Hamiltonian then becomes

$$H_{int} = \frac{\hbar\Omega}{2}(\hat{a}\sigma_- e^{-i(\omega_{cav}+\omega_{qb})t} + \hat{a}^\dagger\sigma_+ e^{i(\omega_{cav}+\omega_{qb})t} + \hat{a}\sigma_+ e^{i(-\omega_{cav}+\omega_{qb})t} + \hat{a}^\dagger\sigma_- e^{-i(-\omega_{cav}+\omega_{qb})t}) \tag{2.32}$$

In this frame, and near resonance, the terms $\omega_{cav} + \omega_{qb}$ rotate quickly compared to the $-\omega_{cav} + \omega_{qb}$ terms, and they can be discarded. After discarding the fast oscillating terms, and transferring back to Shrodinger picture, Jaynes-Cummings Hamiltonian is obtained:

$$H = \hbar\omega_{cav}\hat{a}^\dagger\hat{a} + \frac{\hbar\omega_{qb}}{2}\sigma_z + g(\hat{a}^\dagger\sigma_- + \hat{a}\sigma_+) \tag{2.33}$$

Far from degeneracy, the levels of the systems, qubit and cavity remain uncoupled. The energy levels of this system are shown in blue in Figure 2.12. Close to degeneracy of

the qubit and cavity, $\omega_{qb} \sim \omega_{cav}$, the energy levels of the system couple and the combined energy states are shown in orange in Figure 2.12.

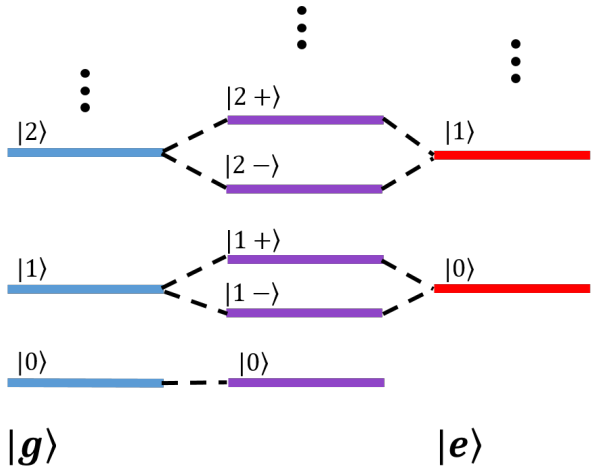

Figure 2.12: Energy levels of the cavity when the qubit is in the ground state, $|g\rangle$, (blue) and excited state, $|e\rangle$ (red). The number states indicate the state of the cavity. When the qubit and cavity are degenerate ($\omega_{qb} \sim \omega_{cav}$) the energy levels combine and they form the purple states.

2.4.4 The Dispersive Regime

The dispersive regime occurs when $\Delta =\mid \omega_{qb} - \omega_{cav} \mid \gg g$. This regime allows for optimal control of the system and is used often for QI experiments. In this regime, the cavity-qubit interaction can be limited to the lowest order through canonical transformation. It is in this regime where restricting the qubit to the ground and first excited states, the following effective Hamiltonian can be used [21]:

$$H = \frac{\hbar\omega'_{01}}{2}\sigma_z + (\hbar{\omega_{cav}}' + \hbar\chi\sigma_z)\hat{a}^\dagger\hat{a} \tag{2.34}$$

The qubit and cavity frequencies shift due to the presence of the other in the system [34]. The shift in the qubit frequency is due to the coupling between the transition between the ground and first excited state of the qubit to the cavity $\omega'_{01} = \omega_{01} + \chi_{01}$ while the shift in the cavity frequency is due to the coupling to the transition between the first and second

excited states of the cavity, ${\omega_{cav}}' = \omega_{cav} - \chi_{12}/2$. The shifts are defined as

$$\chi_{ij} = \frac{g_{ij}^2}{\omega_{ij} - \omega_{cav}} \tag{2.35}$$

where $\omega_{ij} = \omega_j - \omega_i$ and g_{ij} is the coupling between ω_{ij} and the cavity. The dispersive shift is given by

$$\chi = \chi_{01} - \frac{\chi_{12}}{2} \tag{2.36}$$

When then qubit is in the ground state, the cavity is excited at a frequency of $\langle 1, g| H |1, g\rangle - \langle 0, g| H |0, g\rangle = -\hbar(\chi_{01} - \chi_{12})/2$. When the qubit is in the excited state the cavity is excited at a frequency of $\langle 1, e| H |1, e\rangle - \langle 0, e| H |0, e\rangle = \hbar(\chi_{01} - \chi_{12})/2$. The difference between these two frequencies is then $2\hbar(\chi_{01} - \chi_{12})/2 = 2\hbar\chi$

χ can also be written in terms of g_{01} through

$$\hbar\chi \simeq \frac{(\hbar g_{01})^2 \alpha}{\hbar^2 \delta_0 \delta_1} \tag{2.37}$$

where $\delta_i = \omega_{i,i+1} - \omega_{cav}$, giving us a second way to experimentally measure g_{01}.

2.5 Lambda Systems

Lambda systems take their name from the configuration of energy levels in them. They are characterized by a metastable state ($|e\rangle$): one that has a relatively long lifetime compared to the other energy levels of the system. The organization of these states are shown in Figure 2.13. An excited state, $|f\rangle$ quickly decays into the metastable state, $|e\rangle$, which then slowly decays into the ground state, $|g\rangle$.

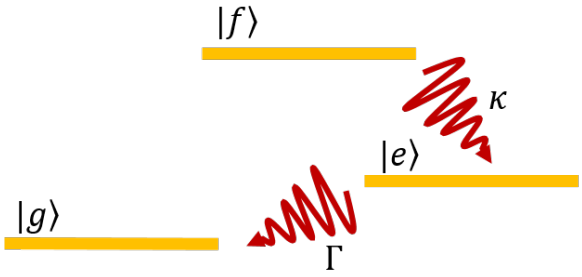

Figure 2.13: The arrangement of energy levels in a lambda system. The decay rate Γ must be much smaller than the decay rate κ so that $|e\rangle$ becomes a metastable state.

These systems are common in atomic physics, due to the complex interactions of particles in atoms. They have been used to demonstrate many interesting physics' phenomena including fast or slow light. Three of these phenomena, coherent population trapping (CPT), EIT and DIT form through similar processes, but occur under different experimental parameters. A fourth phenomenon, Aulters-Townes splitting (ATS), is discussed here, as it can look similar to CPT, DIT and DIT, but it occurs though very different processes. All three phenomena have interesting applications that could be used in quantum information processing. The main application being the control of EM signals using much weaker signals, similar to transistors. These configurations have been used in single photon transistors, and single photon detectors.

2.5.1 Aulter-Townes Splitting

Strongly driving a two-level quantum system (TLS) resonantly produces a dressed field, the purple energy levels of Figure 2.12. The splitting between these is determined by the Rabi frequency of the drive field. If probing a second transition of the system, the splitting is apparent, ATS [49].

To explore ATS, two drives are used. The first, the probe, ω_c, drives the transition between $|g\rangle \leftrightarrow |e\rangle$ of the qubit, in Figure 2.12. A probe probe, ω_p is used to drive the cavity between the ground and first excited states ($|0\rangle \leftrightarrow |1\rangle$, Figure 2.14).

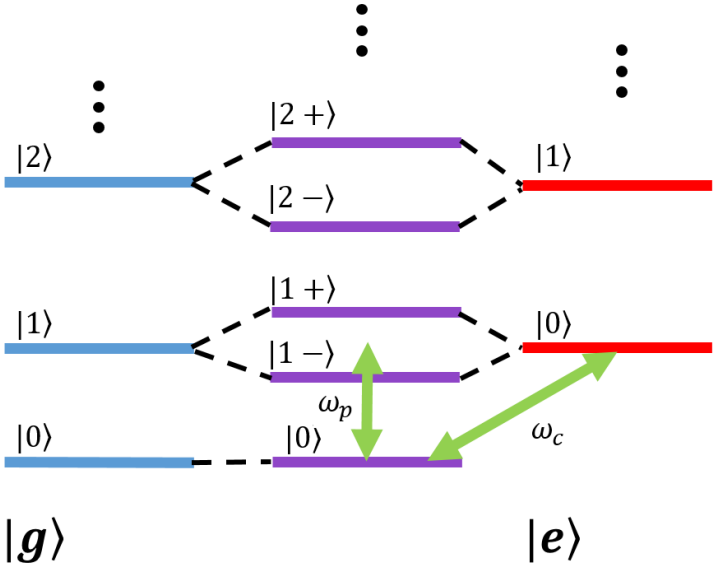

Figure 2.14: Microwave drives for ATS experiment. ω_c probes the $|g\rangle \leftrightarrow |e\rangle$ transition, causing $|1\rangle$ to split into $|1\pm\rangle$. Sweeping ω_c near the $|0\rangle \leftrightarrow |1\rangle$ shows a splitting in the transmission line.

Absorption of the couplerfrequency, $^{\omega_c}/_{2\pi}$, is seen due to the doublet produced by the drive strength, Ω_p, of ω_p. As Ω_p increases, $|1\rangle$ splits into a doublet ($|1-\rangle$, $|1+\rangle$). This produces a splitting in the transmission line of ω_c at ω_{cav} The two peaks in transmission form at $\delta = \pm^{\Omega_p}/_2$. As Ω_p continues to increase, the two peaks continue to separate and the dip grows stronger, Figure 2.15.

This phenomenon has been widely studied in atomic, molecular and superconducting qubit systems.

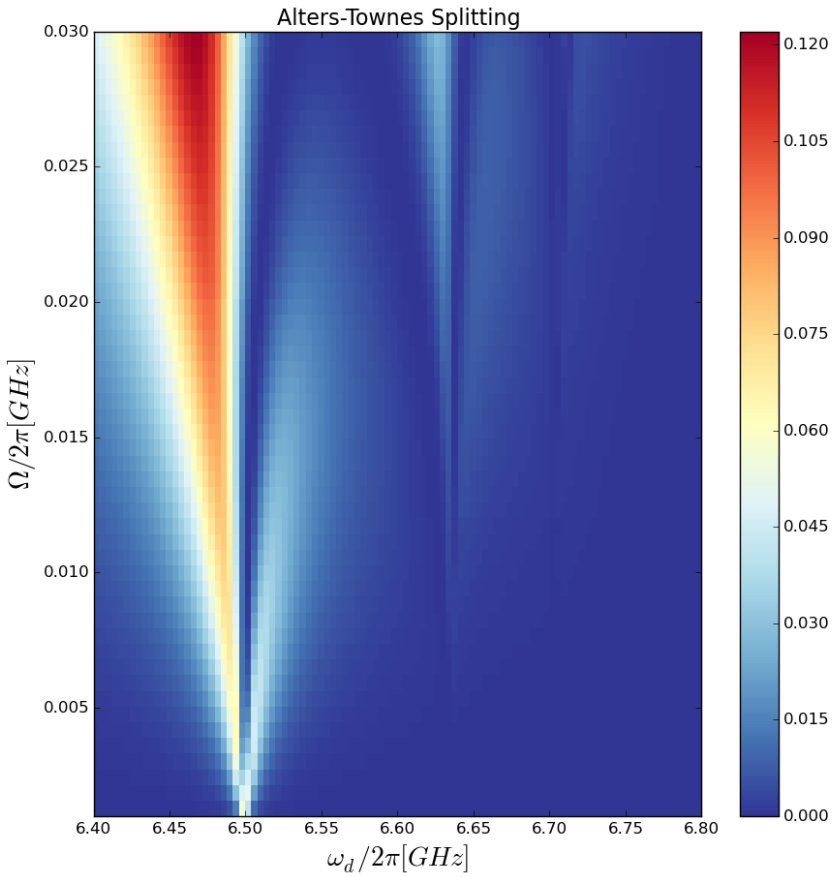

Figure 2.15: Simulation following [8] of the transmission of a cavity demonstrating ATS. The qubit and cavity are in resonance ($\omega_{cav} = \omega_{qb}$). As the drive strength, Ω, increases, the transmission of the qubit frequency is suppressed and the splitting between transmission peaks separates further. The same phenomenon occurring with higher order qubit transitions are seen at ~ 6.68GHz and ~ 6.73GHz

2.5.2 Coherent Population Trapping and Induced Transparency

CPT, EIT and DIT are closely related phenomena, stemming from the destructive quantum interference of the transition amplitudes of three-level systems. Trapping the quantum system in a dark state through the use of two coherent drives, is referred to as CPT. Once CPT is established, the system becomes transparent to light, EIT or DIT [36]. Both CPT and induced transparency can be demonstrated in lambda systems. Two drives are used in each experiment. The probe, ω_p diving the $|g\rangle \leftrightarrow |f\rangle$ transition and the coupler, ω_c, driving the $|e\rangle \leftrightarrow |f\rangle$ transition (Figure 2.16).

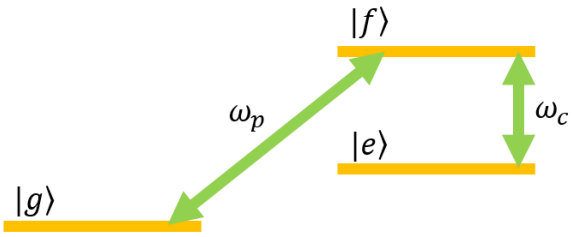

Figure 2.16: A lambda arrangement of energy levels can be used for CPT and EIT experiments. In both experiments, two coherent drives are used: ω_p to drive the $|g\rangle \leftrightarrow |f\rangle$ transition and ω_c to drive the $|e\rangle \leftrightarrow |f\rangle$ transition. Although contrary to most literature, this naming convention is used to remain consistent with [42]

Electromagnetically Induced Transparency

When ω_c is driven strongly, a transmission window appears in the absorbance line of ω_p, or EIT [35] [9]. This phenomenon is seen in atomic vapours containing atoms with three-level systems (vee, ladder and lambda, Figure 2.17). For EIT to occur two of the transitions in the system must be dipole allowed ($|g\rangle \leftrightarrow |f\rangle$ and $|e\rangle \leftrightarrow |f\rangle$), the transition can be induced by an oscillating electric field, driven by ω_c and ω_p. ω_p couples $|g\rangle \leftrightarrow |e\rangle$, while ω_c couples $|e\rangle \leftrightarrow |f\rangle$ (Figure 2.16). It is also required that one of the energy levels, $|e\rangle$, be metastable. When all of the conditions are met, the transparency window in the absorbance line of ω_p is caused by the destructive interference of quantum transition probability amplitudes of $|g\rangle \leftrightarrow |f\rangle$ and $|e\rangle \leftrightarrow |f\rangle$.

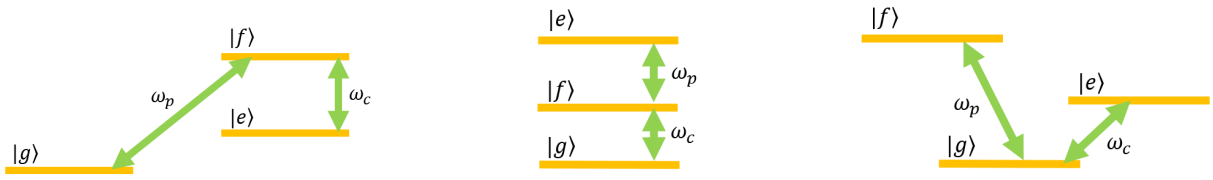

(a) (b) (c)

Figure 2.17: Three-level systems that exhibit EIT include **(a)** lambda, **(b)** ladder, and **(c)** vee energy level configurations. For EIT to occur, $|e\rangle$ must be metastable.

This transparency can also be seen in the spectrum of ω_c. When the probability amplitudes interfere, ω_c is absorbed and a absorbance line in seen in the transmission of ω_c.

EIT can be observed by sweeping the frequency of both ω_p and ω_c. For constant Ω_c and Ω_p, the transmission of ω_c is monitored. At zero detuning of the drives, Δ_c=Δ_p= 0, EIT occurs and the absorbance line is seen. Detuning ω_p, causes the absorbance line to shift by Δ_p, and the absorbance line is seen at $\Delta_c = \Delta_p$.

Dipole Induced Transparency

Named for its similarities to EIT, DIT is a result of destructive interference between two quantum states of a single dipole emitter and cavity system [58]. Here, losses due to cavity leakage and dipole absoption cancel for large values of the Purcell factor inhibiting light from entering the cavity, through quantum interference, producing the signature absorption window [59]. DIT has been demonstrated in drop-filter cavity-waveguide systems [] using a quantum dot, but other quantum systems, including SC qubits.

Most EIT and DIT experiments are conducted in reflection. The experiments conducted for this thesis were conducted using transmission through the cavity. If the resonant cavity frequency of the cavity, with the qubit in the excited state ($\omega_{cav} + \chi$) the transmission would expected to be $T_{-\chi} = 1 - A$, as seen in Figure 2.19. Instead, the experiments conducted for this thesis used the transmission of $\omega_{cav} - \chi$, the resonant frequency of the cavity with the qubit in the excited state. Since $\omega_{cav} + \chi$ is transmitted when the qubit is in the ground state, it is suppressed when the qubit is excited. Therefore, when the transmission coefficient of it is low, the qubit is in the excited state and $\omega_{cav} - \chi$ is

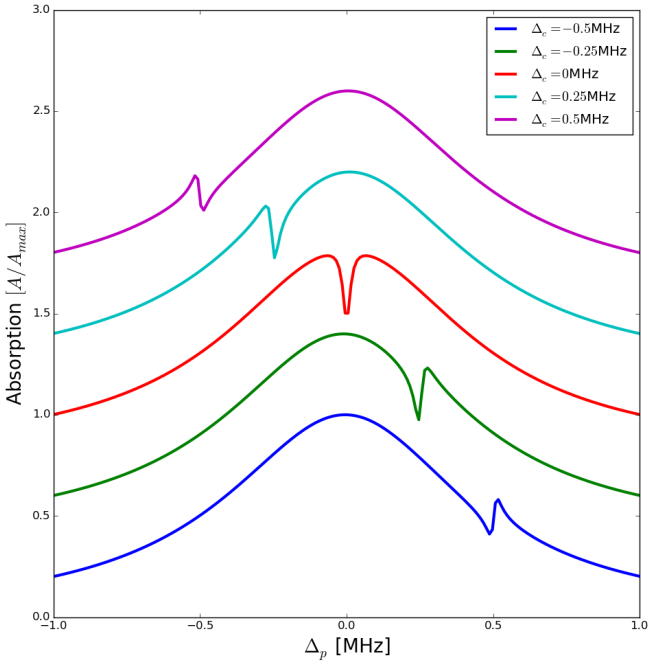

Figure 2.18: The absorption spectrum of a system demonstrating EIT. A narrow transmission window is seen in the absorption of the ω_c. This transmission window moves with the detuning of ω_p.

transmitted; it is excepted that the transmission of $\omega_{cav} - \chi$ frequency would be $T_{+\chi} = 1 - T_{-\chi} = 1 - (1 - A) = A$. . Therefore, we expect a similar line shape to Figure 2.18 for the transmission of $\omega_{cav} - \chi$.

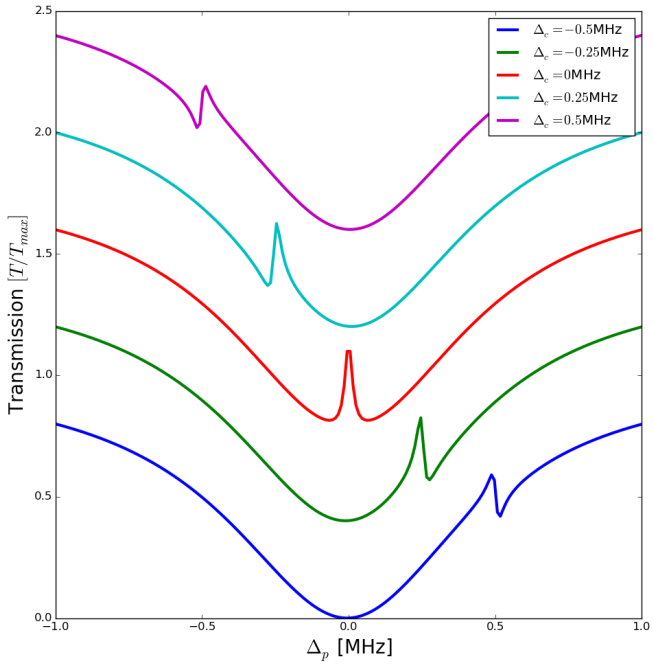

Figure 2.19: When conducting experiments using the transmission of ω_c instead of the absorption, the narrow transmission window appears as a peak in the supression of the transmission of ω_c.

Coherent Population Trapping

CPT occurs when a non-absorbing state, or dark state is formed from the lambda system due to coherent driving of the transitions of the lambda system. Through the use of two coherent drives the population is trapped in the dark state. This was first observed in a Na vapour cell as a decrease in the flourescense emission [1]. For CPT to be observed, the drives must be phase coherent.

When $|g\rangle \leftrightarrow |f\rangle$ and $|e\rangle \leftrightarrow |f\rangle$ are driven coherently, $|g\rangle$ and $|e\rangle$ form a dressed state

(purple energy levels of Figure 2.20). This state is a superposition of $|g\rangle$ and $|e\rangle$ which is dependent on Ω_c and Ω_p through the mixing angle $\Theta = \tan^{-1} \Omega_p/\Omega_c$ [42]. Without decoherence, the superposition states are then

$$|B/D\rangle = \cos\Theta\,|g\rangle \pm \sin\Theta\,|e\rangle \tag{2.38}$$

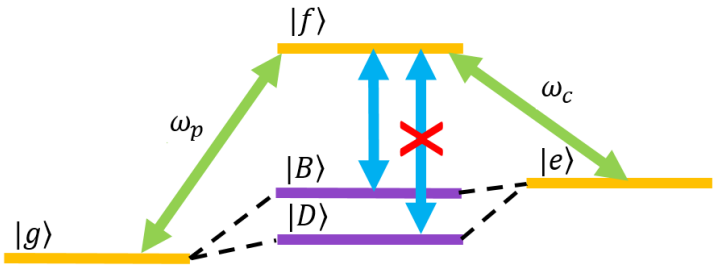

Figure 2.20: The ratio Ω_p/Ω_c determines the mixing angle Θ, which defines the hybridization of $|g\rangle$ and $|e\rangle$ into $|B\rangle$ and $|D\rangle$. Only the state $|B\rangle = \cos\Theta\,|g\rangle + \sin\Theta\,|e\rangle$ couples to $|f\rangle$, leaving $|D\rangle$ as the dark state.

Only one of these two states,the bright state $|B\rangle$, couples to $|f\rangle$. The other state, $|D\rangle$, does not couple to $|f\rangle$ and, thus, forms the dark state.

One demonstration of CPT can be done by sweeping the detuning of ω_p, Δ_p, for increasing Ω_c. With no ω_c, a population in $|e\rangle$ can be seen at Δ_p= 0. When ω_c is added with zero detuning (Δ_c= 0), the population splits. From Equation 2.38, it can be seen that as long as $\Omega_c \gg \Omega_p$, the dark state is $|g\rangle$, and the splitting indicates the presence of the dark state.

2.6 Creating an Effective Lambda System

In the dispersive regime, the energy levels of the cavity-qubit system form a double ladder arrangement (Figure 2.21), as described by the Jaynes-Cummings Hamiltonian (Equation 2.34). The rungs of each ladder are the energy levels of the cavity, while each ladder corresponds to the qubit in the ground (blue) and excited (yellow) state. Decay between

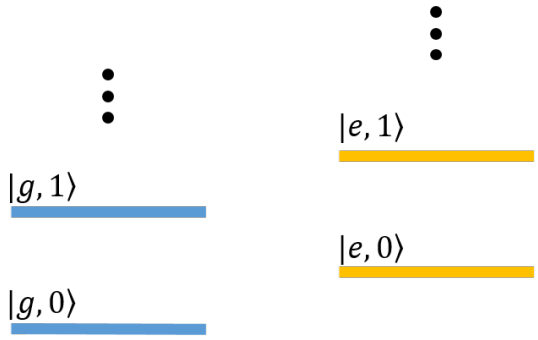

Figure 2.21: The double ladder formation of energy levels in the cavity-qubit system. With $\kappa \gg \Gamma$ the states $|g,0\rangle$, $|e,0\rangle$ and $|e,1\rangle$ can be used as the lambda system.

rungs on the ladder is determined by the decay rate of the cavity (κ), while the decay rate from the excited qubit ladder to the qubit ground state ladder is the decay rate of the qubit (Γ).

As long as the $\kappa > \Gamma$, if the system is driven to $|e,1\rangle$ it will quickly decay to $|e,0\rangle$. The only channel of decay is then from $|e,0\rangle$ to $|g,0\rangle$. Since this decay rate is Γ, the system will remain in $|e,0\rangle$ much longer than it was in $|e,1\rangle$, forming the metastable state. Therefore the energy levels $|g,0\rangle$, $|e,0\rangle$ and $|e,1\rangle$ can be used as the levels $|g\rangle$, $|e\rangle$ and $|f\rangle$ of the lambda system.

Using a transmon as the qubit in this experiment requires that $|g\rangle \leftrightarrow |f\rangle$ be a two-photon transition. If the two photon transistion is detuned, such that photons of two different frequencies (ω_{p_1} and ω_{p_2}) are used to excite the $|g\rangle \leftrightarrow |f\rangle$, two different microwave sources be used to drive each frequency (Figure 2.22). This allows for each frequency to be driven at a different Rabi drive frequency (Ω_{p_1} and Ω_{p_2}).

With sufficient detuning and using ω_{p_1} as a continuous wave drive, ω_{p_2} can be pulsed to turn on and off the ω_p. This experiment explores if Ω_{p_1} is strong enough, that Ω_{p_2} and the pulse length of ω_{p_2} can be reduced to a single photon and still invoke the transition.

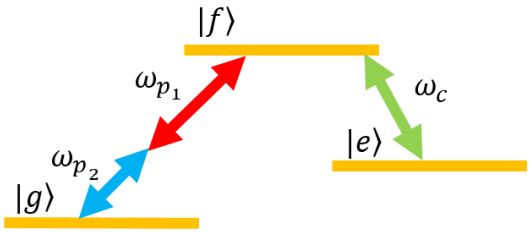

Figure 2.22: Using a transmon requires that $|g\rangle \leftrightarrow |f\rangle$ be a two-photon transistion. If the photons are detuned such that instead of two photons of the same frequency, two photons of different frequencies (ω_{p_1} and ω_{p_2}) are used, the drive strength (Ω_{p_1} and Ω_{p_2}) of each frequency can be controlled through different microwave sources.

2.7 Using the Lambda System as a Transistor

A transistor is a three terminal semi-conductor device. Two main configurations of the semiconductor materials are used: the field effect transistor (FET) and bipolar junction transistor (BJT) [54]. Applying a voltage or current to one of the terminals (called the base in a BJT) controls the current through the other two terminals (the collector and emitter) [54]. Since the current applied to the base can be much smaller than the current through the collector and emitter, the transistor can amplify the signal.

The lambda system can be used as a transistor for microwave signals. ω_c is used as the base signal, but there are two possible signals that can be used as the collector-emitter signal ($\omega_{control}$), as shown in Figure 2.24. The first of these is $\omega_{control} = \omega_{cav} - \chi$, the transition frequency of $|e,0\rangle \leftrightarrow |e,1\rangle$ in Figure 4.22. It can only resonate in the cavity when ω_p is turned on and the system is brought into the state $|e\rangle$ and so an increase in the transmission of $\omega_{control} = \omega_{cav} - \chi$ will be seen when ω_p is turned on.

The second signal is the $|g,0\rangle \leftrightarrow |g,1\rangle$ transition frequency, $\omega_{control} = \omega_{cav} + \chi$. This signal will resonate in the cavity until the system is brought to the state $|e\rangle$ by turning on ω_p, at which point there will be a suppression of the transmission of the signal.

This allows a gain to be defined in a similar manner to the gain of a transistor. In a BJT, this is the ratio of the collector-emitter current to the base-emitter current (I_{ce}/I_{be}). Here, gain is defined at the change in the number of photons in the controlled signal ($\omega_{control}$),

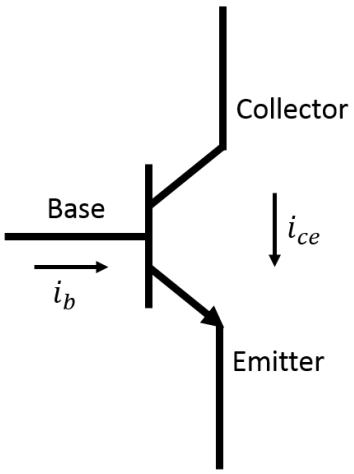

Figure 2.23: The schematic of a BJT. The current i_b control the flow of current from the collector to the emitter, i_{ce}. As i_{ce} can be greater than i_b, there is a gain of the transistor i_b/i_{ce}.

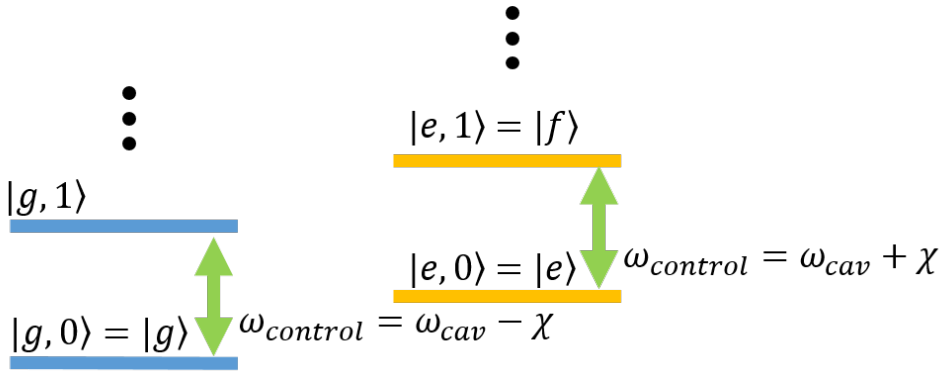

Figure 2.24: Two signals can be used as the collector-emitter signal of the microwave transistor. The two frequencies correspond to the resonant frequency of the cavity, with the qubit in the ground or excited state ($\omega_{control} = \omega_{cav} \pm \chi$).

to the number of photons in the pulsed probe drive, ω_{p_2}, as seen in Equation 2.39

$$G = \frac{\text{\# photons gained/lost from } \omega_{control}}{\text{\# photons in } \omega_{p_2}} \tag{2.39}$$

Chapter 3

Theoretical Modelling

The lambda system consists of three energy levels of the cavity-qubit system: $|g,0\rangle = |g\rangle$, $|e,0\rangle = |e\rangle$, and $|e,1\rangle = |f\rangle$ (Figure 3.1). A probe drive, ω_p with drive strength Ω_p, is used to drive the $|g\rangle \leftrightarrow |f\rangle$ transition. Due to the restrictions of the transmon, this must be a two photon transition. For DIT-like experiments another microwave drive, ω_c is used to drive the $|e\rangle \leftrightarrow |f\rangle$ transition.

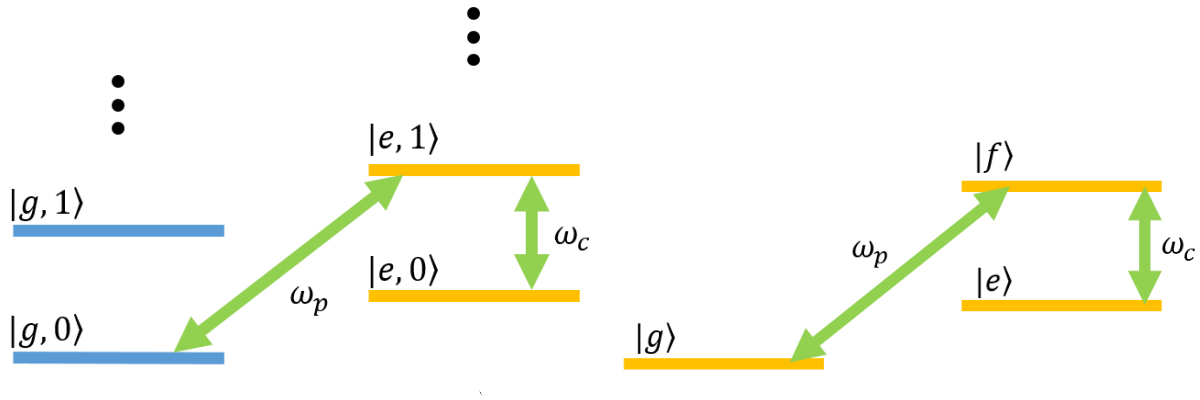

(a) (b)

Figure 3.1: The energy levels of the lambda system. **(a)**The lower energy levels from the cavity-qubit system are used to form **(b)** the lambda system. $|g,0\rangle = |g\rangle$, $|e,0\rangle = |e\rangle$, and $|e,1\rangle = |f\rangle$. The decay rate $|f\rangle \rightarrow |e\rangle$ is κ while $|e\rangle \rightarrow |g\rangle$ is Γ

Since the advantage of two probe drives is that they can be detuned away from the

two-photon transition frequency of $\omega_{gf}/2$: driven by ω_{p_1} and ω_{p_2} with Rabi drive frequencies Ω_{p_1} and Ω_{p_2}. This allows for one of the two drives to be continuous and only induce the transition when the second couper drive is pulsed on. It is expected that as long as the continuous drive is driven sufficiently strong, the pulsed drive could be turned down to a single photon.

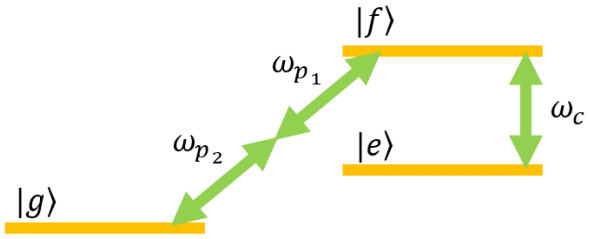

Figure 3.2: The two photon transition of $|g\rangle \leftrightarrow |f\rangle$ can be driven by two separate microwave drives, at different frequencies. This is expected to allow for control of the system with a single photon.

Theoretical modelling was conducted to investigate the effects of two probe drives on the lambda system. First, using the model developed by Nokikov et al. for [42] for a single ω_p, the predictions are reproduced to check the validity of the implementation. This model uses both a rotating frame approximation and a RWA to remove any time dependence.

Unfortunately, the model does not include the time dependence interference of two detuned probe drives. A model was developed to incorporate the second probe drive. This new model keeps the time dependence, but restricts the Hilbert space to only the energy levels of interest.

The new model is first used to reproduce the results from [42] by keeping $\omega_{p_1} = \omega_{p_2}$ and $\Omega_{p_1} = \Omega_{p_2}$. Then ω_{p_1} and ω_{p_2} are detuned to see if the sum of the drive frequencies changes with detuning. Lastly, the time dependence is investigated to see if a single photon can induce the $|g\rangle \leftrightarrow |e\rangle$ transition.

In both models, the excited state population of the qubit is plotted to represent the population of $|e\rangle$. Since both $|e\rangle$ and $|f\rangle$ require the qubit to be in the excited state, the excited state population of the qubit is the sum of the populations of $|e\rangle$ and $|f\rangle$. As

$\kappa \gg \Gamma$, there should be very little population in $|f\rangle$ and the excited state population of the qubit is an accurate measurement of the population of $|e\rangle$.

Example code for the simulations for this chapter can be found in Appendix A.

3.1 Single Probe Drive

Using the model developed by Novikov et al. in [42] for a single probe drive, the lambda system is driven by two drives. The first, ω_p, drives the $|g,n\rangle \leftrightarrow |e,n+1\rangle$ transition via a two photon transition. For DIT-like experiments ω_c drives the $|e,n\rangle \leftrightarrow |e,n+1\rangle$ transition. Using the dispersive JC Hamiltonian (Equation 2.34), the detunings can be defined as $\Delta_p = 2\omega_p - \omega_{qb} - \omega_{cav} - \chi$ and $\Delta_c = \omega_c - \omega_{cav} - \chi$.

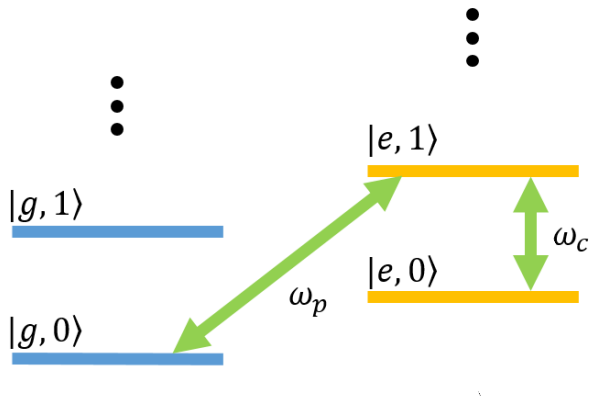

Figure 3.3: Arrangement of energy levels and drives for single probe drive modelling

Starting with the JC Hamiltonian in the dispersive regime, ω_p and ω_c drives are added. After restricting ω_c to only excite the $|e,n\rangle \rightarrow |e,n+1\rangle$ transition, and not allowing it to interact with $|g,n\rangle \rightarrow |g,n+1\rangle$, a rotating frame approximation is applied. Finally, dropping the fast rotating terms, the Hamiltonian is left time independent and the model from Novikov et al. is reached:

$$\begin{aligned} H = n(-\Delta_c - 2\chi)\,|g,n\rangle\langle g,n| - (\Delta_p - (n-1)\Delta_c)\,|e,n\rangle\langle e,n| \\ + \frac{\Omega_c}{2}\sqrt{n-1}\,|e,n+1\rangle\langle e,n| + \frac{\Omega_p}{2}\,|e,n+1\rangle\langle g,n| + H.C. \end{aligned} \tag{3.1}$$

where $|g, n\rangle$ ($|e, n\rangle$) denotes the number state of the cavity while the qubit is in the ground (excited) state, and Ω_c and Ω_p in MHz. The Hamiltonian was solved using the Lindbald master equation solver in Qutip [28] with $n_{max} = 8$, modelling the decay rates of the qubit and cavity ($\Gamma = 0.04$MHz and $\kappa = 2.9$MHz, respectively) as collapse operators.

Sweeping Δ_p and Ω_c with $\chi = -4.1$MHz, $\Delta_c = 0$ and $\Omega_p = 0.65$MHz there is a splitting of excited state which increases as Ω_c increases (Figure 3.4**(a)**). The splitting in the excited state population of the qubit is the signature of CPT. When $\Omega_c \gg \Omega_p$, the dark state of the of the system is $|g\rangle$ (Equation 2.38). Therefore, as Ω_c is increased, the system is trapped in $|g\rangle$ and no qubit excited state population is seen.

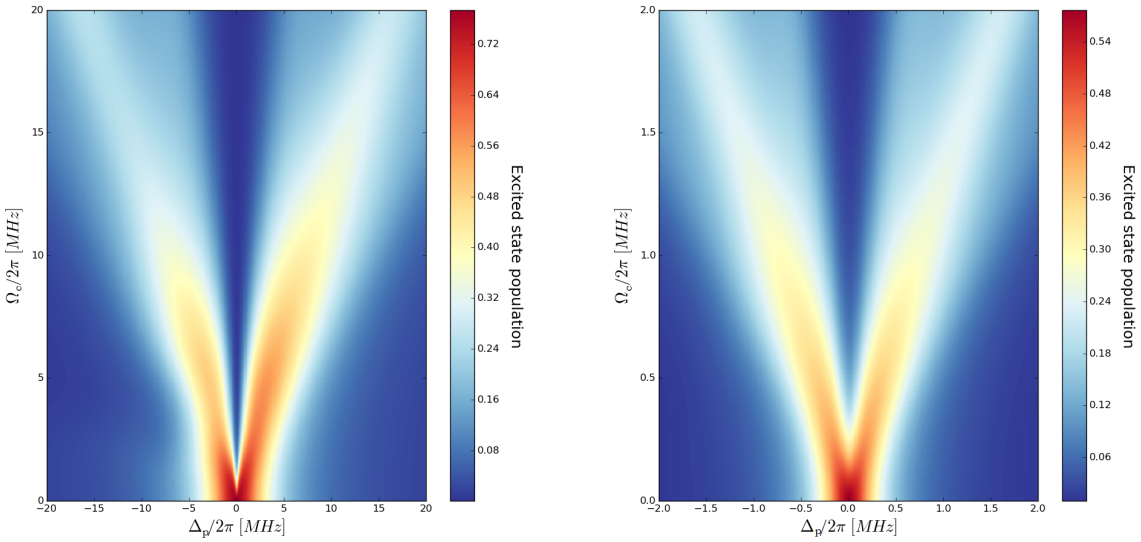

(a) (b)

Figure 3.4: Qubit excited state population in steady state, demonstrating CPT. **(a)** Using $\chi = -4.1$MHz from Novikov et al. with $\Delta_c = 0$ and $\Omega_p = 0.65$MHz. **(b)** Using parameters from system used in experimentation the simulation is repeated with $\Omega_p = 1$MHz.

Figure 3.4**(b)** shows DIT for the experimental system with $\Omega_c = 1MHz$. System parameters ($\Gamma = 62.5MHz$, $\kappa = 250MHz$ and $\chi = 1.05MHz$) are obtained from low power characterization of the cavity-qubit system (Section 4). Due to the smaller κ and Γ, the splitting occurs at Ω_c 10 times smaller than for system used by Novikov et al. Unlike Figure 3.4**(a)**, the two branches of the splitting are not uneven in strength. This is most

likely due to κ/Γ being an order of magnitude less in the experimental system ($\kappa/\Gamma \sim 10$) than the system used by Novikov et al. ($\kappa/\Gamma \sim 100$).

Increasing Ω_c also causes the $|f\rangle$ state to broaden, which broadens the line width of of the excited state as well as the line width of the CPT. This is shown through increased splitting in the excited qubit state peaks as Ω_c is increased. The splitting in the excited state population is linear for both systems, following Equation 3.2. It is dependent only on Ω_c, not Ω_p.

$$Splitting = (1.9135 \pm 0.0316)\Omega_c + (0 \pm 4.75 \times 10^{-6}) \tag{3.2}$$

where the splitting and Ω_c are in GHz. Each peak moves approximately $\pm\Omega_c$ away from the two photon transition frequency.

Holding Ω_c and Ω_p constant and varying Δ_c and Δ_p, the DIT becomes apparent (Figure 3.5). The quantum transition probability amplitudes of $|g\rangle \leftrightarrow |f\rangle$ and $|e\rangle \leftrightarrow |f\rangle$ interfere transmission of ω_p. When this occurs, ω_p no longer excites the $|g\rangle \leftrightarrow |f\rangle$ transition. Without this, the system does not reach $|e\rangle$ or $|f\rangle$ and no qubit excited state population is seen, the splitting seen in Figure 3.5.

DIT occurs when the dark state exists, demonstrated by a suppression in steady state population of the qubit. DIT was simulated for both the system parameters in [42] (Figure 3.5**(a)** and **(b)**) and from the experimental system (Figure 3.5**(c)** and **(d)**).

The DIT simulations were run for two different Ω_p values for each system. It can be seen that changing Ω_p only changes the line width of the excited state, without altering the slope of the DIT line. It also does not change the splitting of the line width, only makes the supression more shallow.

Looking at line cuts of the DIT results (Figure 3.6), it can be seen that the suppression of the excited state of the qubit moves with Δ_c. The line cuts are plotted for Ω_c= 5MHz and Ω_p= 0.30. The suppression occurs when $\Delta_c = \Delta_p$; the suppression moves with a slope of $1^{\mathrm{GHz}}/_{\mathrm{GHz}}$. When $\Delta_c = 0$, the supression in the population of excited state occurs in the middle of the linewidth.

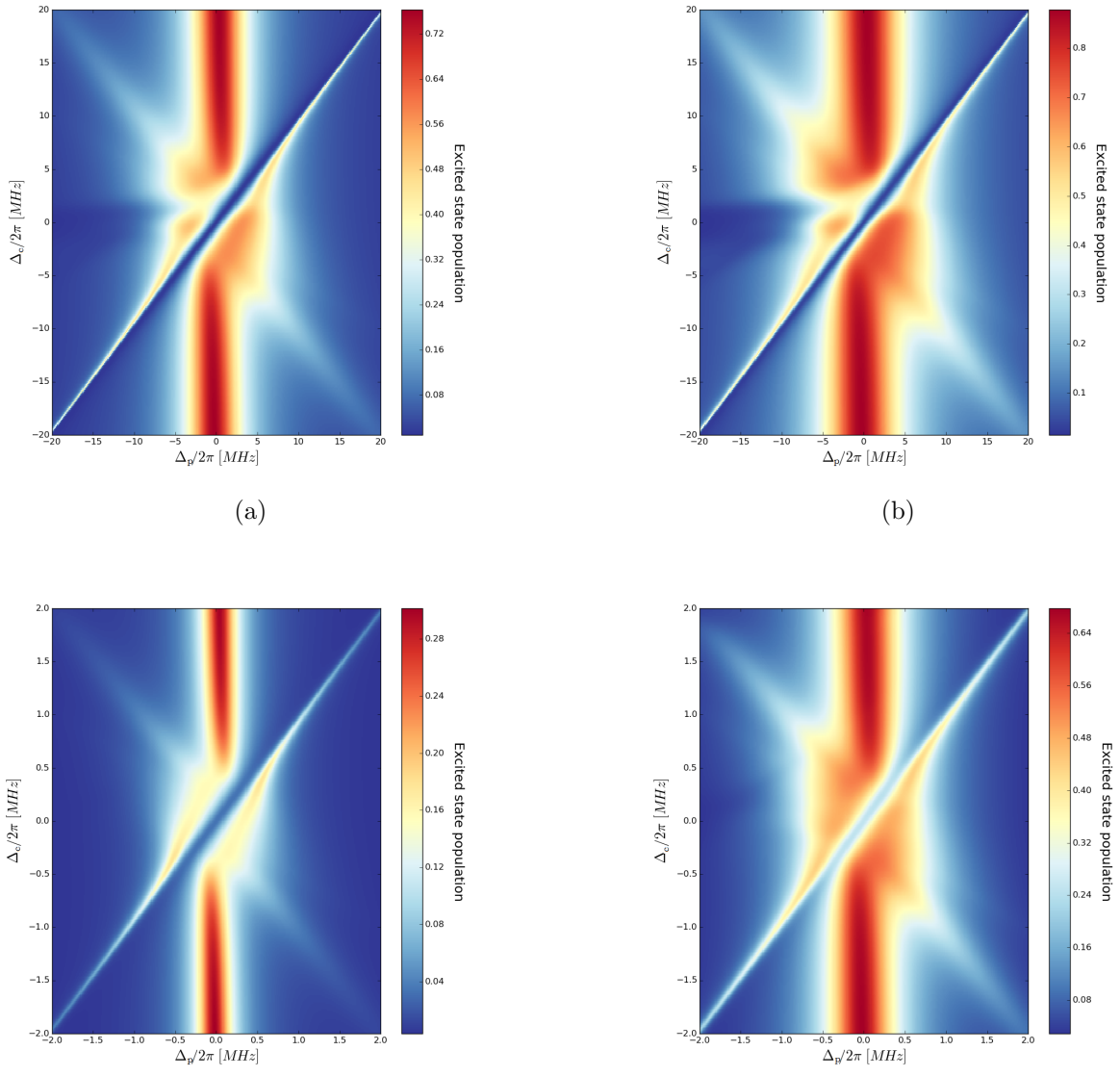

Figure 3.5: Qubit excited state population in steady state with $\Omega_c = 5$MHz and **(a)**$\Omega_p = 0.65$MHz and **(b)** Ω_p= 1MHz using system parameters from Novikov et al. **(c)** and **(d)** The same simulations using the parameters from the cavity-qubit system used in this experiment. Ω_c= 0.5MHz and Ω_p= 0.1MHz (a) and 0.3MHz (b). The suppression of the excitation to the excited state is DIT, where the system is trapped in the dark state, $|g\rangle$.

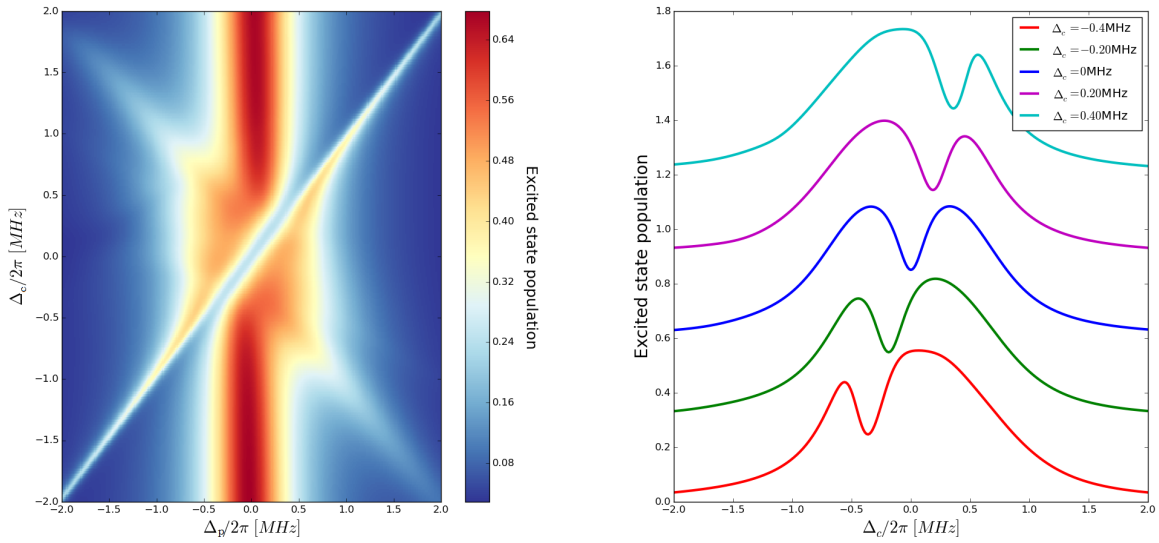

(a) (b)

Figure 3.6: **(a)** Qubit excited state population in steady state with $\Omega_c = 5$MHz and two $\Omega_p = 0.30$MHz drives. **(b)** Linecuts of (a) showing suppression of the excited state population. The suppression of the excited state shifts linearly with ω_c

3.2 Two Probe Drives

To fully investigate the system, the effects of detuning the probe drive needed to be modelled. Following a similar derivation for a three-level system in [27], the two-photon RWA Hamiltonian can be derived by restricting the subspace to the three levels of the lambda system: $|g,0\rangle = |g\rangle$, $|e,0\rangle = |e\rangle$, and $|e,1\rangle = |f\rangle$ (Figure 3.7). The Hamiltonian of the lambda system becomes:

$$H_\lambda = \begin{pmatrix} E_g & 0 & 0 \\ 0 & E_e & 0 \\ 0 & 0 & E_f \end{pmatrix} \tag{3.3}$$

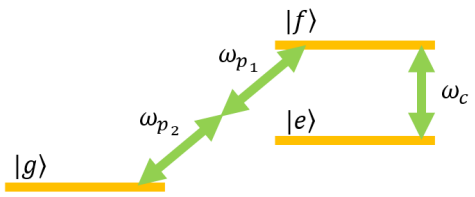

Figure 3.7: Arrangement of energy levels in the lambda system.

The transition frequencies between energy levels are then defined as $\hbar\omega_{gf} = E_f - E_g$ and $\hbar\omega_{ef} = E_f - E_e$.

This system uses three drives. The coupler driving the $|e\rangle \leftrightarrow |f\rangle$ with frequency ω_c and amplitude Ω_c, and probe driving the $|g\rangle \leftrightarrow |f\rangle$ transition. In contrast to Section 3.1, ω_p drives ω_{p_1} and ω_{p_2} are used. These can be detuned individually, and driven at two different and Rabi drive frequencies Ω_{p_1} and Ω_{p_2}.

$$H_{drive} = \Omega_c \cos\omega_c t \begin{pmatrix} 0 & 0 & 0 \\ 0 & 0 & 1 \\ 0 & 1 & 0 \end{pmatrix} + \Omega_{p_1} \cos\omega_{p1} t \begin{pmatrix} 0 & 0 & 1 \\ 0 & 0 & 0 \\ 1 & 0 & 0 \end{pmatrix} + \Omega_{p_2} \cos\omega_{p_2} t \begin{pmatrix} 0 & 0 & 1 \\ 0 & 0 & 0 \\ 1 & 0 & 0 \end{pmatrix} \tag{3.4}$$

The total Hamiltonian is the sum of Equations 3.3 and 3.4. Letting the state of the system $\Psi = c_0 |g\rangle + c_1 |e\rangle + c_2 |f\rangle$, the Schrödinger equation can be written as

$$\begin{pmatrix} H_{00} & H_{01} & H_{02} \\ H_{10} & H_{11} & H_{12} \\ H_{20} & H_{21} & H_{22} \end{pmatrix} \begin{pmatrix} c_0 \\ c_1 \\ c_2 \end{pmatrix} = i\hbar \begin{pmatrix} \delta_t c_0 \\ \delta_t c_1 \\ \delta_t c2 \end{pmatrix} \tag{3.5}$$

where $\delta_t c_i$ is the time derivative of c_i.

Using the rotating frame approximation, $\tilde{c}_i = e^{i\phi_i(t)} c_i \rightarrow \tilde{\Psi} = \tilde{c}_0 |g\rangle + \tilde{c}_1 |e\rangle + \tilde{c}_2 |f\rangle$, $i = 0, 1, 2$, the following relation can be found:

$$\begin{aligned} i\hbar\delta_t\tilde{c}_0 &= i\hbar e^{i\phi_0}\delta_t\tilde{c}_0 - \hbar\delta_t\phi_0 c_0 e^{i\phi_0} \\ &= (H_{00} - \hbar\delta_t\phi_0)c_0 + H_{01}e^{i(\phi_0-\phi_1)}\tilde{c_1} + H_{02}e^{i(\phi_0-\phi_2)}\tilde{c}_2 \end{aligned} \tag{3.6}$$

which defines $\tilde{H}_{00} = H_{00} - \hbar\delta_t\phi_0$, $\tilde{H}_{01} = H_{01}e^{i(\phi_0-\phi_1)}$, and $\tilde{H}_{02} = H_{02}e^{i(\phi_0-\phi_2)}$. Following a similar derivation the form of the time transformed Hamiltonian becomes

$$\tilde{H} = \begin{pmatrix} H_{00} - \hbar\delta_t\phi_0 & H_{01}e^{i(\phi_0-\phi_1)} & H_{02}e^{i(\phi_0-\phi_2)} \\ H_{10}e^{i(\phi_1-\phi_0)} & H_{11} - \hbar\delta_t\phi_1 & H_{12}e^{i(\phi_1-\phi_2)} \\ H_{20}e^{i(\phi_2-\phi_0)} & H_{21}e^{i(\phi_2-\phi_1)} & H_{22} - \hbar\delta_t\phi_2 \end{pmatrix} \tag{3.7}$$

Here, the choise of ϕ_i, is important to simplify the equation. Choosing

$$\phi_0 = {}^{E_g t}/_{\hbar} \tag{3.8}$$

$$\phi_1 = ({}^{E_g}/_{\hbar} + {}^{(\omega_{p_1} + \omega_{p_2})}/_2 + \omega_c)t \tag{3.9}$$

and

$$\phi_2 = ({}^{E_g}/_{\hbar} + {}^{(\omega_{p_1} + \omega_{p_2})}/_2)t \tag{3.10}$$

Defining the detunings $\Delta_c = \omega_c - \omega_{ef}$, and $\Delta_p = {}^{(\omega_{p_1} + \omega_{p_2})}/_2 - {}^{\omega_{gf}}/_2$, the final Hamiltonian becomes:

$$\tilde{H} = \begin{pmatrix} 0 & 0 & \frac{\Omega_{p_1}}{2}k_1 + \frac{\Omega_{p_2}}{2}k_2 \\ 0 & \Delta_p + \Delta_c & \frac{\Omega_c}{2}(1 + e^{i2\omega_c t}) \\ \frac{\Omega_{p_1}}{2}k_1^* + \frac{\Omega_{p_2}}{2}k_2^* & \frac{\Omega_c}{2}(1 + e^{-i2\omega_c t}) & \Delta_p \end{pmatrix} \tag{3.11}$$

where

$$k_1 = (e^{i\omega_{p_1} t/2} + e^{-i3\omega_{p_1} t/2})e^{-i\omega_{p_2} t/2} \tag{3.12}$$

$$k_2 = (e^{i\omega_{p_2} t/2} + e^{-i3\omega_{p_2} t/2})e^{-i\omega_{p_1} t/2} \tag{3.13}$$

When the probe drive frequencies are equal in drive strength and frequency, the fast rotating terms can be dropped, as in Section 2.4.3, and the Hamiltonian becomes

$$\tilde{H} = \begin{pmatrix} 0 & 0 & \Omega_p \\ 0 & \Delta_p + \Delta_c & \frac{\Omega_c}{2} \\ \Omega_p & \frac{\Omega_c}{2} & \Delta_p \end{pmatrix} \tag{3.14}$$

which can be shown to be equivalent to Equation 3.1 with double the probe drive strength, when Equation 3.1 is restricted to only the three states $|g, 0\rangle$, $|e, 0\rangle$, and $|e, 1\rangle$.

To determine the validity of the model, the model is used to simulate the CPT experiment, using the parameters in [42]. A RWA is made by dropping the fast oscillating terms, $e^{\pm i3\omega_{c_{1/2}} t/2}$. The steady state of the time-dependent Hamiltonian is solved by first finding the propagator of the system and then using that to find the steady state. This is then compared to the results of the model in [42], restricting to $n = 2$. The results in Figure 3.8, show that the two models give the same steady state solution. Therefore, the model is accepted as valid.

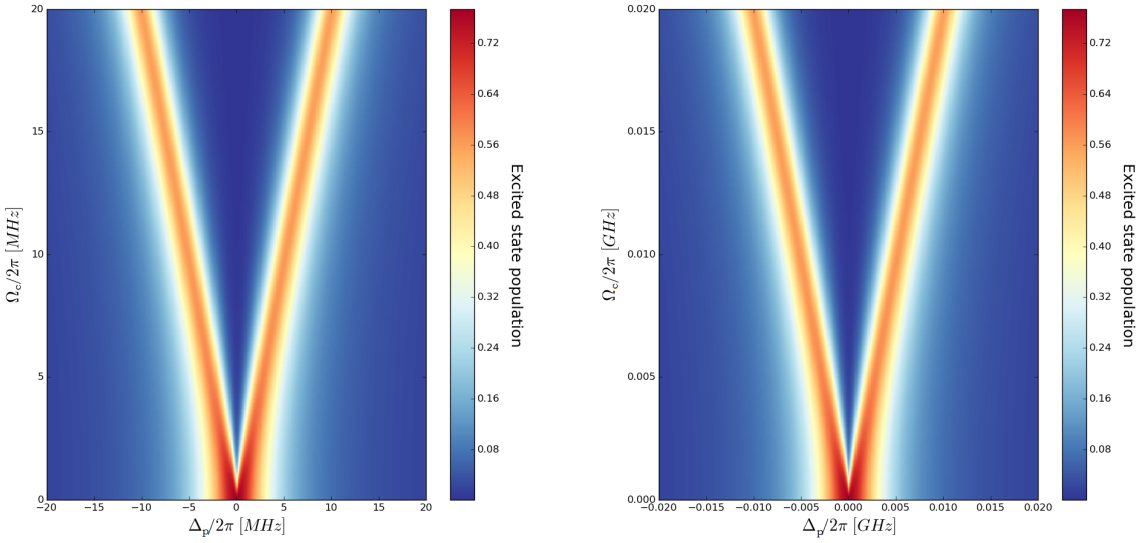

(a) (b)

Figure 3.8: CPT simulations. **(a)** Following the single probe drive model from Koch et al. restricting to $n_{max} = 2$. **(b)** Simulation using two probe drive model. It can seen to be the same as the single drive model, when it is restricted to only 2 cavity energy levels.

Detuning the two photon transition, the frequency of probe probes are linearly dependent on eachother, with a slope of $-1 \pm 0.0000027^{\text{Hz}}/_{\text{Hz}}$, Figure 3.9: detuning one probe drive by $+\Delta_p$ requires the other probe to be detuned by $-\Delta_p$ from the two photon transition frequency. The line width of the excited state is determined by the strength of the probe drive, Figure 3.10**(b)**.

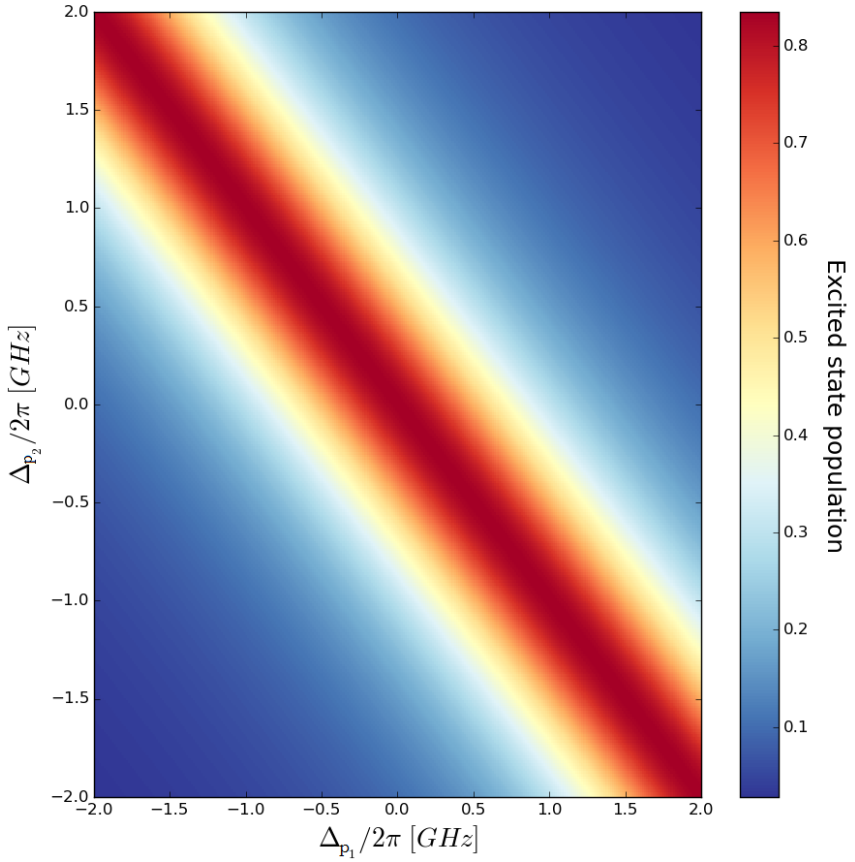

Figure 3.9: The frequency of each detuned probe drive are linearly dependent on each other, with a slope of $-1 \pm 0.00000027^{\text{Hz}}/_{\text{Hz}}$. The steady state population of the qubit excited state for $\Omega_p = 0.8$MHz and no coupler drive. The linewidth of this transition is dependent on the strengths of the drives.

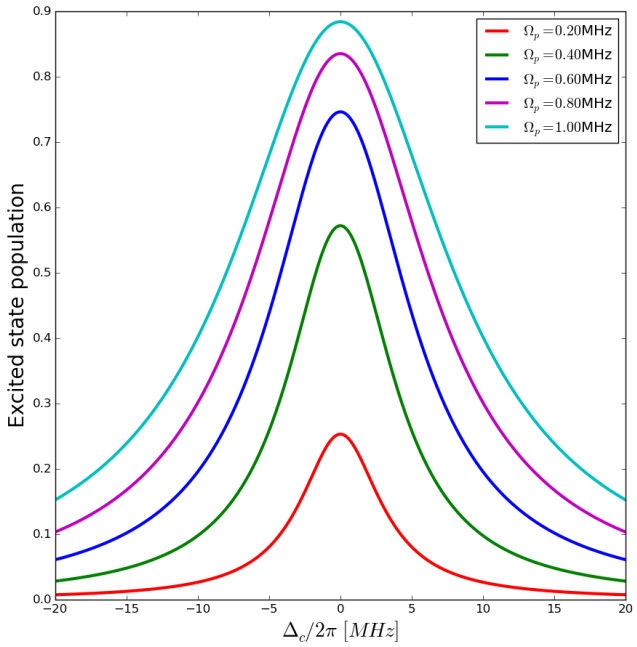

(a)

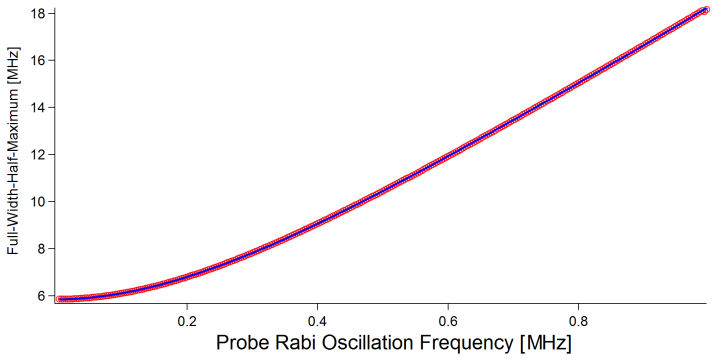

(b)

Figure 3.10: Linewidth dependence on probe drive strength. **(a)** Steady state population of the excited state of the qubit for different Ω_p. Increasing Ω_p increases the steady state population but also broadens the linewidth. **(b)** FWHM for various Ω_p. The FWHM changes as $(5.8494 \pm 0.00283) + (0.11371 \pm 0.039)\Omega_p + (27.828 \pm 0.158){\Omega_p}^2 - (23.051 \pm 0.238){\Omega_p}^3 + (7.5422 \pm 0.118){\Omega_p}^4$ where Ω_p is in MHz.

Moving into the time domain, simulations were run to determine the effect of the detuned drives. The time domain simulations were run with no ω_c, so that no interference from ω_c is included in the system. When both drives equal in frequency and drive strength ($\Delta_{p_1} = \Delta_{p_2} = 0$ and $\Omega_{p_1} = \Omega_{p_2} = 1$MHz), the steady state population of the qubit is 0.8 (blue line of Figure 3.11**(a)**). Decreasing Ω_{p_2} to 0.01MHz (Figure 3.11**(b)**), the steady state also decreases, but remains close to 0.8, indicating that the maximum qubit excited state population is 0.8, and a single ω_p of $\sim$ 1MHz is required to achieve it. The oscillations in the qubit excited state population when the drives are initially turend on also decrease with the decrease of Ω_{p_2}. This is because when Ω_{p_2} is decreased, the amplitude of the oscillations from ω_{p_2} decrease. Therefore, they interfere less with the oscillations driven by ω_{p_1}, and the total oscillation frequency decreases.

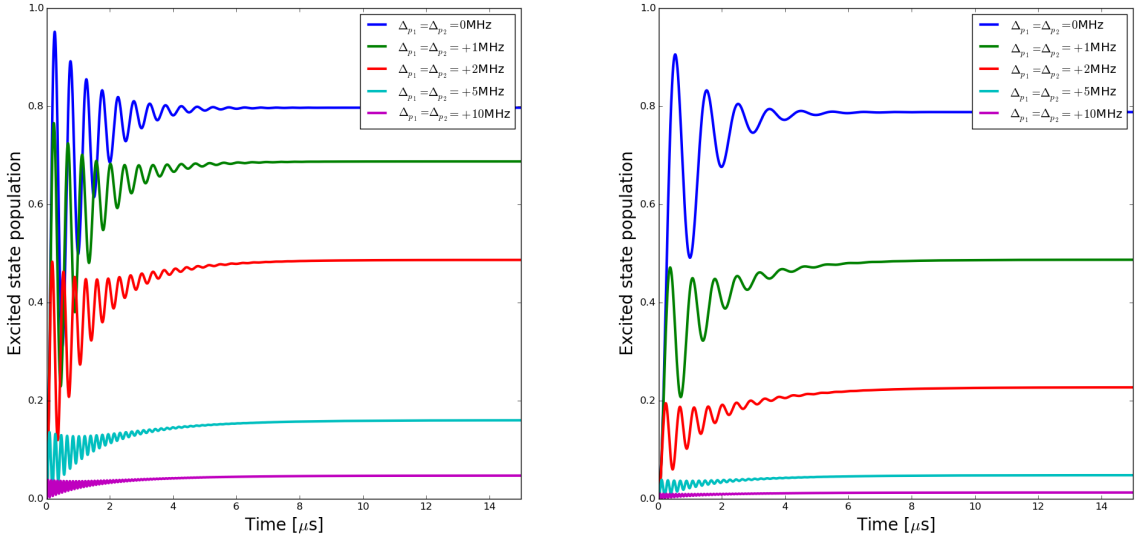

(a) (b)

Figure 3.11: Time dynamics with detuned ω_{p_1} and ω_{p_2}. As the detuning in the drive is increased, the steady state population decreases. **(a)** $\Omega_{p_1} = \Omega_{p_2} = 1$MHz **(b)** $\Omega_{p_1} = 1$MHz $\Omega_{p_2} = 0.01$MHz. Decreasing Ω_{p_2} decreases the frequency of oscillations when the drives are first turned on.

Detuning ω_{p_1} and ω_{p_2} by the same amount ($\Delta_{p_1} = \Delta_{p_2}$), decreases the steady-state population of the qubit, matching results from the steady-state simulations. Again, decreasing Ω_{p_2} to 0.01MHz (Figure 3.11**(b)**) decreases the steady state population achieved

at each detuning, but by a greater amount.

If, instead, ω_{p_2} is detuned in the opposite direction from ω_{p_1} ($\Delta_{p_1} = -\Delta_{p_2}$) the steady-state population of 0.8 is recovered, as seen in the green line Figure 3.12**(a)**, simulated with $\Delta_{p_1} = -\Delta_{p_2} = 1$MHz and $\Omega_{p_1} = \Omega_{p_2} = 1$MHz. As the detuning is increased to 2MHz and 5MHz, (Figure 3.12**(b)** and **(c)**, respectively), detuning the drives as $\Delta_{p_1} = -\Delta_{p_2}$ still recovers the qubit steady-state population of 0.8. This agrees with the predictions seen in Figure 4.28 for steady-state.

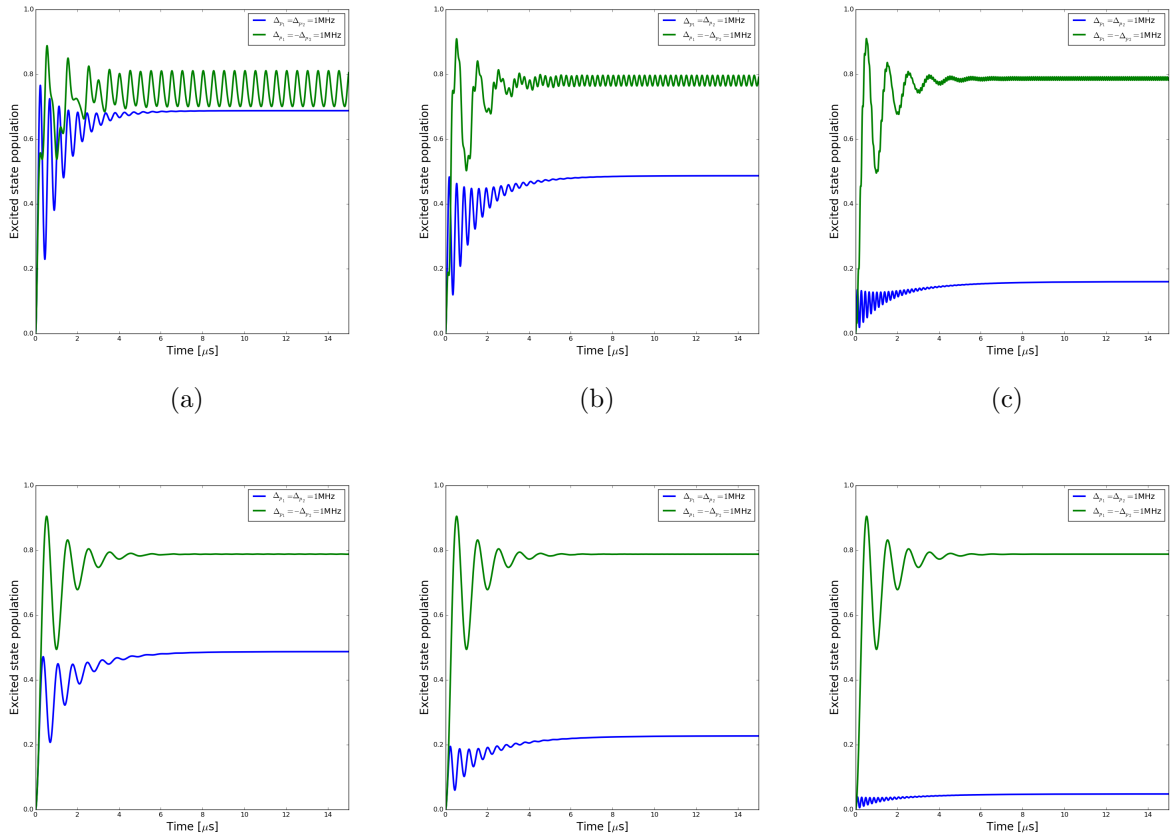

(a) (b) (c)

(d) (e) (f)

Figure 3.12: Time dynamics for $\Delta_{p_1} = \Delta_{p_2}$ (blue) and $\Delta_{p_1} = -\Delta_{p_2}$ (green). When $\Delta_{p_1} = -\Delta_{p_2}$ the steady-state population of the qubit is recovered. **Top row:** $\Omega p_1 = \Omega p_2 1$MHz with Δ_{p_1} = **(a)** 1MHz, **(b)** 2MHz and **(c)** 5MHz. **Bottom row:** Ωp_1 = 1MHz and $\Omega p_2 = 0.01$MHz with Δ_{p_1} = **(d)** 1MHz, **(e)** 2MHz and **(f)** 5MHz.

Increasing the overall detuning decreases the amplitude of the fast oscillations in the steady state population. This is expected as the relative frequency difference between the two drives increases, and over time the oscillations average away.

Decreasing Ω_{p_2} to 0.01MHz, as seen in Figure 3.12**(d)**-**(f)**, the steady-state population of 0.8 is still recovered, but with a smaller amplitude of oscillations in the steady-state.

Finally the system is used to simulate the microwave transistor experiment. In Figure 3.13, ω_{p_1} is turned on for the first 15μs with $\Omega_{p_1} = 1$MHz, without ω_{p_2}. This is enough time for the qubit population to reach steady-state. $\Delta_{p_1} = -\Delta_{p_2}$ is chosen such that no significant qubit excited state population is achieved with only ω_{p_1}. Then, ω_{p_2} is pulsed on for the next 15μs and then turned off again. During the pulse, the qubit excited state population jumps to 0.8, and then returns to the steady state population driven by ω_{p_1} with decay rate Γ. Again, decreasing Ω_{p_2} does not change the steady state population (Figure 3.13**(b)** and **(c)**), but decreases the amplitude of the fast oscillations in the steady-state population.

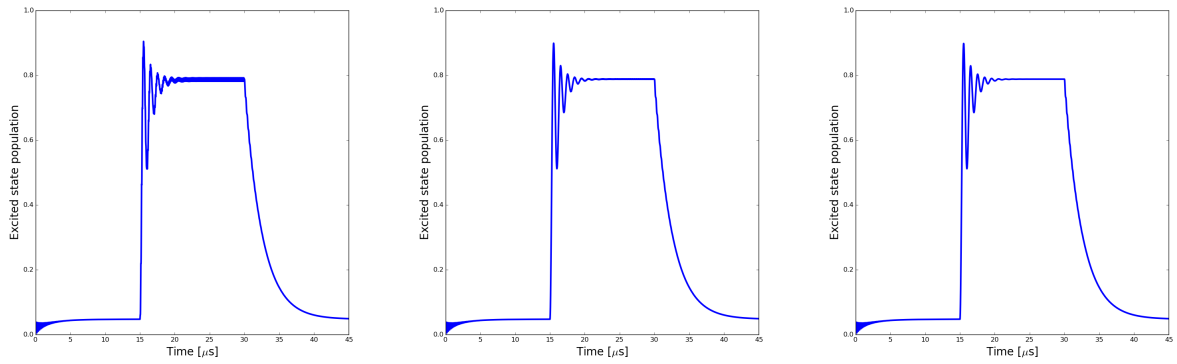

(a) (b) (c)

Figure 3.13: Time dynamics of a pulsed ω_{p_2} with $\Delta_{p_1} = -\Delta_{p_2} = 5$MHz and $\Omega_{p_1} = 1$MHz. ω_{p_2} is pulsed on from 15μs to 30μs. During this time Once ω_{p_2} is turned off, the steady state population decays with the rate Γ. Decreasing Ω_{p_2} from **(a)** 1MHz to **(b)** 0.01MHz and **(c)** 0.1kHz shows no decrease in the steady-state population, and a decrease in the amplitude of the fast oscillations in the steady-state.

These results indicate that the system could work with uneven Ω_{p_1} and Ω_{p_2}. Since a steady-state population of 0.8 was still achieved with infinitely small Ω_{p_2}, the model indicates that the system could work in the single photon regime.

Chapter 4

Experiment

4.1 Device and Fridge Setup

The experiment used an aluminum 3D transmon fabricated on a silicon wafer. The JJ was fabricated using double angle evaporation and produced an $^{E_J}/_{E_C}$ of ~ 190.

The transmon was placed in a 3D aluminum cavity, as shown in Figure 2.11. The cavity is $2.7cm \times 3.15cm \times 4.2mm$ and is designed for a TE_{101} of 7GHz. The device was cooled in the bottom stage of a Blufors dry dilution refrigerator to approximately 10mK. The fridge is wired as shown in Figure 4.1, utilizing a transmission scheme for state detection. The circulators are connected so that signals pass from the 3D transmon up line A, but are blocked from going down line A back to the transmon. Lastly, the 1dB attenuator is included on line A to prevent standing waves forming between the circulators and the measurement equipment.

Drive strengths are reported at room temperature, with a nominal 78dB of attenuation to the device, including losses due to cables. Any attenuations reported are in additional to this attenuation.

The digitizer uses a heterodyne detection scheme. For microwave equipment setups see Appendix B.

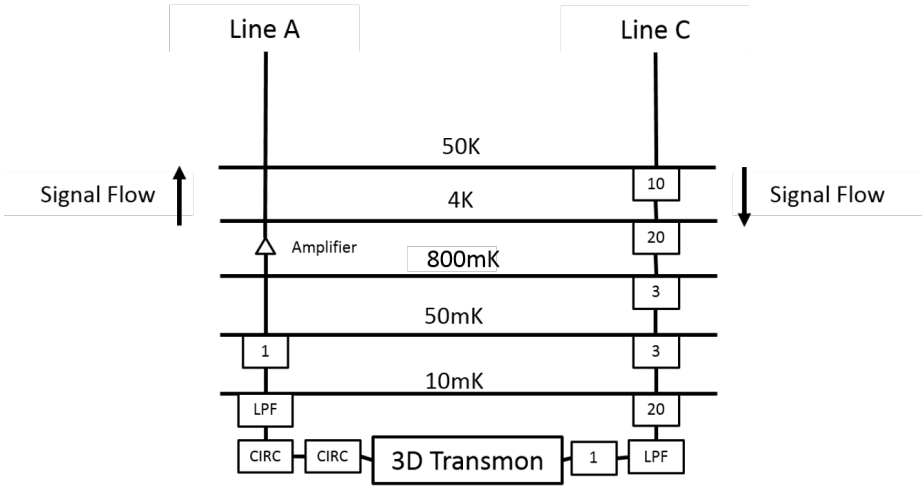

Figure 4.1: The wiring of the fridge used in experimentation. The levels represent the temperature stages in the fridge. Rectangles with numbers represent alternators with the number representing the dB attenuation. The low pass filters (LPF) have a cutoff frequency of 8.5GHz. The circulators are denoted as CIRC. The amplifier is a high electron mobility transistor (HEMT) amplifier with an amplification of 27dB at room temperature.

4.2 Qubit Spectroscopy

Qubit spectroscopy is used to estimate the qubit frequency at higher drive frequencies as well as the higher order transition frequencies of the qubit. These higher order transitions are used to determine the anharmonicity of the qubit. Spectroscopy was conducted using a network analyzer at zero span to monitor the transmission of the cavity frequency, $\omega_{cav}+\chi$. This means that the netwrok anaylser takes multiple data points, all at the same frequency. Then, the frequency of a QuickSyn (QS) driven at 7dBm was swept. Monitoring the transmission magnitude, the qubit frequencies appear as reflections. This is because the frequency $\omega_{cav}+\chi$ corresponds to the qubit in the ground state. When the qubit is in the excited state, the cavity frequency shifts to $\omega_{cav}-\chi$ and $\omega_{cav}+\chi$ is reflected, rather than transmitted through the cavity.

At low coupler powers, only f_{01} is apparent. Figure 4.2**(a)** shows the qubit spectra for a coupler strength of -40dBm. Fitting a Lorenzian lineshape to the absoption spectrum shows that $f_{01} = 6.1159 \pm 0.000468$GHz.

Although high coupler drives causes an ac-Stark shift in the qubit frequencies [53], it is necessary to find the higher order qubit transitions. Figure 4.2**(b)** shows transmission

frequencies for $|0\rangle \leftrightarrow |1\rangle$, $|1\rangle \leftrightarrow |2\rangle$, and $|0\rangle \leftrightarrow |2\rangle$ for a 3dBm probe. Since each of the qubit transitions couple to cavity with different strengths [34], the linewidth of each of these transitions is different.

The absorption line of $|0\rangle \leftrightarrow |1\rangle$ broadened due to the higher prob strength and shifted down, as expected for an ac-Stark shift, to $f_{01} = 5.971 \pm 0.000124$GHz. The next transition $|1\rangle \leftrightarrow |2\rangle$ is the adsorption line to the right of the $|0\rangle \leftrightarrow |1\rangle$ adsorption line. This is because the anharmonicity of a transmon is greater than 1 (Equation 2.19) and therefore $f_{12} > f_{01}$. The $|1\rangle \leftrightarrow |2\rangle$ transition frequency is $f_{12} = 6.1278 \pm 0.00161$GHz.

The final transition, $|0\rangle \leftrightarrow |2\rangle$, is a two photon transition for a transmon; therefore, the adsorption line appears at $f_{02}/2$. The transition frequency for $|0\rangle \leftrightarrow |2\rangle$ was determined to be $f_{02}/2 = 5.8039 \pm 0.000124$GHz.

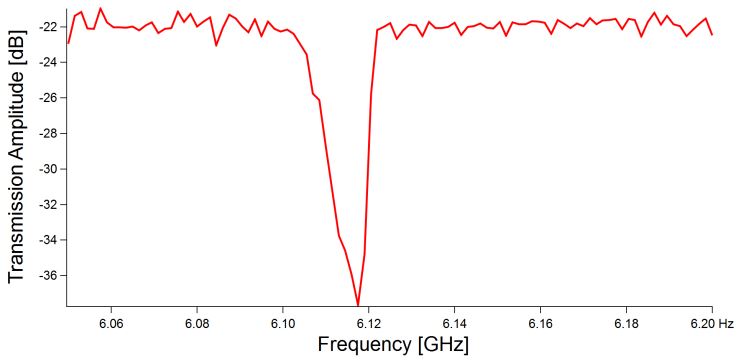

(a)

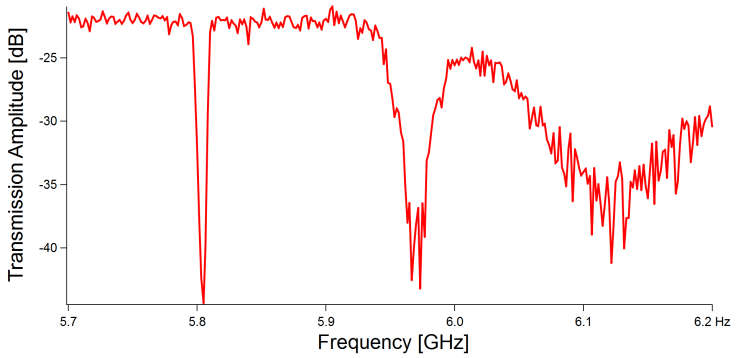

(b)

Figure 4.2: Qubit spectroscopy. **(a)** is a linecut at a coupler power of -40dBm. Only the first transition is shown and was determined to be $f_{01} = 6.1159 \pm 0.000468$GHz. **(b)** shows a line-cut for a coupler power of 3dBm. The three resonant curves show the first transitions of of the qubit: $f_{01} = 5.971 \pm 0.000124$GHz, $f_{12} = 6.1278 \pm 0.00161$GHz and $f_{02}/2 = 5.8039 \pm 0.000124$GHz.

4.3 Low Power Readout

Two readout schemes, a low power and a high power, are possible based on the nonlinear effects the qubit state has on the resonance frequency of the cavity. These schemes differ in power and contrast. The first low power readout has a lower contrast but can be used in a wider variety of experiments. Both schemes use the transmission of a coherent microwave pulse through a cavity, although the length of the high power pulse is shorter. The response of the cavity to the pulse is integrated over the pulse time, and this is used to determine the state of the qubit.

The low power readout scheme is based on shift of resonant frequency, $\pm\chi$ in Equation 2.36. When the qubit is in the ground state, the cavity is resonate at $\omega_{cav}+\chi$, but shifts to $\omega_{cav}-\chi$ when the qubit is in the excited state. Choosing one of these two frequencies, will readout the ground state or excited state of the cavity.

Two methods can be used, depending on whether the readout will be in the magnitude or phase of the signal [22][53]. If the phase response is used, the readout frequency is chosen to be the peak of the resonant magnitude curve, red line in Figure 4.3**(a)**. Here, there will be maximal difference in phase between the qubit in the excited or ground states.

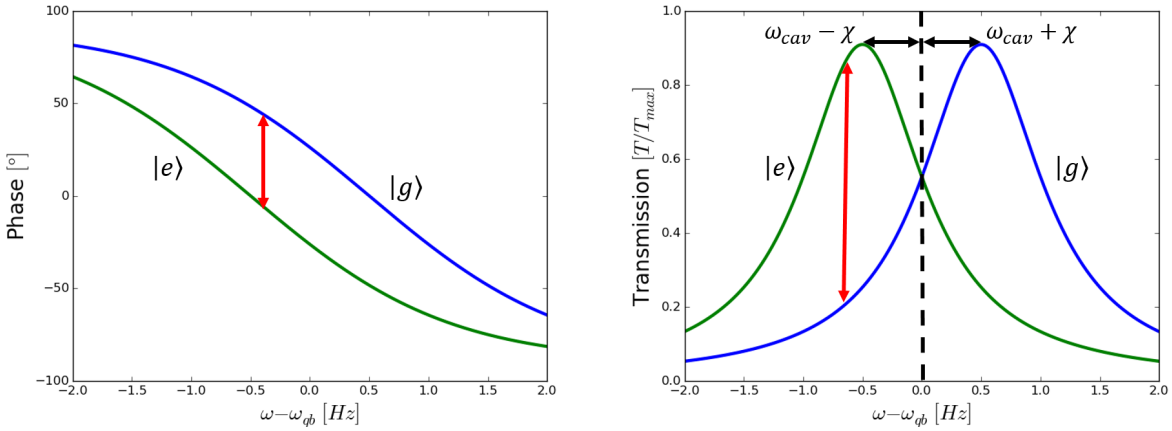

(a) (b)

Figure 4.3: Phase **(a)** and magnitude **(b)** transmission responses of the cavity with the qubit in the excited (green) and ground (blue) states. Maximum distinguishability of states for either magnitude or phase occurs at the red line.

To monitor the transmission magnitude, the maximal difference in response does not

occur at the peak of the resonant response, but at a frequency a little to one side or the other, red line in Figure 4.3**(b)**. When the qubit is in the other state the resonance response narrows, instead of fully disappearing so the largest magnitude difference appears slightly off resonance. If reflection experiments are used then the same readout frequency choice is used for the dips in reflected signal magnitude.

To find the frequency at which to do low power readout, a network analyzer was used to send and monitor a microwave drive, near the the expected cavity frequency, 7GHz, at -60dBm. A second microwave drive, supplied by a QS, is used to drive the qubit at the frequency determined in Section 4.2 at -5dBm (see Appendix B for equipment setup).

The transmitted magnitude of the cavity coupler is shown in Figure 4.4. The qubit drive creates a mixed qubit state of $|0\rangle$ and $|1\rangle$, producing two resoance peaks at $\omega_{cav} \pm \chi$. Fitting Lorenzian curves to the two peaks gives $\omega_{cav}/2\pi - \chi/2\pi = 7.0779 \pm 0.000124$GHz and $\omega_{cav}/2\pi + \chi/2\pi = 7.0800 \pm 0.0000957$GHz. χ can then be determined to be $\chi = 1.05 \pm 0.2197$MHz.

Due to a constant time dependent phase shift between the microwave source and digitizer, the magnitude response was used instead of the phase.

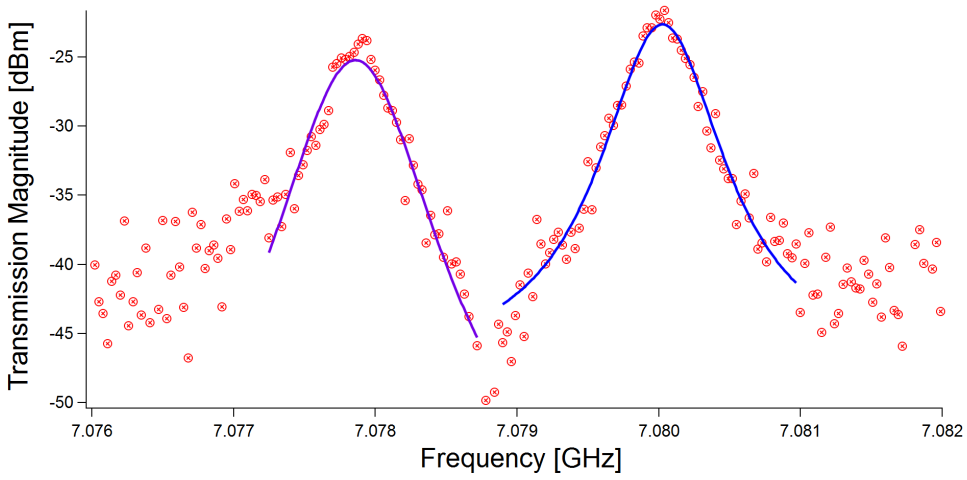

Figure 4.4: Magnitude response cavity while driving the qubit, causing it to be in a mixed state of $|0\rangle$ and $|1\rangle$. This causes resonance curves at $\omega_{cav}/2\pi \pm \chi/2\pi$ which were determined to be 7.0800 ± 0.00957GHz and 7.0779 ± 0.000124GHz, respectively. $\chi = 1.05 \pm 0.2197$MHz.

4.4 Punchout

A punchout scan is used to determine the presence of the qubit in the cavity. The qubit shifts the frequency of the cavity, but when probed with a strong enough power, the bare cavity frequency, ω_{bare}, is exposed. This is the frequency of the cavity without the qubit. The measurement is conducted by scanning both the frequency and power of a microwave probe. If a shift in resonant frequency is seen then it can be concluded that a qubit is present in the cavity.

Here, a network analyzer is used to send and monitor the transmission of the microwave signal. The punchout scan in Figure 4.5, shows the shift in frequency that is characteristic of a qubit-cavity system, the first indication that the qubit is present in the cavity. The second resonant frequency at low coupler power is from the nonlinearity in the cavity response due to driving the qubit at -10dBm, discussed in Section 4.3. A line-cut at a cavity coupler power of -60dBm from this scan is shown in Figure 4.4. At high powers, the bare cavity frequency, $\omega_{bare}/2\pi = 7.0760 \pm 0.000135$GHz, has almost complete transmission.

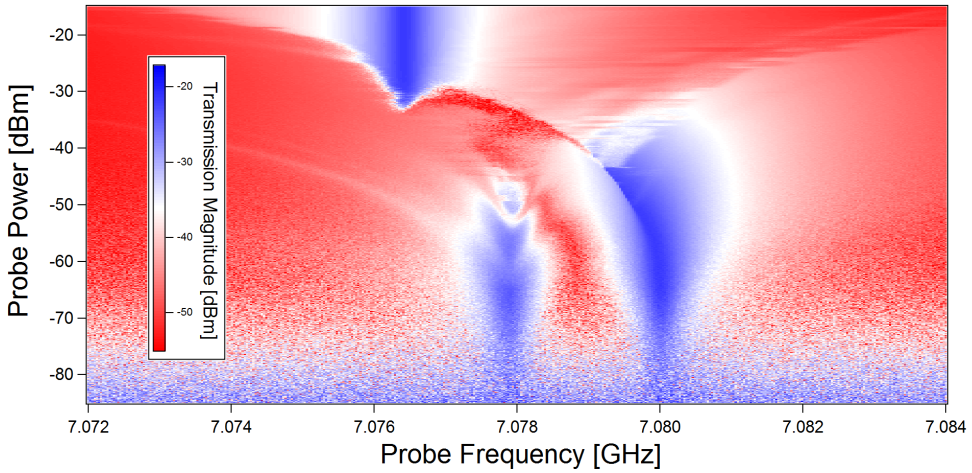

Figure 4.5: Punch-out scan of qubit cavity system with qubit drive on. $\omega_{qb}/2\pi = 6.2115$GHz at -10dBm, $\omega_{cav}/2\pi = 7.079$GHz, and $\omega_{bare}/2\pi = 7.0760 \pm 0.000135$GHz

Following [34], the coupling between the qubit and cavity was determined to be 56MHz. Since $g/(\omega_{cav} - \omega_{qb}) < 0.05$, the system is well described by the dispersive Jaynes-Cummings Hamiltonian, Equation 2.34.

4.5 High Power Readout

The second, high power, readout scheme is based on the Jaynes-Cummings non-linearity as described in [39]. This scheme relies on the qubit state dependent power at which the bare cavity frequency is exposed. When the qubit is in the excited state the transmission of bare cavity frequency occurs at a lower power. To readout the state of the qubit a coherent microwave pulse can be sent into the cavity at the bare cavity frequency and the power level which has the greatest distinction between levels. The magnitude of the transmitted wave indicates the state of the qubit.

To determine the power for readout, a 600ns readout pulse at ω_{bare} was sent through the cavity with no qubit drive to keep the qubit in the ground state. The transmitted magnitude of the pulse was then integrated over the pulse time to determine the readout magnitude.

Next, the process was repeated with the qubit in the excited state. This was completed by first sending in a π control pulse, determined by low power Rabi time-domain measurements (see Section 4.6.1 for discussion on the Rabi experiment) before the readout pulse and then reading out the state immediately.

Plotting the readout magnitude for different cavity powers, Figure 4.6, with the qubit in the ground and excited states, the optimal readout power can be determined. The maximal distinction in readout magnitude for the ground and excited states was determined to be -0.5dBm with 25dB of room temperature attenuation.

The contrast of the readout was determined using histogram data from the Rabi time-domain measurement, Section 4.6.1. A double Gaussian line shape is fit to the readout of the qubit in the $|0\rangle$ and $|1\rangle$ states, Figure 4.7. From this fit, area under the curve could be used to determine the percentage of incorrect measurements. Using this method there is a 80% contrast in the readout of the excited state and an 83% contrast in the readout of the ground state, Figure 4.7.

Some of the difference in contrast between the excited and ground state readout can be attributed to triggering errors. It was determined that a few of the pulses were missed on the AWG, causing false readings of $|0\rangle$. Increasing the number of pulses in a burst from 5 to 20 reduced this number, but no further reduction was seen by increasing the number of pulses further.

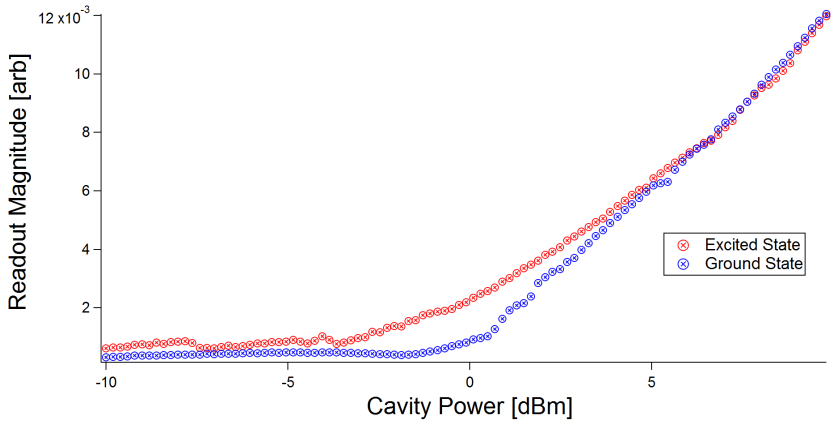

Figure 4.6: Readout magnitude of the transmitted coherent microwave pulse at the bare cavity frequency as a function of its power with and without the qubit drive. The optimal readout power is at -0.5dBm using 25dB of room temperature attenuation.

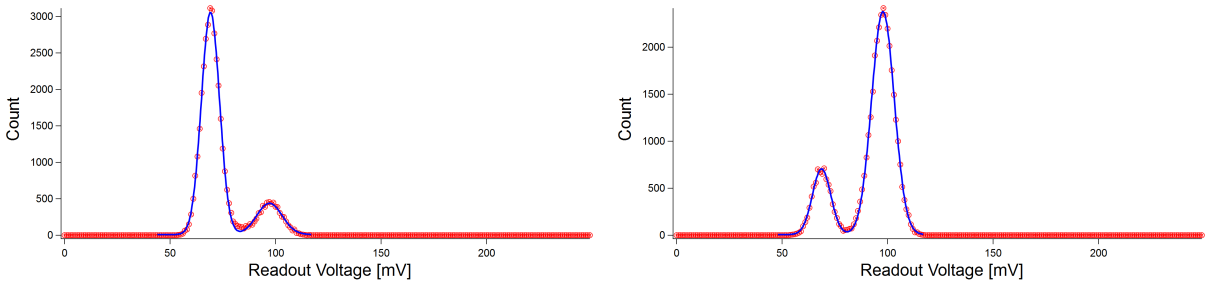

(a) (b)

Figure 4.7: Histogram data from when the qubit is prepared in the ground state **(a)** and excited state **(b)**. The ground state is read out with 83% contrast while the excited state has 80% contrast.

4.6 Time Domain Qubit Characterization

To characterize the time domain response of the system Rabi, Ramsey, T_1, and spin echo measurements were used [15]. Each measurement uses as series of microwave pulses from a signal generator (SigGen), at or near the qubit frequency to control the state of the qubit. Since the qubit frequency is above the maximum frequency of the signal generator, the signal from the SigGen is mixed with a 4GHz continuous wave microwave signal produced by a QS. A second QS is used for state readout. Results here are shown for the high power readout scheme (Section 4.5). See Appendix B for complete microwave equipment setup. Using noise measurements it was determined that the 4GHz signal was sufficiently filtered from the system (Appendix C).

It was determined that the qubit had a T_1 time of $\sim 17\mu$s and a T_2 time of $\sim 35\mu$s.

4.6.1 Rabi Oscillations and Readout Optimization

Imagining the microwave control pulse as rotations on the Bloch sphere, is useful in understanding control pulse sequences. The control pulses are equivalent to counter-clockwise rotations about the $|R\rangle$ axis of the Bloch Sphere (Section 2.3. The length of the control pulse determines the how far the state is rotated about this axis.

Rabi measurements are used to obtain the π and $\pi/2$ times for qubit control [46][11]. The π time is used to invert the population of the qubit, a rotation of 180° around the $|L/R\rangle$ axis on the Bloch sphere described in Section 2.3 from the $|0\rangle$ state to the $|1\rangle$ state. The $\pi/2$ pulse is used to initiate into the superposition state $1/\sqrt{2}\,(|0\rangle + |1\rangle)$. This is a rotation of 45° on the Bloch sphere.

The measurement changes the length of a microwave control pulse, t, driven at ω_{qb}. As t is increased, so is the rotation about the $|R\rangle$ axis. For a series of increasing t, if the state of the qubit is immediately readout after the control pulse this shows an increasing population of $|1\rangle$. Eventually, the qubit reaches $|1\rangle$, and increasing t further moves the state back towards $|0\rangle$, and is seen in experiment as decreasing population of $|0\rangle$.

Plotting the population of $|1\rangle$ for increasing t, an exponentially decaying sinusoid becomes apparent. The frequency of these oscillations determines $t(\pi)$ and $t(\pi/2)$. The decay rate is a mixture of T_1 and T_2 times, which is caused by the the state to relaxing from $|1\rangle$ to $|0\rangle$ as well dephasing, rotating around the $|R/+\rangle$ plane.

Figure 4.8 shows the microwave pulse sequence for the Rabi experiment: a control pulse (black line) at ω_{qb} with increasing length, t, followed immediately by readout.

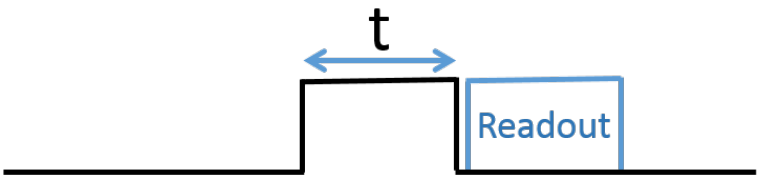

Figure 4.8: Microwave pulse sequence for Rabi measurements. The black line is the amplitude of the control microwave pulse. The time of the control pulse is increased and then the state of the qubit is read out for each time.

The results of the experiment are shown in Figure 4.9 in red markers. For this experiment, the $|0\rangle$ state is indicated by low readout magnitude and $|1\rangle$ by high readout magnitude. From fitting an exponentially decaying sinusoid to the plot (blue line) the $t(\pi/2)$ was determined to be 25ns and the $t(\pi)$ to be 70ns.

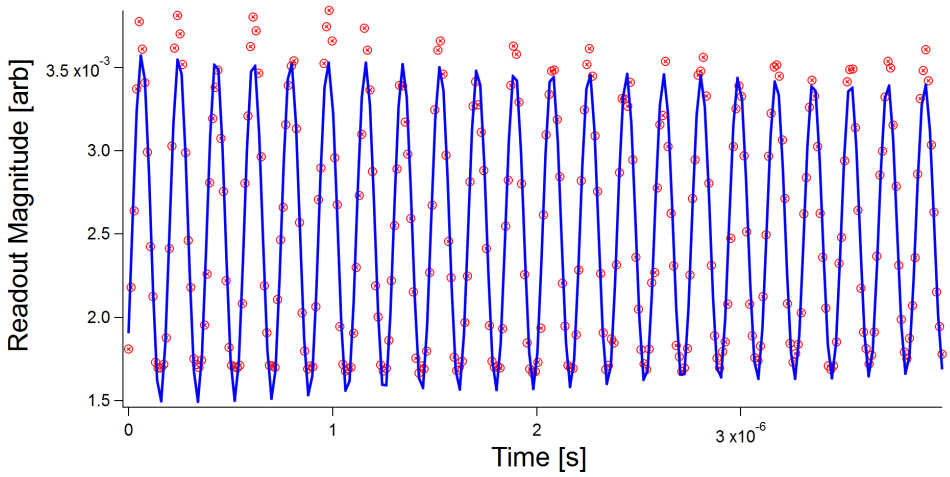

Figure 4.9: Rabi oscillations of the qubit using high power readout, obtaining $t(\pi/2) = 25$ns and $t(\pi) = 70$ns. The qubit was driven at -10dBm.

The Rabi frequency is linearly dependent on the the control pulse amplitude. Since the Rabi frequency determines $t(\pi)$ and $t(\pi/2)$, this power can be used to control the gate times of the system. The dependence of the π pulse length on the power of the control pulse is shown in Figure 4.10 and described by Equation 4.1. The pulse lengths should be chosen to be close to the decay times of the system to prevent the system from starting to decohere during the control pulse, but are limited in length by the equipment used

in experimentation. The lengths must also be longer than the shortest pulse that the equipment can produce to ensure that overshoot, rise/fall time have minimal effect on the pulse.

$$f = (-1.1385 \pm 0.448) \times 10^6 + (4.9885 \pm 0.238) \times 10^7 A \tag{4.1}$$

where f is time in Hz and A is the amplitude of the drive.

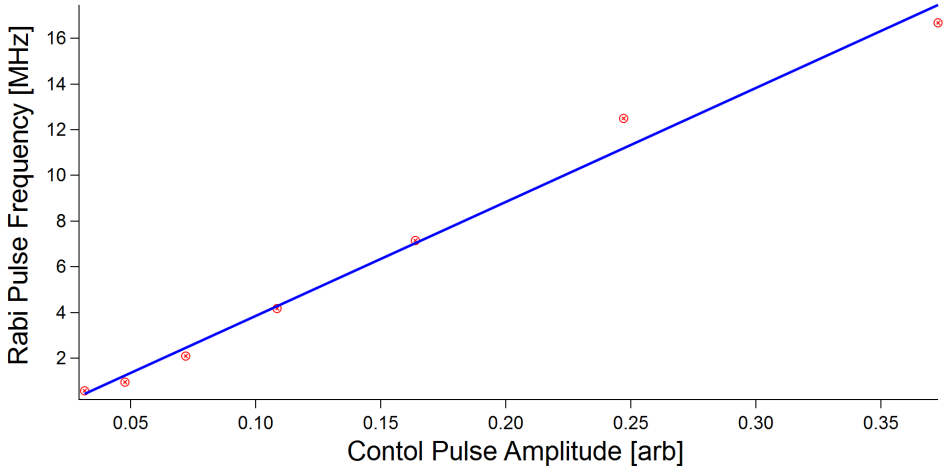

Figure 4.10: Power dependence of f_{Rabi} on the drive strength of the control pulse using high power readout. The pulse length is linearly dependent on the control pulse amplitude.

To limit the frequency domain of the control pulse, pulse shaping is used. Sharp corners, such as in square pulses, excite many superfluous frequencies, potentially exciting undesired transitions. Instead of a square pulse, a half Gaussian pulse shape is added to each side of the pulse with a half-width-half-max of 10ns. Due to this, the pulse is longer than what is reported in Figure 4.9; the 0ns pulse is actually a Gaussian pulse with a half-width-half-max of 10ns. To compensate for this in the high power readout, a histogram was used to determine a more accurate $t(\pi)$, Figure 4.11. This process was repeated with Ramsey oscillations to find the adjusted $t(\pi/2)$. The new $t(\pi)$ and $t(\pi/2)$ were determined to be 24ns and 68ns, respectively.

The Rabi oscillations were also used to determine the optimal readout pulse time for the high power readout. A histogram of the readout magnitude forms two, overlapping Gaussians, one pertaining to each state. Figure 4.12 shows the histograms for the qubit approximately in the superposition state $1/\sqrt{2}(|0\rangle + |1\rangle)$ for readout pulse lengths of 400, 600

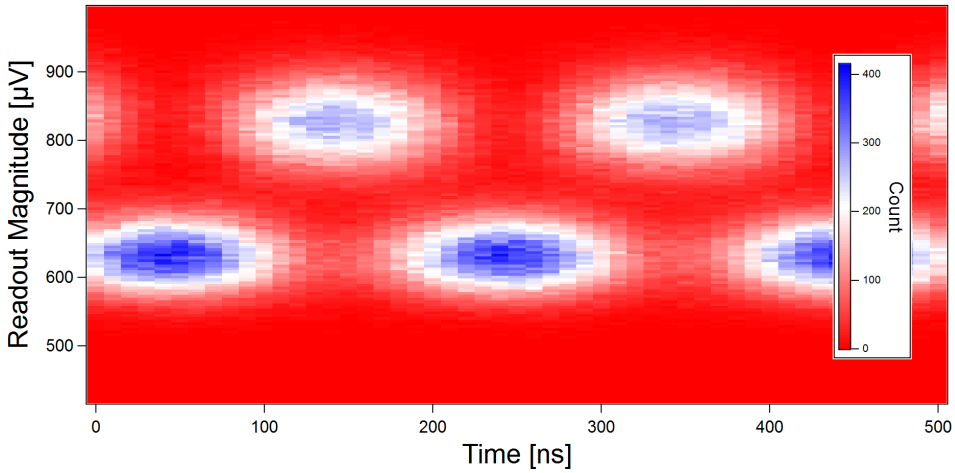

Figure 4.11: Histogram of the Rabi oscillations of the qubit with drive power −10dBm using the high power readout scheme. The adjusted π time was determined to be $t(\pi) = 68$ns. Repeating the process with Ramsey oscillations produced an adjusted $t(\pi/2)$ of 24ns.

and 800ns. The superposition state was achieved by applying a 35ns pulse at −10dBm. As the readout pulse decreases in length, the Gaussians move together and eventually overlap. The more the Gaussians overlap the states are harder to distinguish, providing a lower bound on how short the readout pulse can be.

Alternatively, a longer readout pulse provides time for the qubit to relax during readout. It can be seen in Figure 4.12**(a)** that there is more population in the $|1\rangle$ state (right Gaussian) than the $|0\rangle$ state (left Gaussian), with a 400ns readout pulse. As the readout pulse is lengthened to 800ns, the populations even out, as the qubit relaxes. A readout pulse is found such that there is maximal distinction between the two states without the qubit relaxing.

This method was not used for the low power readout because the Gaussians are too close together.

4.6.2 Relaxation Time, T_1

The two loss times, T_1 and T_2^*, as outlined in Section 2.2 can be measured through microwave pulse sequences. The first of these T_1, is measured through the decay of the qubit from the $|1\rangle$ state back to the $|0\rangle$ state. The pulse sequence uses a π pulse from a microwave source tuned to ω_{qb} to excite the qubit to the $|1\rangle$ state and then the state is read

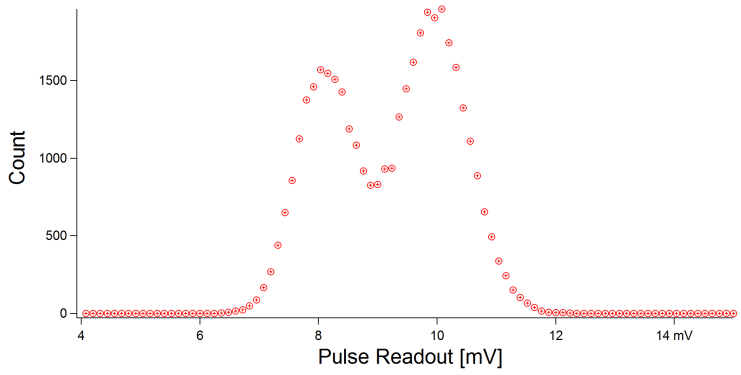

(a)

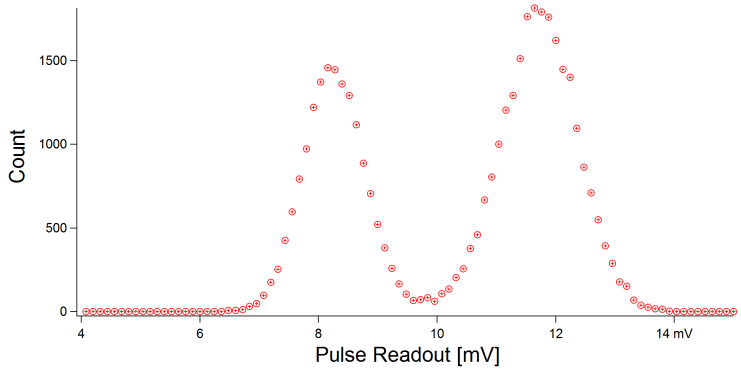

(b)

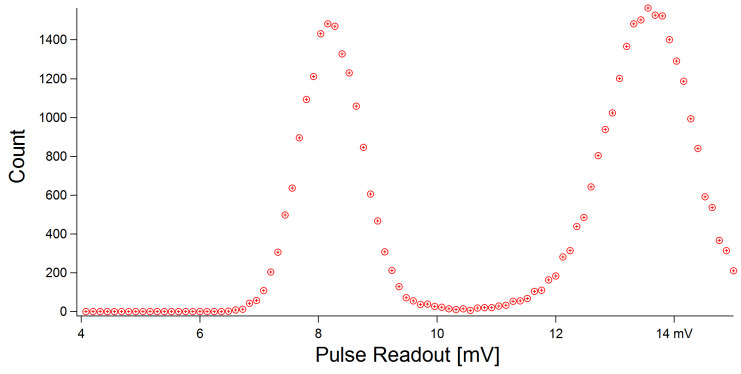

(c)

Figure 4.12: Histograms using 500 bins for high power readout times of **(a)** 400, **(b)** 600, and **(c)** 800ns after a 31ns qubit pulse at −10dBm. The Gaussians are too close together to provide optimal distinction between states in **(a)**, but relaxation can be seen in the qubit state for long readout times **(c)**. A pulse length of 650ns was used for the high power readout in future experiments.

out after waiting for time t, Figure 4.13. For each time t, the qubit is allowed to relax further, therefore plotting the population of $|1\rangle$ for increasing t forms an exponential decay. Fitting an exponential e^{-t/T_1} allows T_1 to be extracted from the data.

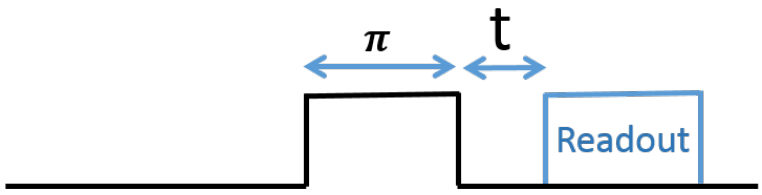

Figure 4.13: Microwave pulse sequence for T_1 measurements. The black line represents the amplitude of the control pulse. A π pulse is used to excite the qubit to the the $|1\rangle$ state. The time before readout is then varied to measure the decay.

The experimental data for the T_1 measurement is shown in Figure 4.14 (red marker). Using an exponential decay to fit the data (blue line), the T_1 time of the system was determined to be 17μs.

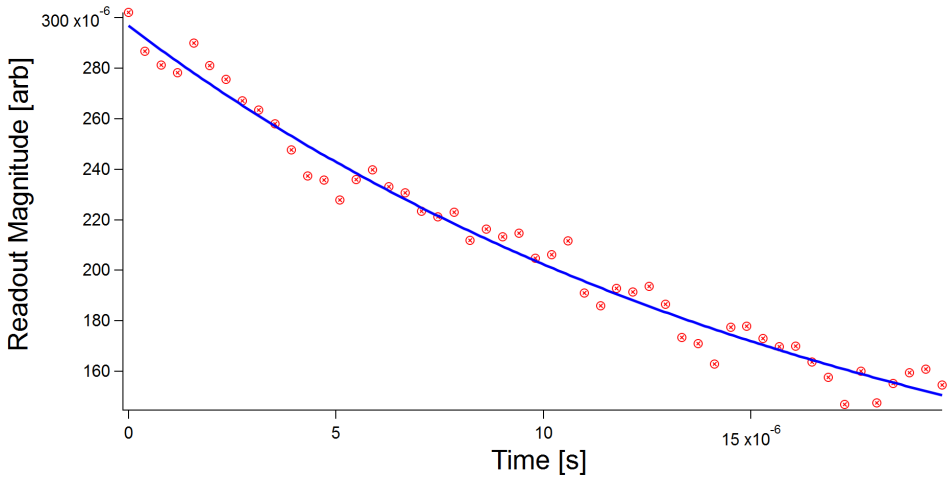

Figure 4.14: T_1 decay time for experimental data (red markers) using the high power readout scheme. Experiment used $t(\pi) = 68$ns and qubit drive power of -10dBm. Curve fit (blue line) indicates $T_1 = 17\mu$s.

4.6.3 Ramsey Oscillations and Dephasing Time

The second coherence time, T_2^*, is measured using two $\pi/2$ pulses [47]. The Ramsey sequence measures the decay of qubit coherence.

The pulse sequence uses two $\pi/2$ pulses. The first pulse brings the qubit from $|0\rangle$ on the Bloch sphere to $|+\rangle$ a rotation around the $|R\rangle$ axis (Figure 4.15). Then a time t is allowed to pass, allowing the qubit to decohere, the state moving around the plane formed by the $|R\rangle$ and $|+\rangle$ axes. The second π pulse is used to again rotate the state around the $|R\rangle$ axis and readout immediately follows. The more the qubit is able to decohere, the smaller the magnitude of the projection of the state onto $|1\rangle$ is, eventually ending in a 50% population in $|1\rangle$ when it reaches $|+\rangle$ or $|-\rangle$. The complete pulse sequence is shown in Figure 4.16.

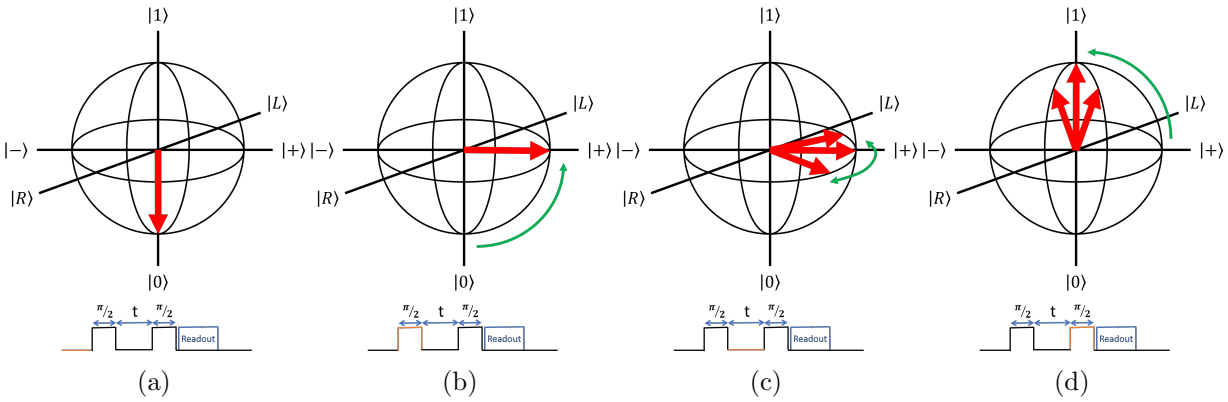

Figure 4.15: Bloch sphere representation of the qubit during a Ramsey measurement. **(a)** Before the Ramsey sequence begins the qubit is in state $|0\rangle$. **(b)** The first $\pi/2$ rotates the state by 90° to the state $|+\rangle$. **(c)** The time t allows the state to dephase. **(d)** The second $\pi/2$ pulse causes the qubit to rotate 90° around $|R\rangle$ again, and the state is read out.

If the control pulse is detuned from ω_{qb}, instead of a decay from $|0\rangle$ to $|1\rangle$, the state of the qubit oscillates with an exponentially decaying sinusoid, the Ramsey fringes. The decay constant of the exponential term of the fit extracts T_2^* from the data, but the frequency of oscillation is determined by the detuning of the control pulse. When the control pulse is detuned from ω_{qb}, it causes the state to process around the plane at the difference frequency between the control frequency and ω_{qb}, causing the oscillation between $|0\rangle$ and $|1\rangle$ at this difference frequency. This provides a more precise way to determine ω_{qb}.

Using 6 control pulses detuned ± 1, ± 2 and ± 3MHz from the expected qubit frequency were used to determined the qubit frequency. Using the average of the calculated qubit

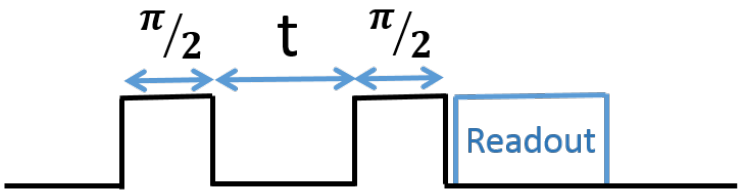

Figure 4.16: Microwave pulse sequence for Ramsey measurements. A $\pi/2$ control pulse (black line inticates control pulse amplitude) is followed by second a time t later. The state is then immediately readout. The sequence is repeated for increasing t.

frequencies, the qubit frequency was calculatd to be 6.1214GHz, Table 4.1.

Estimated Detuning (MHz)	**Control Frequency (GHz)**	**Ramsey Fringe Frequency (MHz)**	**Expected Qubit Frequncy (GHz)**
+3	6.1235	2.7834	6.1214
+2	6.1225	1.9351	6.1214
+1	6.1215	0.9859	6.1214
-1	6.1205	1.0364	6.1215
-2	6.1195	2.0987	6.1215
-3	6.1185	2.7352	6.1214
Average			6.1214

Table 4.1: Ramsey fringe frequencies found using high power readout for 6 frequencies used to determine qubit frequency. The qubit frequency is 6.1214GHz

The experimental data is shown in Figure 4.17 (red markers). The blue line is the exponential decay fit to the data. The fit indicates $T_2^* = 16\mu$s.

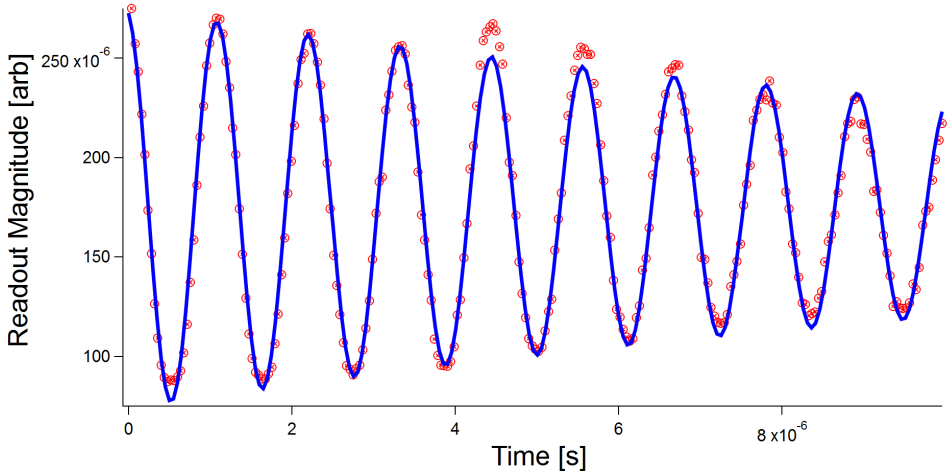

Figure 4.17: Experimental Ramsey data (red markers) for a drive frequency of 6.1225GHz at $-10d$dBm using $t(\pi/2) = 24$ns. The expected oscillation frequency is 1MHz. Curve fit (blue line) indicates $T_2^* = 16\mu$s and an oscillation frequency of 8.9295 ± 0.000667MHz.

4.6.4 Spin Echo

The spin echo measurement uses three control pulses tuned to ω_{qb} to eliminate pure dephasing of the system, obtaining T_2 [40][23]; specifically, for a transmon, it removes the low frequency noise. The first pulse is a $\pi/2$ pulse which brings the qubit into the superposition $|+\rangle = 1/\sqrt{2}\,(|0\rangle + |1\rangle)$. The first time t allows the qubit to dephase, before a π pulse is used to flip the state along the $|+\rangle\,/|-\rangle$ axis of the Bloch sphere. This allows the dephasing to bring the qubit back to the $|-\rangle$ state during the second time t before using the last $\pi/2$ pulse to bring the qubit into the $|1\rangle$ state. The entire pulse sequence is outlined in Figure 4.18 and the corresponding states are shown in Figure 4.19.

Varying the time t causes the qubit to oscillate between $|0\rangle$ and $|1\rangle$ with exponentially decaying amplitude. Fitting the data from higher power readout, shown in Figure 4.20 (red markers), with an exponentially decaying sinusoid (blue line) extracts the $T_2 = 35\mu$s. As $T2 \simeq 2T_1$, this is very close to the theoretical limit $\Gamma_2 \simeq \Gamma 1/2$, indicating that the Ramsey sequence nearly eliminates all of the pure dephaing.

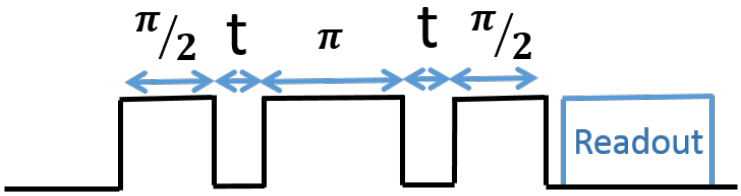

Figure 4.18: The pulse sequence for a spin echo experiment, with the black line indicating the amplitude of the control pulse. There are two $\pi/2$ separated by a single π pulse. The time between the $\pi/2$ and π pulses is swept and readout occurs after the second $\pi/2$ pulse.

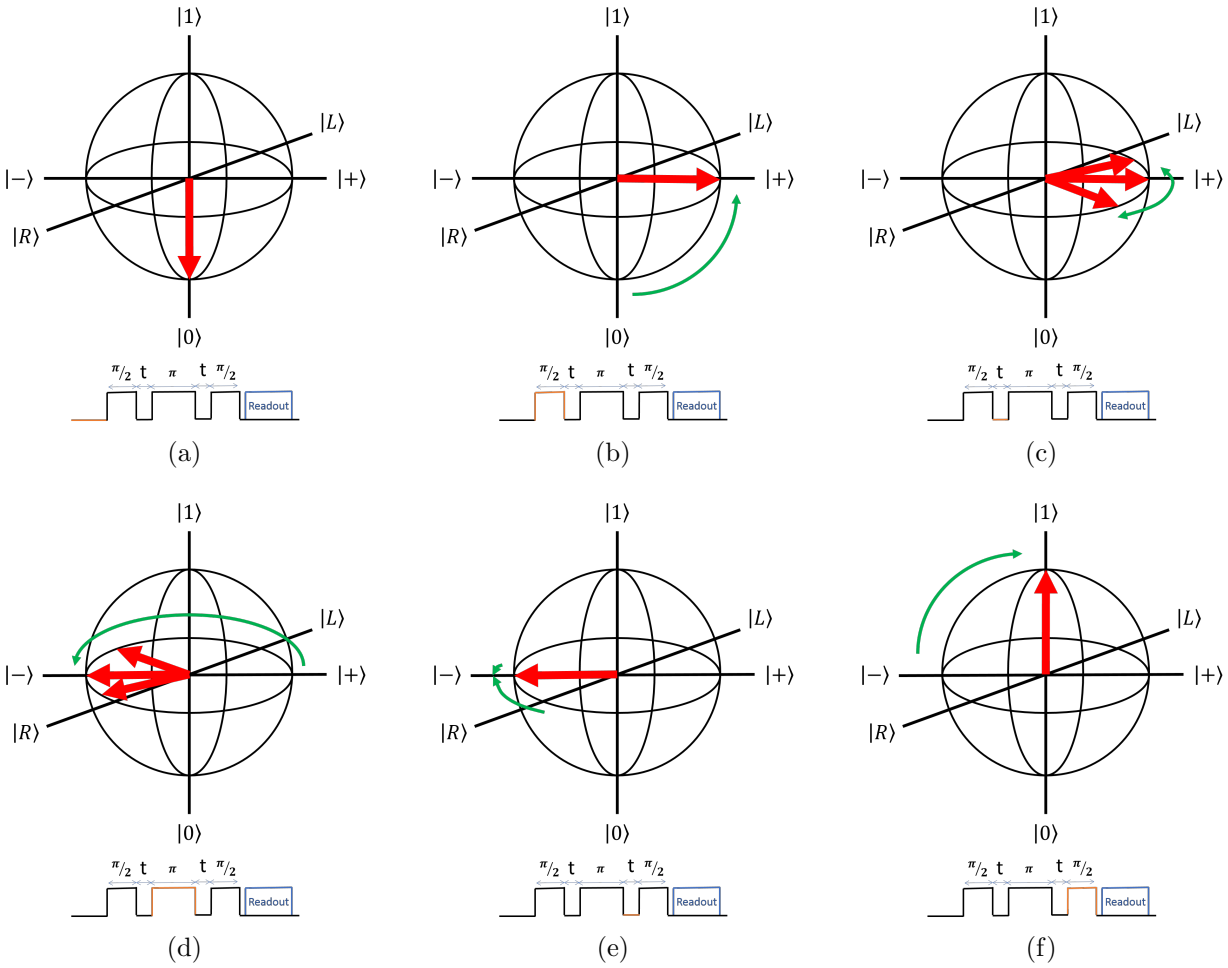

Figure 4.19: Bloch sphere representation of the qubit during a spin echo sequence. **(a)** Before the spin echo sequence begins the qubit is in state $|0\rangle$. **(b)** The first $\pi/2$ rotates the state by 90° to the state $|+\rangle$. **(c)** The first time t allows the state to dephase. **(d)** The pi pulse rotates the state by 180° and **(e)** the qubit state continues to dephase in the same direction causing it to rephse into the $|-\rangle$ state. **(f)** The final $\pi/2$ pulse causes the qubit to rotate to the $|1\rangle$ state.

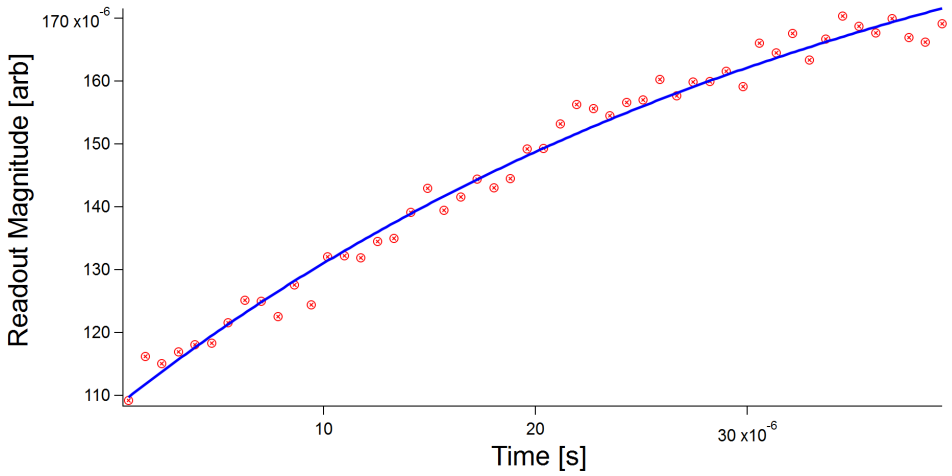

Figure 4.20: Spin echo shows significant improvement in dephasing time. Fitting the data collected with high power readout (red markers), obtained with a -10dBm control drive, with an exponential curve (blue line) gives $T_2 = 35\mu$s, which is close to the theoretical limit $\Gamma_2 \simeq {}^{\Gamma 1}/_{2}$.

4.7 Lambda System

Placing a qubit in a cavity causes a dispersive shift of χ. Interactions between the cavity and qubit cause the harmonic levels of the cavity to shift from $\omega_{cav} - \chi$ (blue states of Figure 4.21) to $\omega_{cav} + \chi$ (yellow states of Figure 4.21) as in Figure 4.3. Looking at this system as a whole, there is a double ladder system, Figure 4.21.

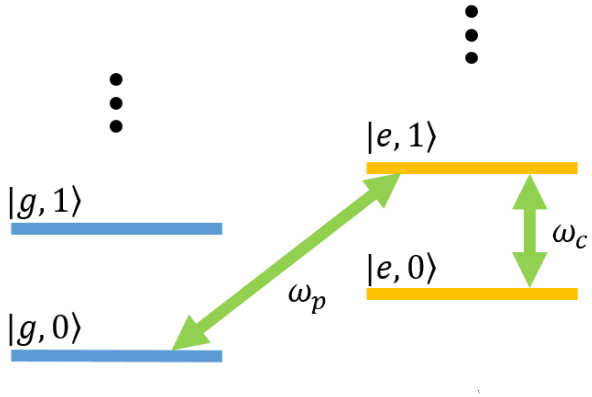

Figure 4.21: Arrangement of energy levels in the cavity-qubit system.

Decay between levels in a ladder is dominated by the decay rate of the cavity (κ), while decay from one ladder to another is dominated by the decay rate of the qubit (Γ). If the decay rate of the qubit is significantly smaller than the decay rate of the cavity the decay between rungs happens faster than from the qubit excited state ladder to the qubit ground state; decay down the qubit excited state ladder traps the system in the $|e,0\rangle$ state, leaving the only decay channel to be through the relatively slow qubit relaxation to $|g,0\rangle$. Thus, the state $|e,0\rangle$ acts as a metastable state and the states $|g,0\rangle$, $|e,1\rangle$ and $|e,0\rangle$ can be used as $|g\rangle$, $|e\rangle$, and $|f\rangle$, forming a lambda system (Figure 4.22).

The system used in this experiment has a cavity decay rate of $\kappa = 0.25$MHz, while the decay rate of the qubit is $\Gamma = 62.5$kHz. Although κ is not large enough for $\kappa \gg \Gamma$, is is still greater than Γ, and the system can still be used as a lambda system.

Using a transmon requires the $|g\rangle \leftrightarrow |f\rangle$ to be a two-photon transition. The frequency of this transition is $(\omega_{cav} - \chi + \omega_{qb})/2 \times 2\pi = 6.5991$GHz. The $|e\rangle \leftrightarrow |f\rangle$ transition is the cavity frequency when the qubit is in the excited state, $\omega_{cav}/2\pi - \chi/2\pi = 7.0779$GHz.

Two drives are used to control the system. The first, the probe, ω_p is used to drive the $|g\rangle \leftrightarrow |f\rangle$ transition and is detuned from this transition frequency by Δ_p. The other

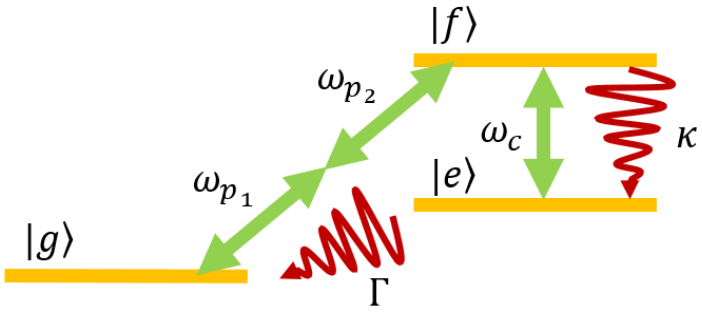

Figure 4.22: Arrangement of energy levels in the lambda system. The third decay of $|f\rangle \rightarrow |g\rangle$ is not shown as it is not used in experiment.

transition, $|e\rangle \leftrightarrow |f\rangle$, is controlled by the second, coupler drive (ω_c) with detuning Δ_c. The two-photon transition allows the two photons to be detuned from the two-photon transition frequency and driven by two separate probe microwave drives, ω_{p_1} and ω_{p_2}. It is then also possible to drive these at different drive strenghths. Here, the higher powered drive strength will be denoted Ω_{p_1} (corresponding to ω_{p_1}) and the lower power Ω_{p_2} (corresponding to ω_{p_2}). If only a single probe drive is used it is denoted ω_p.

4.7.1 Dipole Induced Transparency

To demonstrate the interference effects of the system and DIT [58], both ω_c and ω_p are used. Spectroscopy was completed sweeping ω_c near the $|e\rangle \leftrightarrow |f\rangle$ transition frequency using a network analyzer with $\Omega_c = -60$dBm. ω_p is swept near the expected two-photon transition frequency ($^{(\omega_{cav} - \chi + \omega_{qb})}/_2 = 6.5991$GHz) using a QS at $\Omega_c = -4$dBm.

Although DIT refers to an induced transparency, this was named for reflection experiments. For these experiments instead of the increase in transmitted signal magnitude, the reflected signal is absorbed when a frequency is on resonance. Therefore, the splitting in the absorbence line expected for DIT (Section 2.5.2) corresponds to the splitting, or induced opaquency, in the transmission in this experiment.

Figure 4.23**(a)** shows the transmitted magnitude of ω_p. The transmission line at 7.08GHz corresponds $\omega_{cav} + \chi$: the cavity resonance with the qubit in the ground state.

The transmission line at ~ 7.0779GHz is the transmission of the coupler when tuned near the $|e\rangle \leftrightarrow |f\rangle$ transition. This transmission line only occurs when ω_p is tuned near then $|g\rangle \leftrightarrow |f\rangle$ transmission. This is expected, as, for ω_c to resonate, there must be some population in $|e\rangle$ which can be achieved through the excitation of $|g\rangle \rightarrow |f\rangle$ and decay $|f\rangle \rightarrow |e\rangle$.

Looking closer at transmission line of ω_p for tuned ω_c and ω_p (Figure 4.23**(b)**), a splitting in the transmission line is seen. This occurs when ω_c and ω_p are tuned such that the quantum transition amplitudes interfere, producing a dark state in $|e\rangle$. Without any population in $|e\rangle$, the coupler is unable to excite the $|e\rangle \leftrightarrow |f\rangle$ transition and there is no amplification of transmitted magnitude of ω_c.

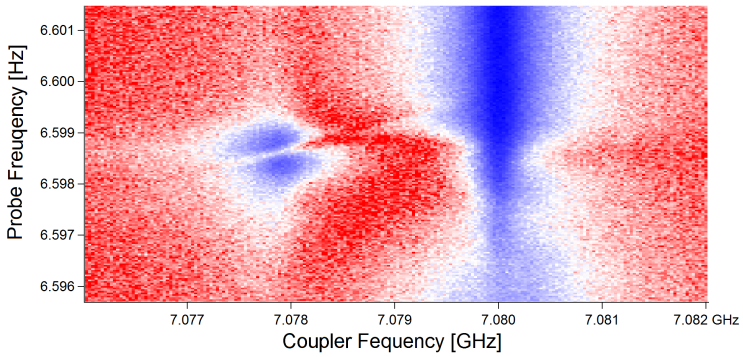

(a)

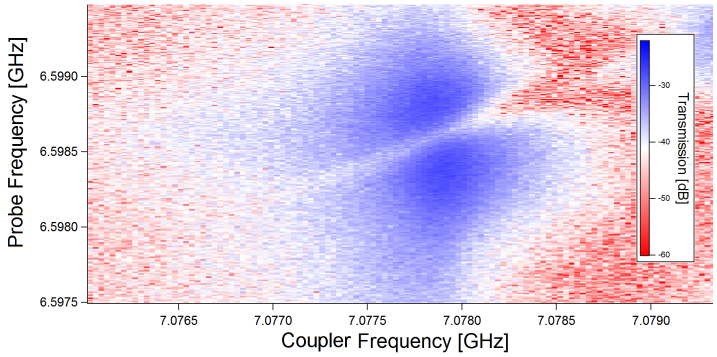

(b)

Figure 4.23: Spectroscopy of the two-photon drive at a cavity coupler of -60dBm and qubit coupler of -4dBm. **(a)** The right transmission line is $\omega_{cav} + \chi$ and the right is $\omega_{cav} - \chi = \omega_p$ when $\Delta_p = 0$ **(b)** Zoomed in look at transmission of ω_p. The suppression of the excited state is a signature of DIT

The centre of the splitting of the transmission line moves linearly with both ω_c and ω_p (Figure 4.24). The slope of this shift is $0.45 \pm 0.00259^{\mathrm{GHz}}/_{\mathrm{GHz}}$. Since $\Delta_p = 2\omega_p - \omega_{qb} - \omega_{cav} - \chi$ it is expected that the slope of this line $0.5^{\mathrm{GHz}}/_{\mathrm{GHz}}$, half of the predicted slope of $1^{\mathrm{GHz}}/_{\mathrm{GHz}}$. Therefore, it is in good agreement for theoretical predictions from the single probe drive model (Section 3.1).

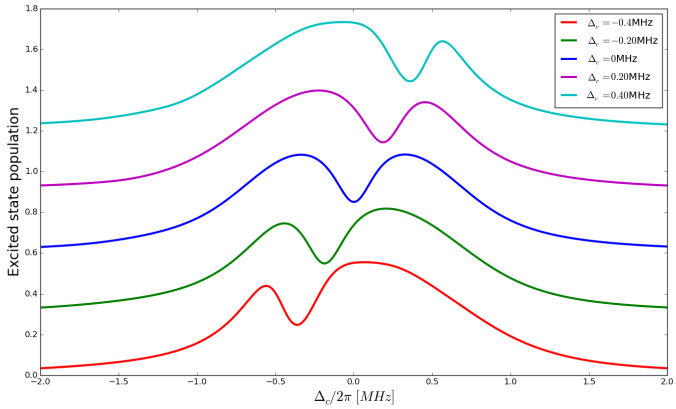

(a)

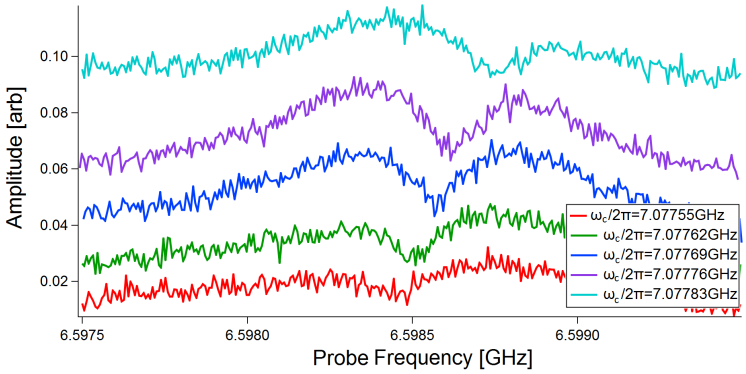

(b)

Figure 4.24: Linecuts of DIT. **(a)** Theoretical predictions. As ω_c increases, the location of the system being trapped in $|g\rangle$ (no steady state population in $|e\rangle$) shifts with ω_c. **(b)** Experimental data: at ω_c= 7.07755GHz(red), 7.07762GHz(yellow), 7.07769GHz(green), 7.07776GHz(blue), and 7.07783GHz(purple). The supression of the transmission of ω_p moves linearly with ω_c. The location of the supression also moves with ω_c detuning, indicating that the supression is caused by the system being trapped in $|g\rangle$.

4.7.2 Lifetime of the Metastable State

The lifetime of the metastable state, $|e\rangle$, is used to calculate the gain of the system. The gain is defined as the number of photons gained or lost in the controlled signal, divided by the number of photons in the pulse of ω_{p_2} (Equation 2.39). By probing the lifetime of the metastable state the number of photons added or removed to the control pulse can be calculated.

As shown in Figure 4.25, two frequencies can be controlled by the microwave transistor, ($\omega_{control} = \omega_{cav} \pm \chi$). These correspond to the cavity resonant frequency when the qubit is in the ground ($+\chi$) and excited ($-\chi$). Since there are two frequencies that can be used as $\omega_{control}$, the lifetime of the excited state is investigated for both frequencies.

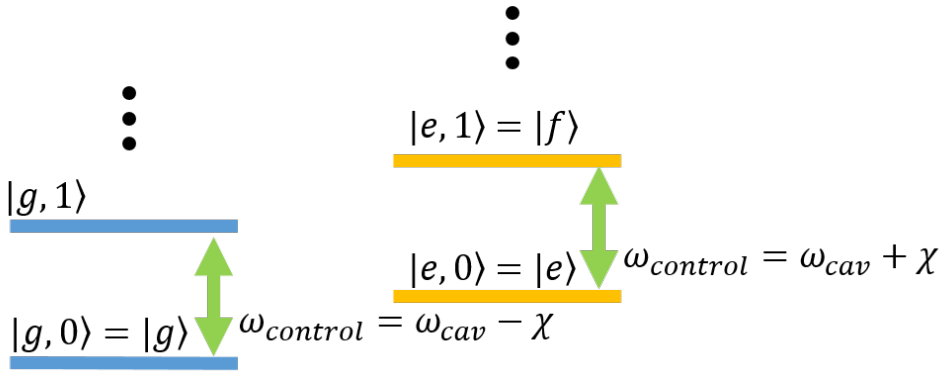

Figure 4.25: Two frequencies can be controlled by the microwave transistor ($\omega_{control} = \omega_{cav} \pm \chi$). The transmission of these frequencies is used to investigate the lifetime of the metastable state and determine the gain of the system.

The lifetime of $|e\rangle$ was investigated by pulsing ω_{p_2} with $\Delta_p = 0$ for 3μs at 5dBm using the SigGen and then monitoring the transmission of a continuous-wave microwave drive at -60dBm over a $100 - 200\mu$s time interval. The 3μs pulse was determined to be long enough to move the state to $|e\rangle$ through a T_1-like experiment. The pulse started at 40μs into each time interval. This was then repeated thousands of times and the measurement averaged for each data point.

The detuning of ω_{p_1} and ω_{p_2} were held constant for each controlled frequency. ω_{p_1} was driven by a QS with $\omega_{p_1} = 6.60966666$GHz, and ω_{p_2} driven by the network analyzer with $\omega_{p_2} = 6.588733333$GHz. The controlled frequency was driven by a second QS.

To calculate the number of photons that reached the system, the power of the signal at the cavity was determined using the attenuation of the cables and room temperature and cold attenuaters. This was then adjusted using the data from Appendix C for the attenuation of the splitters as well as the power reported by the source including the power of the noise frequencies, not only the centre frequency. This power was then integrated over the time of the pulse, to find the total energy, and then divided by the energy of the photon of interest. This process can be described by Equation 4.2.

$$\text{number of photons} = \int_0^t \frac{P(t)}{\hbar\omega_{p_2}} \tag{4.2}$$

where P is time dependent function of the power of the pulse leaving the cavity and t is pulse length. This equation can also be used to calculate the number of photons in the ω_{p_2} pulse, integrating the power at the cavity.

In Figure 4.26, the $\omega_{control}$= 7.0799GHz was driven at 10dBm with 60dB of room temperature attenuation. ω_{p_1} was driven at 12.3dBm, while ω_{p_2} was driven at 10dBm with 60dB of room temperature attenuation. Using a continuous-wave microwave drive at $\omega_{control}$ = 7.0799GHz to monitor the $|e\rangle \leftrightarrow |f\rangle$ transition, the decay time of $|e\rangle$ is $\sim 3\mu$s, Figure 4.26, which is on the order of κ (4μs). This occurs because the second drive pushes the system out of $|e\rangle$ to $|f\rangle$ and allows it to decay from $|f\rangle$ to $|g\rangle$, directly. κ dominates this decay, and is much shorter than the expected lifetime of the metastable state.

Using Equation 4.2 to calculate the number of photons, the transmission of the control pulsed increased by 9 billion photons. ω_{p_2} corresponds to a pulse of 109 thousand photons. Then using Equation 2.39 the gain can be calculated to be $\sim$ 83 thousand $^{\text{photons}}/_{\text{photon}}$.

If instead, a continuous-wave drive to monitor the transmission of $\omega_{control} = \omega_{cav} + \chi$ = 7.0800GHz is used, a decay rate of the metastable state much closer Γ is seen (Figure 4.27). Although the lost of some excitations of $|g\rangle \leftrightarrow |f\rangle$ by driving the system into a state not included in the lambda system (into the $|g, 1\rangle$ state) is expected, this better reflects the expected decay time of the metastable state. The lifetime of the state is $\sim 27\mu$s, which is on the order of T_2 (35μs).

Figure 4.27 was completed using a controlled frequency of 7.0800GHz at 10dBm with -20dB attenuation. ω_{p_2} was driven at -30dBm while ω_{p_1} was driven at 9.1dBm with 20dB attenuation. There were 11 million photons calculated to be in the ω_{p_2} pulse while 58 million photons shifted in the controlled signal. This gives a gain of 5 $^{\text{photons}}/_{\text{photon}}$.

This system can work as a transistor for two $\omega_{control}$ frequencies. The system can be loaded into $|e\rangle$ by turning on ω_{p_2} for sufficiently long. This then will then either increase or

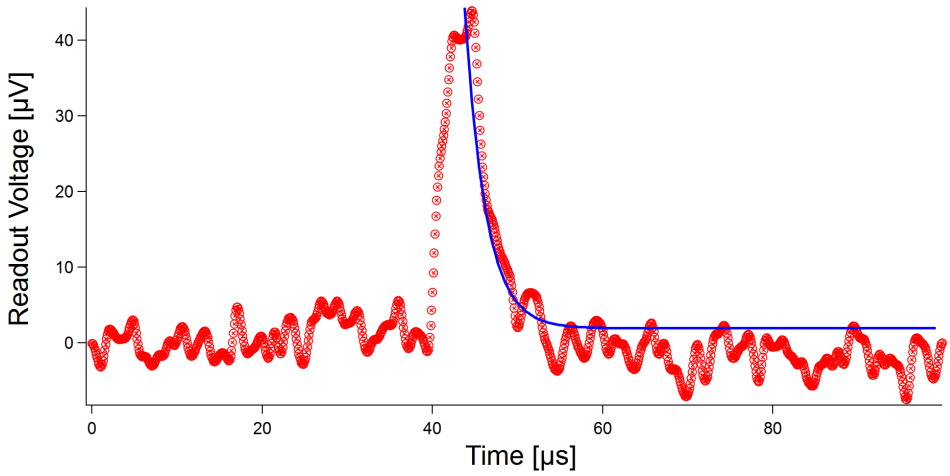

Figure 4.26: Transmission of the continuous $\omega_{control} = \omega_{cav} - \chi = 7.0799$GHz drive at 10dBm with 60dB of room temperature attenuation. ω_{p_1} was also driven continuously at 12.3dBm. ω_{p_2} was pulsed for 3μs at 40μs at 10dBm with 60dB of attenuation. This causes system to transition to $|e\rangle$, which, in turn, causes the amplification of $\omega_{cav} - \chi$. The decay time of $|e\rangle$ ($\sim 3\mu$s), found by fitting an exponential to the decay of the amplification, is on the order of the κ, which dominates the $|f\rangle \rightarrow |g\rangle$ decay. This indicates the $|e\rangle \leftrightarrow |f\rangle$ drive pushes the qubit back into the $|f\rangle$ state. The gain seen is 83 thousand $^{\text{photons}}/_{\text{photon}}$.

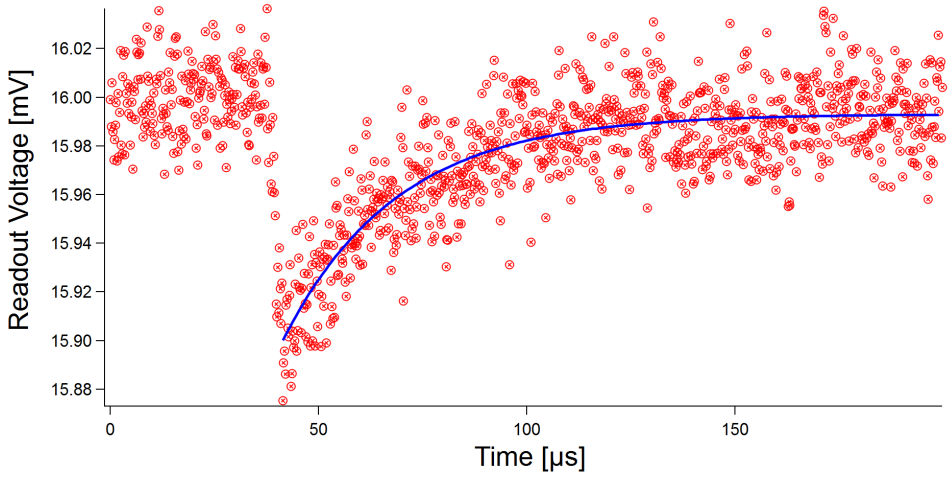

Figure 4.27: Transmission a continuous wave drive at $\omega_{control} = \omega_{cav} + \chi = 7.0800$GHz and -60dBm. ω_{p_1} was driven at 9.1dBm with 20dB of attenuation while ω_{p_2} was driven at -30dBm. When ω_p is pulsed for 3μs at 40μs, the system transitions to $|e\rangle$, causing a supression in the transmission of the decay rate of $\omega_{cav} + \chi$. Fitting an exponential to the decay of the suppression the lifetime of $|e\rangle$ is determined to be $\sim 27\mu$s. This is on the order of Γ, and indicates the system is decaying through the $|e\rangle \rightarrow |g\rangle$ channel, as desired. The gain was 5 $^{\text{photons}}/_{\text{photon}}$.

decrease the transmitted or reflected magnitude of a continuous microwave drive at one of the two frequencies. The first is the transition frequency of $|e\rangle \leftrightarrow |f\rangle$, $\omega_{cav} - \chi$. It increases (decreases) in transmitted (reflected) power when the ω_{p_2} is turned on loading into $|e\rangle$, as the frequency can resonate with the $|e\rangle \leftrightarrow |f\rangle$ transition. $|e\rangle$ then decays quickly when ω_{p_2} is turned off; the decay is on the order of κ. This is because when the state is loaded into state $|e\rangle$ and the $|e\rangle \leftrightarrow |f\rangle$ transition is excited, the state is allowed to decay through the channel $|f\rangle \rightarrow |g\rangle$ which is dominated by κ.

The second frequency is $\omega_{cav} + \chi$, the cavity frequency when the qubit is in the ground state. Once the system is loaded into $|e\rangle$, a continuous drive of this frequency will not change the state of the system. Since the system is in $|e\rangle$ the qubit is in th excitd state and the cavity frequency corresponding to the qubit in the ground stat can no longer resonate. This will cause $\omega_{cav} + \chi$ to decrease (increase) in transmitted (reflected) power when ω_p is turned on. The decay of this suppression in transmission decays slower when ω_p is turned off; decaying on the order of Γ.

Although the $\omega_{cav} - \chi$ has a shorter decay time of the metastable state, here, it had an overall better gain.

4.7.3 Detuning Two Probe Drives

The single photon transition from the ground to second excited state of the lambda system is forbidden with a transmon [34]. Instead, a two photon drive is required. This can either be done through a single ω_p at the two-photon transition frequency or two drives, ω_{p_1} and ω_{p_2}, which average frequency is the two-photon transition frequency.Figure 4.28.

To confirm that the average of ω_{p_1} and ω_{p_2} has to be the two-photon transition frequency, two microwave drives were used. Both drives were set to continuos-wave. Sweeping Δ_{p_1} and Δ_{p_2}, the state of the qubit was monitored to determine if the system was in $|e\rangle$. For each new Δ_{p_1} and Δ_{p_2} pairing, the system was allowed to normalize for 30μs and then the state of the qubit was readout using a third microwave drive and the high-power readout scheme described in Section 4.5 (see Appendix B for equipment setup). The transmitted magnitude of the readout pulse was then integrated to calculate the readout magnitude.

The readout the network analyzer at $\Omega_{p_1} = -5$dBm as ω_{p_1} and a QS as ω_{p_2} at $\Omega_{p_2} = -10$dBm, the readout magnitude is plotted for various Δ_{p_1} and Δ_{p_2} in Figure 4.28. Blue areas show the qubit in the excited state. The vertical line $\omega_{p_1} = 6.5992 \pm 0.00000798$GHz indicates that ω_{p_1} is driven strongly enough to drive the two-photon transition directly. ω_{p_2} is not driven as strongly and excited state at the two-photon transition frequency is very faint.

The excited state shows a linear trend with a slope of $-1.1 \pm 0.00136^{\text{Hz}}/_{\text{Hz}}$. This is in good agreement with the predicted slope of $-1 \pm 0.00000027^{\text{Hz}}/_{\text{Hz}}$ (Figure 3.9) by the two probe drive model in Section 3.2. The average of the frequencies of the probe drives two-photon transition. The experimental results are shifted from the theoretical prediction (black line, Figure 4.28) because of an ac-Stark shift due to strong driving of the system [53].

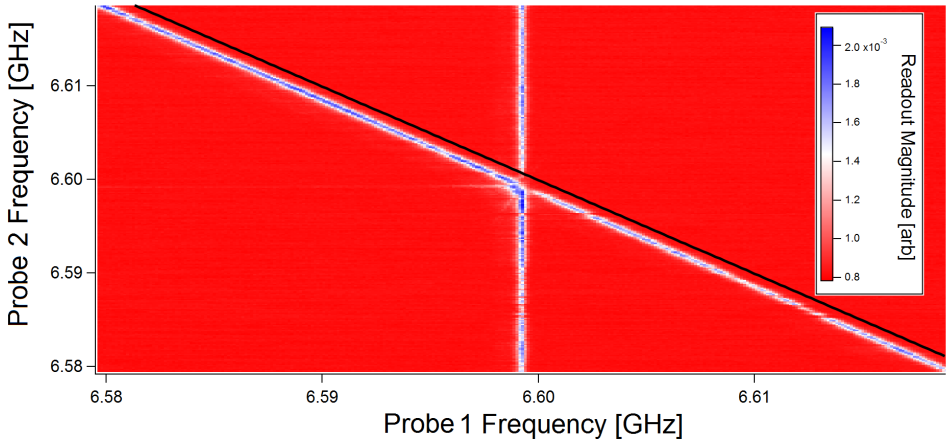

Figure 4.28: Qubit excited state population for a detuned two photon drive using a high power drive of $\Omega_{c1} = -5$dBm and low power drive $\Omega_{c2} = -10$dBm. The probe drive is strong enough to excite the two photon transition on its own. The black line is the predicted theoretical line.

A linecut at $\omega_{p_2} = 6.6021$GHz from Figure 4.28 is shown in Figure 4.29. Two frequencies ($\omega_{p_1} = 6.5992 \pm 0.00000798$GHz and $\omega_{p_1} = 6.5961$GHz invoke an excited state in the qubit. $\omega_{p_1} = 6.5992 \pm 0.00000798$GHz corresponds to the two-photon transition frequency, indicating that a drive strength of -5dBm is strong enough to drive the transition $|g\rangle \leftrightarrow |e\rangle$ with a single ω_p. The other $\omega_{p_1} = 6.5961$GHz is the detuned ω_{p_1} required to have an average ω_p equal to the two-photon transition frequency.

Fitting the linewidth of the excitation with linewidths predicted by the two probe drive model in Section 3.2, Figure 4.29, it was determined that the high power drive corresponds to a Rabi drive frequency of 12.6kHz in the theoretical model, and the low power drive corresponded to a Rabi drive frequency 8.4kHz.

Next, the power dependence of the detuning was investigated. The same experimental technique was used as for the detuning, but ω_{p_1} and Ω_{p_1} were held constant and the frequency and drive amplitude of ω_{p_2} were swept. To sweep the microwave source linearly in drive frequency, the amplitude was converted to power, in dBm as $-20 \log(\text{amplitude})$.

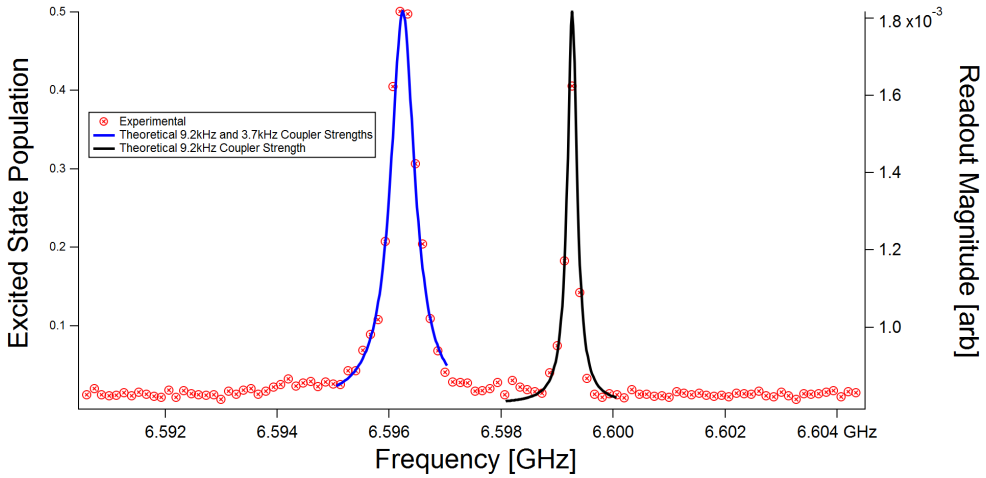

Figure 4.29: Linecut of excited state population at $\omega_{p_2} = 6.6021$GHz. The peak at $\omega_{p_1} = 6.5992 \pm 7.98e-6$ corresponds to a single ω_c. The peak at $\omega_{p_1} = 6.5961$GHz is the detuned ω_{p_1} that is required for the $|g\rangle \leftrightarrow |f\rangle$ transition with $\omega_{p_2} = 6.6021$GHz. Theoretical fit of the linewidths are from the two probe drive theoretical model. It was determined that -5dBm drive corresponds to a Rabi drive frequency of $\Omega_{c1} = 12.6$kHz in the two probe drive theoretical model and -10dBm to $\Omega_{c2} = 8.4$kHz.

For combination of ω_{p_2} and Ω_{p_2}, the population of $|e\rangle$ is plotted as the readout magnitude (Figure 4.30).

Figure 4.30 shows the readout magnitude for each combination of ω_{p_2} and Ω_{p_2} for $\omega_{p_1}/2\pi = 6.6144$GHz and $\Omega_{p_1} = -10$dBm. It can be seen that ω_{p_2} creating a population in $|e\rangle$ (shown in blue and white), shifts down in frequncy as Ω_{p_2} increases and the linewidth of this transition broadens. This can be attributed to an ac-Stark-like shift due to strong driving of the system. Above $\Omega_{p_2} = 2$, the response broadens, and the excitaiton is washed out.

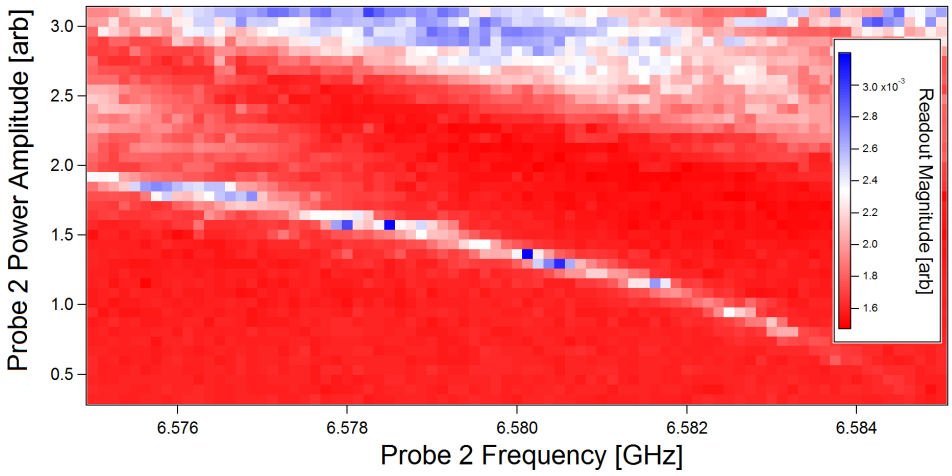

Figure 4.30: Power dependent detuning of the two-photon transition. The frequency and power of the high power probe is held constant at 6.6144GHz and 10dBm, while both the power and frequency of the low power probe is swept ($6.58 - 6.59$GHz and power linearly in amplitude from $0.32 - 3.1$).

For $\Omega_{p_2} = 0.32 - 3$ in Figure 4.30, a Lorentzian lineshape was fit to the spectrum. The ω_{p_2} corresponding to the peak of this lineshape is plotted for each Ω_{p_2} amplitude in Figure 4.31 (red markers). From this it can be seen that a quadratic fit (blue line) describes the shift in frequency for increasing Ω_{p_2} amplitude. The equation of the quadratic fit is

$$f = 6.584 \pm 0.00018 - (6.7023 \pm 2.5) \times 10^{-4} P - (7.8877 \pm 0.743) \times 10^{-4} P^2 \qquad (4.3)$$

where P is the amplitude of the low power probe.

To ensure that the detuning is still linear for higher Ω_{p_1} and Ω_{p_2}, the combinations, the detuning experiment was repeated for $\Omega_{p_1} = \Omega_{p_2} = 0$dBm and $\Omega_{p_1} = 0$dBm and

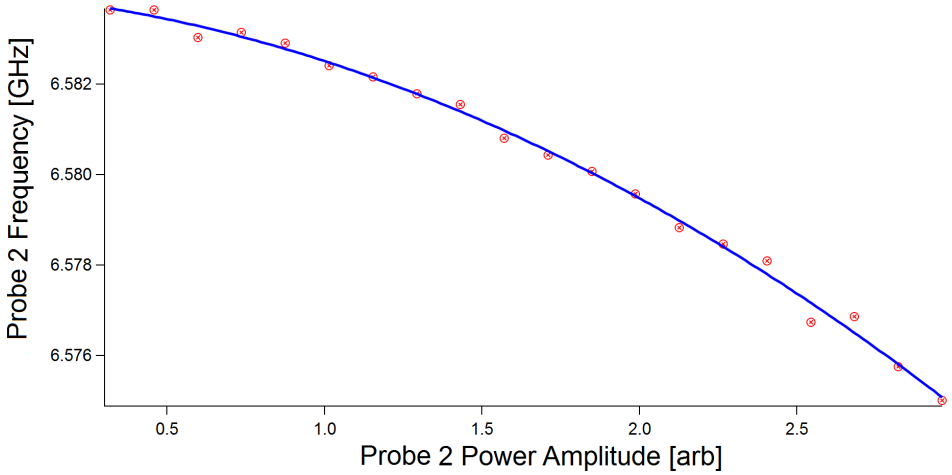

Figure 4.31: Power dependent detuning of the two photon transition. The power changes polynomially with the amplitude of the power. $f = 6.584 \pm 0.00018 - (6.7023 \pm 2.5) \times 10^{-4}P - (7.8877 \pm 0.743) \times 10^{-4}P^2$, where P is the power of the high power probe drive.

$\Omega_{p_2} = -10$dBm (Figure 4.32). In both Figure 4.32**(a)** and **(b)**, the detuning remains linear. It can be concluded that the detuning remains linear as long as Ω_{p_1} and Ω_{p_2} are held constant.

4.7.4 Towards Single Photon Drive

For implementation in a single photon transistor or as a single photon detector it was predicted that with sufficiently high Ω_{p_1}, ω_{p_2} could be reduced to a single photon. Initial experiments tried to repeat the experiment in Section 4.7.2 with decreasing Ω_{p_2} and monitoring the transmission of $\omega_{cav} + \chi = 7.08$GHz, but due to noise of the network analyzer and amplification, no change in the transmission of the signal was seen.

Instead, the goal of this experiment is to show that for each Ω_{p_2} and ω_{p_2}, there is a ω_{p_1} that produces population in $|e\rangle$ and $|f\rangle$. This can be done by showing that the qubit is in the excited state. If the qubit is in the excited state, then ω_{p_1} and ω_{p_2} have successfully excited the $|g\rangle \leftrightarrow |f\rangle$ transition and the system has been loaded into $|e\rangle$. Since this experiment was conducted using the state of the qubit rather than $\omega_{control}$, the gain of the system was not calculated.

Two QS are used for ω_{p_1} and ω_{p_2}. ω_{p_1} is used as a continuous-wave drive, while ω_{p_2} is pulsed to fix the number of control photons at ω_{p_2}. Ω_{p_2}, ω_{p_2}, and ω_{p_1} were held constant

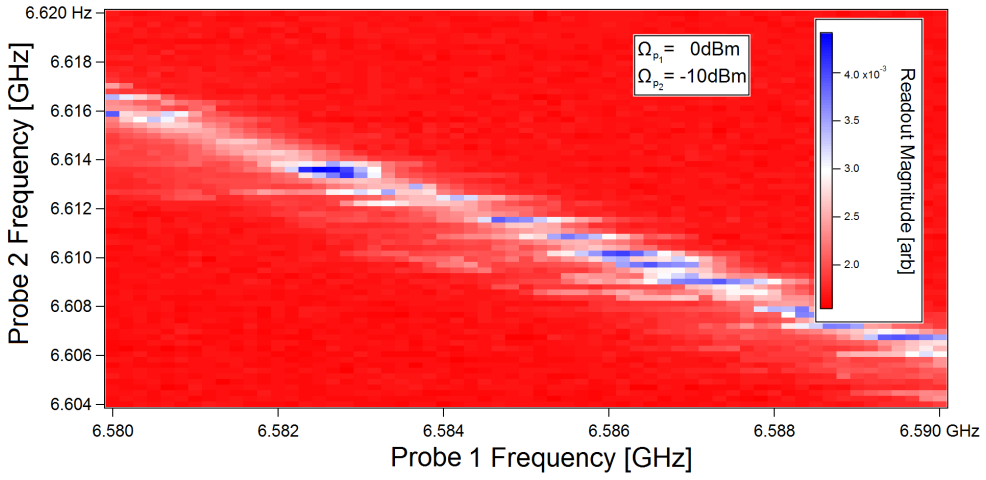

(a)

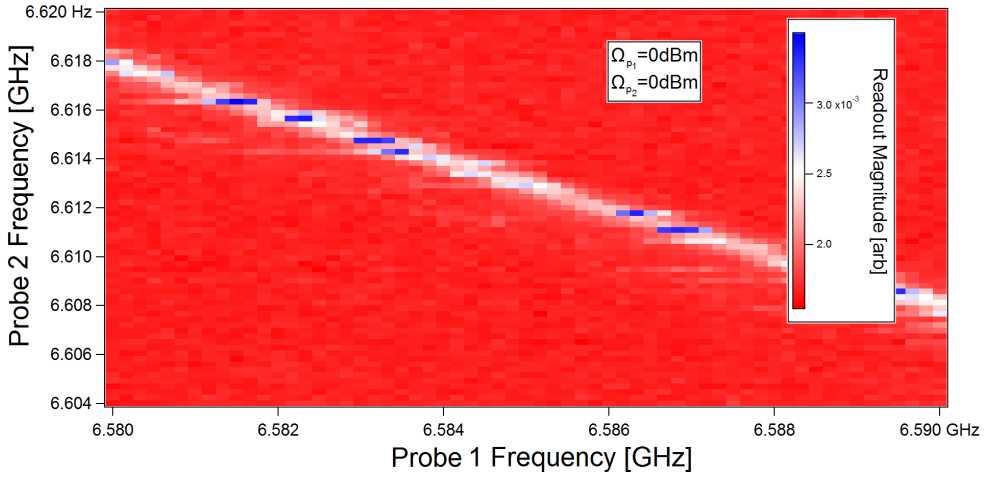

(b)

Figure 4.32: Population of $|e\rangle$ for various probe powers. **(a)** $\Omega_{p_1} = \Omega_{p_2} = 0$dBm, **(b)** $\Omega_{p_1} = -10$dBm and $\Omega_{p_2} = 0$dBm. Both figures show that the detuning of ω_{p_1} and ω_{p_2} is linear for constant Ω_{p_1} and Ω_{p_2}.

and ω_{p_1} was swept. The population of $|e\rangle$ was readout using the high-power readout scheme (Section 4.5) immediately following a 650ns ω_{p_2} pulse. To allow the system to reset between pulses, the system was allowed to relax for 198.7μs between measurements. This is much longer than the lifetime of $|e\rangle$ (27μs, see Section 4.7.2), and it can be assumed that the system will return to $|g\rangle$ within this time.

In this experiment, to gain the best signal to noise ratio of ω_{p_2}, the QS used to drive ω_{p_2} was held at 7dBm and room temperature attenuation was added to decrease Ω_{p_2}. Figure 4.33 shows the readout magnitude for (a) 21dB and **(b)** 27dB of attenuation. Using Equation 4.2, but using the power of the signal at the cavity, rather than leaving the cavity, the number of photons in the ω_{p_2} pulses are 57000 and 3700 photons respectively.

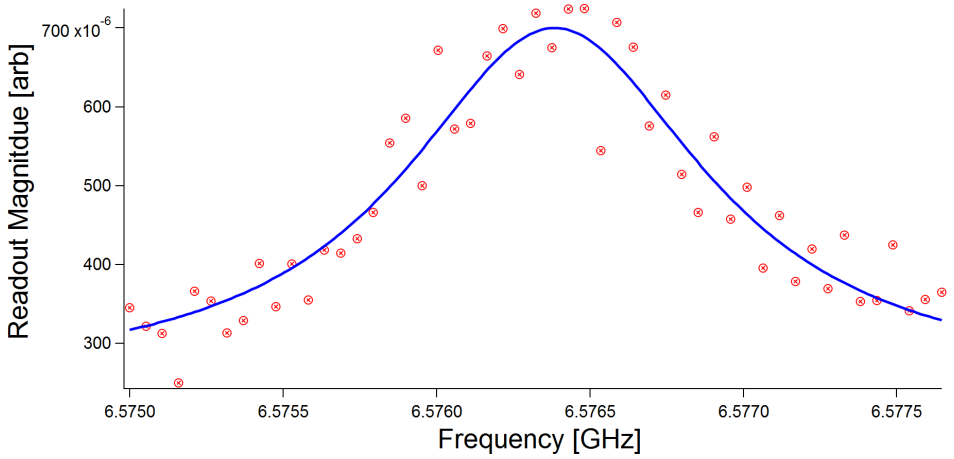

(a)

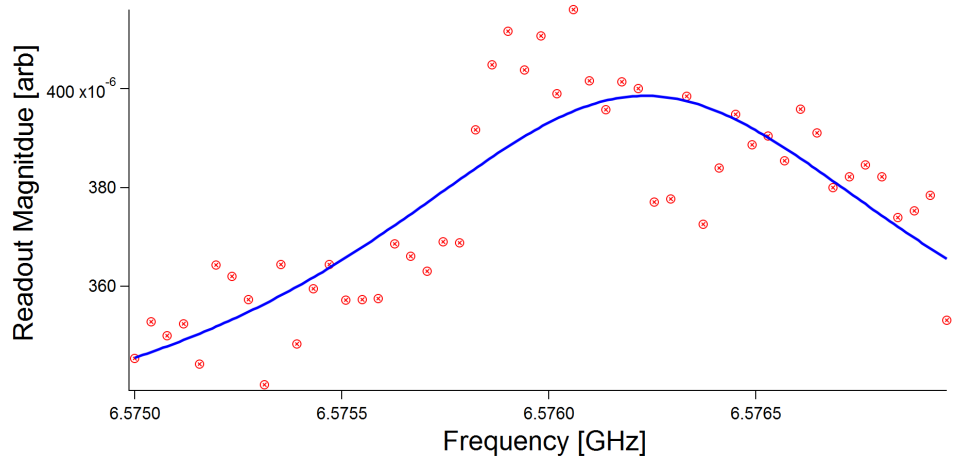

(b)

Figure 4.33: Population of $|e\rangle$ at various ω_{p_1} for small Ω_{p_2} with continuous-wave drive $\Omega_{p_1} = 5.3$dBm and $\omega_{p_2} = 6.6144$GHz. The QS suppling ω_{p_2} is held at 7dBm and **(a)** 21dB and **(b)** 27dB of room temperature atttenuation are added. ω_{p_2} is pulsed for 650ns, corresponding to pulses of (a) 57000 and (b) 3700 photons.

Chapter 5

Conclusion and Outlook

This work explored the suitability of using a qubit-cavity system as a single photon detector. Three energy levels of the combined system are used to form a lambda system. The advantage of using a superconducting system is the tunability of parameters, such as decay rates and control frequencies, that is provided through the design of both the qubit and cavity, rather than the constraints that using an atomic lambda system puts on the experiment. Using specifically a transmon as the qubit in the system forces the $|g\rangle \leftrightarrow |f\rangle$ transition to be a two-photon process.

The two-photon process allows for two separate probe drives, ω_{p_1} and ω_{p_2} to be used to excite the transition. If each of these drives is detuned from the two photon transition, on their own, they do not excite the $|g\rangle \leftrightarrow |f\rangle$ transition. This allows for ω_{p_1} to be driven constantly, and only invoking the transition when ω_{p_2} is pulsed. The $|g\rangle \leftrightarrow |f\rangle$ transition is only driven when ω_{p_2} is on, therefore no population builds in $|e\rangle$ when ω_{p_2} is on.

If ω_{p_1} and ω_{p_2} are driven with different drive strengths, Ω_{p_1} and Ω_{p_2}, the transition will still occur. With sufficiently high Ω_{p_1}, it is predicted that Ω_{p_2} can be reduced to a pulse of a single photon.

A model was developed to investigate uneven driving of ω_{p_1} and ω_{p_2}. To drive $|g\rangle \leftrightarrow |f\rangle$, the drives need to be detuned as $\Delta_{p_1} = -\Delta_{p_2}$. In the time domain, pulsing ω_{p_2} shows population building only when ω_{p_2} is on. As long as Ω_{p_1} is strong enough to obtain the maximum population of $|e\rangle$ when ω_{p_1} is not detuned, decreasing Ω_{p_2} does not change the steady state population of $|e\rangle$. Therefore, the model support the prediction that ω_{p_2} can be reduced to a single photon and still populate $|e\rangle$.

Two readout schemes were explored. The first, a low power readout scheme, uses the qubit state dependent nonlinearity in the resonant cavity frequency. The second, a high

power readout, uses nonlinearity in the cavity coupler power at which the bare cavity frequency was exposed, based on the qubit state. This second readout scheme affords an 80% contrast in the readout of the excited state and 83% for the ground state.

Protocols for lab equipment were developed in order to conduct time domain characterization of the system. These showed that the qubit had a T_1= 17μs and T_2 = 35μs.

Finally, the lambda system was explored. Using the energy levels $|g,0\rangle$, $|e,0\rangle$ and $|e,1\rangle$ of the Jaynes-Cummings ladder as the states $|g\rangle$, $|e\rangle$ and $|f\rangle$ an effective lambda system can be formed. The decay $|f\rangle \rightarrow |e\rangle$ is determined by the cavity decay rate, κ, while $|e\rangle \rightarrow |g\rangle$ is the decay of the qubit, Γ. As $\kappa = 0.25$MHz and $\kappa = 62.5$kHz, the qubit-cavity system used in experimentation meets the requirement $\kappa \gg \Gamma$.

The first indication of the presence of the lambda system was the appearance of an absorbance line in the transmission of ω_c near the $|g\rangle \leftrightarrow |e\rangle$ frequency when the $|e\rangle \leftrightarrow |f\rangle$ transition was driven with ω_p. The absorbence line was an indication that the quantum transition amplitudes of ω_p and ω_c are interfering producing DIT. The shift in the absorbence line with ω_c and ω_p agreed with the two probe drive theory developed for this experiment.

The use of a transmon means that the $|g\rangle \leftrightarrow |f\rangle$ is a two photon transition. This provides the opportunity to use two photons of different frequencies and drive strengths to excite the probe transition. Looking at detuning the two photon drive it was determined that the frequencies could be detuned linearly in opposite directions (one positively and one negatively) from the two photon transition.

The readout of the excited state was critical in probing the system. If the transmission of a continuous-wave drive at $\omega_{cav} - \chi$, which is equal to the transition frequency of $|e\rangle \leftrightarrow |f\rangle$, was monitored then $|e\rangle$ only had a coherence time on the order of the cavity, $\sim 3\mu$s. This indicated that the lambda system was decaying through $|f\rangle \rightarrow |g\rangle$ instead of $|e\rangle \rightarrow |g\rangle$, as desired, since $|f\rangle \leftrightarrow |g\rangle$ was dominated by κ. If, instead, $\omega_{cav} + \chi$ was used, the coherence time of $|e\rangle$ increased to $\sim$ 27μs. This indicated the system was decaying through the desired channel, $|e\rangle \rightarrow |g\rangle$, and the probing has minimal effect on the state system.

This indicates that the system could be used as a transistor for two different $\omega_{control}$, $\omega_{cav} \pm \chi$. The transmission of $\omega_{cav} \pm \chi$ would decrease (increase) when ω_{p_2} is turned on. Although the change in transmission happens quite quickly when ω_{p_2} is turned on, the changed state of the transitor differs depending on which frequency is being controlled. This is because the decay of $|e\rangle$ differs, as described above. $\omega_{control} = \omega_{cav} + \chi$ would decay with a decay rate similar to Γ, while $\omega_{control} = \omega_{cav} - \chi$ would return to steady state with the decay rate of the cavity, which is a much shorter time.

Although the decay time of the change in the transmission of $\omega_{control} = \omega_{cav} + \chi$ was much longer than that of $\omega_{control} = \omega_{cav} - \chi$, the gain of the system considerably larger for $\omega_{control} = \omega_{cav} - \chi$. For $\omega_{control} = \omega_{cav} - \chi$ a ω_{p_2} pulse of 109 thousand photons caused a change of 9 billion photons in $\omega_{control}$, a gain of ~ 83 thousand $^{\text{photons}}/_{\text{photon}}$. For $\omega_{control} = \omega_{cav} + \chi$ only a gain of $5^{\text{photons}}/_{\text{photon}}$ was achieved: a ω_{p_2} pulse of 11 million photons caused a change of 58 million photons in $\omega_{control}$.

For constant power the detuning was linear, but the sum of the probe drive frequencies was dependent on the powers of the two drives, especially for high power drive. The frequency of the low power probe was shown to be dependent on the drive amplitude as $f = 6.584 \pm 0.00018 - (6.7023 \pm 2.5) \times 10^{-4} P - (7.8877 \pm 0.743) \times 10^{-4} P^2$, where P is the amplitude of the lower power probe drive.

Lastly, it was investigated how low ω_{p_2} could be and still excite the $|g\rangle \leftrightarrow |f\rangle$ transition. A 650ns pulse of one of the probe drives was applied while driving the second probe drive at 0dBm. This lead to pulses of 57000 and 3700 photons producing loading of $|e\rangle$

Although the direct control of the transmission of $\omega_{control} = \omega_{cav} + \chi$ or $\omega_{cav} - \chi$ could not be shown, it is expected with less noisy microwave sources and quantum-limited amplification, such as a parametric amplifier, could be used to demonstrate this.

The qubit-cavity lambda system proved to be predictable and controllable, although measurements of pulses at lower powers did not show clear excitation of the transition, despite millions of averages and long measurement times. The introduction of quantum amplifiers, such as a parametric amplifier, could help in obtaining results in the few to single photon regime.

The system shows promise to be able to reach the single photon regime. With further investigation in the effects of various parameters on the system such as the qubit-cavity coupling, g, the ratio of decay rates, and the coupling of the cavity to the transmission line, the lambda system could be fine tuned to numerous applications. These parameters, especially the couplings, may create a lower bound on the number of photons needed to control the $|g\rangle \leftrightarrow |f\rangle$ transition.

Single photon transistors or single photon detectors are possible uses for this system in the future.

References

[1] GAML Alzetta, A Gozzini, L Moi, and G Orriols. An experimental method for the observation of rf transitions and laser beat resonances in oriented na vapour. *Il Nuovo Cimento B (1971-1996)*, 36(1):5–20, 1976.

[2] Gerardo Alzetta. Induced transparency. *Physics Today*, 50(7):36, 1997.

[3] Axel Andre, M Bajcsy, D E Chang, AS Zibrov, and M F Lukin. Stationary pulses of light in an atomic medium. In *Nonlinear Optics: Materials, Fundamentals and Applications*, page TuD3. Optical Society of America, 2004.

[4] N.W. Ashcroft and N.D. Mermin. *Solid State Physics*. HRW international editions. Holt, Rinehart and Winston, 1976.

[5] J Banuchandar and D Uthirapathi. Single photon transistor. In *Information Communication and Embedded Systems (ICICES), 2014 International Conference on*, pages 1–5. IEEE, 2014.

[6] J. Bardeen, L. N. Cooper, and J. R. Schrieffer. Theory of superconductivity. *Phys. Rev.*, 108:1175–1204, Dec 1957.

[7] J. G. Bednorz and K. A. Müller. Possible hightc superconductivity in the balacuo system. *Zeitschrift für Physik B Condensed Matter*, 64(2):189–193, Jun 1986.

[8] Lev S Bishop, JM Chow, Jens Koch, AA Houck, MH Devoret, E Thuneberg, SM Girvin, and RJ Schoelkopf. Nonlinear response of the vacuum rabi resonance. *Nature Physics*, 5(2):105–109, 2009.

[9] K.-J. Boller, A. Imamoğlu, and S. E. Harris. Observation of electromagnetically induced transparency. *Phys. Rev. Lett.*, 66:2593–2596, May 1991.

[10] Vincent Bouchiat, D Vion, Ph Joyez, D Esteve, and MH Devoret. Quantum coherence with a single cooper pair. *Physica Scripta*, 1998(T76):165, 1998.

[11] M Brune, F Schmidt-Kaler, A Maali, J Dreyer, E Hagley, JM Raimond, and S Haroche. Quantum rabi oscillation: A direct test of field quantization in a cavity. *Physical Review Letters*, 76(11):1800, 1996.

[12] D Budker, DF Kimball, SM Rochester, and VV Yashchuk. Nonlinear magneto-optics and reduced group velocity of light in atomic vapor with slow ground state relaxation. *Physical review letters*, 83(9):1767, 1999.

[13] M Büttiker. Zero-current persistent potential drop across small-capacitance josephson junctions. *Physical Review B*, 36(7):3548, 1987.

[14] Darrick E Chang, Anders S Sørensen, Eugene A Demler, and Mikhail D Lukin. A single-photon transistor using nanoscale surface plasmons. *Nature Physics*, 3(11):807–812, 2007.

[15] I Chiorescu, Y Nakamura, CJP Ma Harmans, and JE Mooij. Coherent quantum dynamics of a superconducting flux qubit. *Science*, 299(5614):1869–1871, 2003.

[16] Leon N Cooper. Bound electron pairs in a degenerate fermi gas. *Physical Review*, 104(4):1189, 1956.

[17] Michel H Devoret et al. Quantum fluctuations in electrical circuits. *Les Houches, Session LXIII*, 7(8), 1995.

[18] Paul Adrien Maurice Dirac. A new notation for quantum mechanics. In *Mathematical Proceedings of the Cambridge Philosophical Society*, volume 35, pages 416–418. Cambridge University Press, 1939.

[19] G Falci, A La Cognata, M Berritta, A DArrigo, E Paladino, and B Spagnolo. f. *Physical Review B*, 87(21):214515, 2013.

[20] Michael Fleischhauer, Atac Imamoglu, and Jonathan P Marangos. Electromagnetically induced transparency: Optics in coherent media. *Reviews of modern physics*, 77(2):633, 2005.

[21] Jay Gambetta, Alexandre Blais, David I Schuster, Andreas Wallraff, L Frunzio, J Majer, Michel H Devoret, Steven M Girvin, and Robert J Schoelkopf. Qubit-photon interactions in a cavity: Measurement-induced dephasing and number splitting. *Physical Review A*, 74(4):042318, 2006.

[22] Jay Gambetta, WA Braff, A Wallraff, SM Girvin, and RJ Schoelkopf. Protocols for optimal readout of qubits using a continuous quantum nondemolition measurement. *Physical Review A*, 76(1):012325, 2007.

[23] Erwin L Hahn. Spin echoes. *Physical review*, 80(4):580, 1950.

[24] Lene Vestergaard Hau, Stephen E Harris, Zachary Dutton, and Cyrus H Behroozi. Light speed reduction to 17 metres per second in an ultracold atomic gas. *Nature*, 397(6720):594, 1999.

[25] HyperPhysics. Fermi energies, solid properties. `http://hyperphysics.phy-astr.gsu.edu/hbase/Tables/fermi.html`. (Accessed on 07/04/2017).

[26] Kunihiro Inomata, Zhirong Lin, Kazuki Koshino, William D Oliver, Jaw-Shen Tsai, Tsuyoshi Yamamoto, and Yasunobu Nakamura. Single microwave-photon detector using an artificial [lambda]-type three-level system. *Nature communications*, 7, 2016.

[27] Hoi Ion-Chun. *Quantum Optics with Propagating Microwaves in Superconducting Circuits*. PhD thesis, Chalmers University of Technology, 2013.

[28] JR Johansson, PD Nation, and Franco Nori. Qutip: An open-source python framework for the dynamics of open quantum systems. *Computer Physics Communications*, 183(8):1760–1772, 2012.

[29] Brian David Josephson. Possible new effects in superconductive tunnelling. *Physics letters*, 1(7):251–253, 1962.

[30] Brian Julsgaard, Jacob Sherson, J Ignacio Cirac, Jaromír Fiurášek, and Eugene S Polzik. Experimental demonstration of quantum memory for light. *Nature*, 432(7016):482–486, 2004.

[31] P. Kaye, R. Laflamme, and M. Mosca. *An Introduction to Quantum Computing*. Oxford University Press, 2007.

[32] Sumanta Khan, Molahalli Panidhara Kumar, Vineet Bharti, and Vasant Natarajan. Coherent population trapping (cpt) versus electromagnetically induced transparency (eit). *The European Physical Journal D*, 71(2):38, 2017.

[33] Jacob B Khurgin. Slow light in various media: a tutorial. *Advances in Optics and Photonics*, 2(3):287–318, 2010.

[34] Jens Koch, M Yu Terri, Jay Gambetta, Andrew A Houck, DI Schuster, J Majer, Alexandre Blais, Michel H Devoret, Steven M Girvin, and Robert J Schoelkopf. Charge-insensitive qubit design derived from the cooper pair box. *Physical Review A*, 76(4):042319, 2007.

[35] A Kocharovskaya and Ya I Khanin. Population trapping and coherent bleaching of a three-level medium by a periodic train of ultrashort pulses. *Zh. Eksp. Teor. Fiz*, 90:1610–1618, 1986.

[36] Yuimaru Kubo. Quantum engineering: Turn to the dark side. *Nature Physics*, 12:21–22, 2016.

[37] Henry G Leduc, Bruce Bumble, Peter K Day, Byeong Ho Eom, Jiansong Gao, Sunil Golwala, Benjamin A Mazin, Sean McHugh, Andrew Merrill, David C Moore, et al. Titanium nitride films for ultrasensitive microresonator detectors. *Applied Physics Letters*, 97(10):102509, 2010.

[38] H Malissa, DI Schuster, AM Tyryshkin, AA Houck, and SA Lyon. Superconducting coplanar waveguide resonators for low temperature pulsed electron spin resonance spectroscopy. *Review of scientific instruments*, 84(2):025116, 2013.

[39] B.R. Johnson L. Sun D.I. Schuster L. Frunzio R.J Schoelkopf M.D. Reed, L. DiCarlo. High-fidelity readout in circuit quantum electodynamics using the jaynes-cummings nonlinearity. *Physical Review Letter*, 105, 2010.

[40] Saul Meiboom and David Gill. Modified spin-echo method for measuring nuclear relaxation times. *Review of scientific instruments*, 29(8):688–691, 1958.

[41] Yasunobu Nakamura, Yu A Pashkin, and JS Tsai. Coherent control of macroscopic quantum states in a single-cooper-pair box. *nature*, 398(6730):786–788, 1999.

[42] S Novikov, T Sweeney, JE Robinson, SP Premaratne, B Suri, FC Wellstood, and BS Palmer. Raman coherence in a circuit quantum electrodynamics lambda system. *Nature Physics*, 12(1):75, 2016.

[43] T.P. Orlando and K.A. Delin. *Foundations of Applied Superconductivity*. Electrical Engineering Series. Addison-Wesley, 1991.

[44] DF Phillips, A Fleischhauer, A Mair, RL Walsworth, and Mikhail D Lukin. Storage of light in atomic vapor. *Physical Review Letters*, 86(5):783, 2001.

[45] D.M. Pozar. *Microwave Engineering*. Wiley, 2004.

[46] Isidor Isaac Rabi. Space quantization in a gyrating magnetic field. *Physical Review*, 51(8):652, 1937.

[47] Norman F Ramsey. A molecular beam resonance method with separated oscillating fields. *Physical Review*, 78(6):695, 1950.

[48] Chad Rigetti, Jay M Gambetta, Stefano Poletto, BLT Plourde, Jerry M Chow, AD Córcoles, John A Smolin, Seth T Merkel, JR Rozen, George A Keefe, et al. Superconducting qubit in a waveguide cavity with a coherence time approaching 0.1 ms. *Physical Review B*, 86(10):100506, 2012.

[49] C. H. Townes S. H. Aulters. Stark effect in rabidly varying fields. *Physical Review*, 100, 1955.

[50] Martin Sandberg, Michael R Vissers, Jeffrey S Kline, Martin Weides, Jiansong Gao, David S Wisbey, and David P Pappas. Etch induced microwave losses in titanium nitride superconducting resonators. *Applied Physics Letters*, 100(26):262605, 2012.

[51] R.J. Scherrer. *Quantum Mechanics: An Accessible Introduction*. Benjamin Cummings, 2006.

[52] JA Schreier, Andrew A Houck, Jens Koch, David I Schuster, BR Johnson, JM Chow, Jay M Gambetta, J Majer, L Frunzio, Michel H Devoret, et al. Suppressing charge noise decoherence in superconducting charge qubits. *Physical Review B*, 77(18):180502, 2008.

[53] DI Schuster, Andreas Wallraff, Alexandre Blais, L Frunzio, R-S Huang, J Majer, SM Girvin, and RJ Schoelkopf. ac stark shift and dephasing of a superconducting qubit strongly coupled to a cavity field. *Physical Review Letters*, 94(12):123602, 2005.

[54] A.S. Sedra and K.C. Smith. *Microelectronic Circuits*. Oxford Series in Electrical an. Oxford University Press, 2014.

[55] Vibhor Singh, Ben H Schneider, Sal J Bosman, Evert PJ Merkx, and Gary A Steele. Molybdenum-rhenium alloy based high-q superconducting microwave resonators. *Applied Physics Letters*, 105(22):222601, 2014.

[56] J Solyom. The fermi gas model of one-dimensional conductors. *Advances in Physics*, 28(2):201–303, 1979.

[57] Michael R Vissers, Jiansong Gao, David S Wisbey, Dustin A Hite, Chang C Tsuei, Antonio D Corcoles, Matthias Steffen, and David P Pappas. Low loss superconducting titanium nitride coplanar waveguide resonators. *Applied Physics Letters*, 97(23):232509, 2010.

[58] Edo Waks and Jelena Vuckovic. Dipole induced transparency in drop-filter cavity-waveguide systems. *Physical review letters*, 96(15):153601, 2006.

[59] Edo Waks and Jelena Vuckovic. Dispersive properties and large kerr nonlinearities using dipole-induced transparency in a single-sided cavity. *Physical Review A*, 73(4):041803, 2006.

[60] Christopher M Walker and James A Bankson. A bloch-mcconnell simulator with pharmacokinetic modeling to explore accuracy and reproducibility in the measurement of hyperpolarized pyruvate. In *SPIE Medical Imaging*, pages 94170B–94170B. International Society for Optics and Photonics, 2015.

[61] Ying Wu and Xiaoxue Yang. Strong-coupling theory of periodically driven two-level systems. *Phys. Rev. Lett.*, 98:013601, Jan 2007.

APPENDICES

Appendix A

Example Theoretical Python Code

Example code for theoretical simulation is seen here. The code is written in Python and relies on the Qutip package [28] for quantum simulations.

A.1 Single Probe Drive

The Python code for simulations in Section 3.1 is shown in this section. Different simulations were run by changing the parameters that were swept.

```
import matplotlib.pyplot as plt
import numpy as np

from qutip import *

def ham(delta_c,delta_p,Omega_c,Omega_p,chi,kappa,gamma):
        N = 8

        g = basis(2,0)
        e = basis(2,1)

        H = ( delta_c    2 * chi) * tensor(g*g.dag(),num(N))  \
            delta_p * tensor(e*e.dag(),qeye(N))    delta_c * \
            tensor(e*e.dag(),num(N))    delta_c * \
            tensor(e*e.dag(),qeye(N)) + Omega_c/2 * \
            tensor(e*e.dag(),create(N)) + Omega_p/2 * \
```

```
            tensor(create(2),create(N)) + Omega_c/2 * \
            tensor(e*e.dag(),destroy(N)) + Omega_p/2 * \
            tensor(destroy(2),destroy(N))

        p_1 = tensor(qeye(2),destroy(N))*np.sqrt(kappa)
        p_2 = tensor(destroy(2),qeye(N))*np.sqrt(gamma)
        return H, [p_1,p_2,]


def run():
        N = 10
        M = 10
        e_pop = np.zeros([N,M])
        chi =  4.1 * 2 * np.pi
        delta_p = np.linspace( 30 * 2 * np.pi, 30 * 2 * np.pi, N+1)
        delta_c = np.linspace( 30 * 2 * np.pi, 30 * 2 * np.pi, N+1)
        Omega_p = 4 * 2 * np.pi
        Omega_c = 5 * 2 * np.pi
        kappa = 2.9 * 2 * np.pi
        gamma = 0.04 * 2 * np.pi
        nq = destroy(2)
        mq = nq.dag() * nq
        print(mq)

        for i in range(N):
                print(i)
                for j in range(M):
                        H, c_op_list = ham(delta_p[j],delta_c[i],
                             Omega_p,Omega_c,chi,kappa,gamma)
                        result = steadystate(H,c_op_list)
                        e_pop[j,i] = expect(mq,ptrace(result,0))

        fig, ax = plt.subplots(figsize=(10,10))
        np.savetxt('detuning_Ap5_Oc400_test.txt',
            e_pop,fmt='%f',delimiter=',')
        p = ax.pcolor(np.linspace( 30,30,N+1),
            np.linspace( 30,30,M+1), e_pop, edgecolors='none')
        p.set_cmap('RdYlBu_r')
        ax.set_ylabel(r'$\Delta_p/\omega$', fontsize=20)
        ax.set_xlabel(r'$\Delta_c/\omega$', fontsize=20)
```

```
        ax.axis('tight')
        ax.set_title(
            'Excitation probabilty of qubit, in steady state',
            fontsize=16)
        plt.colorbar(p)
        plt.show()

if __name__ == '__main__':
    run()
```

A.2 Two Probe Drives

The following is an example of Python code used for theoretical simulations for Section 3.2. This example sweeps the drive strength and frequency of one of the probe drives and holds the other constant. Other simulations were done using similar code, changing which variables were swept in the loop.

```
import matplotlib.pyplot as plt
import numpy as np

from qutip import *

def ham(Omega_p_1, Omega_p_2, Omega_p, kappa, gamma, wge, we10, wc1, wc2, wp):


        H0 = Qobj([[we10 wp, 0, 0],
                   [0, (wge+we10) ((wc1+wc2)/2+wp), 0],
                   [0, 0, wge (wc1+wc2)/2]])
        Hc1m = Omega_p_1/2 * Qobj([[0, 1, 0], [0, 0, 0], [0, 0, 0]])
        Hc1p = Omega_p_1/2 * Qobj([[0, 0, 0], [1, 0, 0], [0, 0, 0]])
        Hc2m = Omega_p_2/2 * Qobj([[0, 1, 0], [0, 0, 0], [0, 0, 0]])
        Hc2p = Omega_p_2/2 * Qobj([[0, 0, 0], [1, 0, 0], [0, 0, 0]])
        Hpm = Omega_p * Qobj([[0, 0, 0], [0, 0, 1], [0, 0, 0]])
        Hpp = Omega_p * Qobj([[0, 0, 0], [0, 0, 0], [0, 1, 0]])


        #collapse operators (decay rates)
        p_1 = Qobj([[0, 0, 0], [0, 0, 1], [0, 0, 0]])*(gamma)
        p_2 = Qobj([[0, 1, 0], [0, 0, 0], [0, 0, 0]])*(kappa)
```

```
        return H0, Hp1m, Hp1p, Hp2m, Hp2p, Hcm, Hcp, [p_1,p_2]

# add time dependence
def hamiltonian_t(t,args):
        return (args['H0'] + args['Hc1m'] *
            np.exp(1j * 0.5 * (args['wp1'] * t)) *
            np.exp( 1j * (args['wp2'] * t) / 2) + args['Hp1p'] *
            np.exp( 1j * 0.5 * args['wp1'] * t) * np.exp(1j *
            (args['wp2'] * t) / 2) + args['Hp2m'] *
            np.exp(1j * 0.5 * args['wp2'] * t) *
            np.exp( 1j * (args['wp1'] * t) / 2) +
            args['Hp2p'] * np.exp( 1j * 0.5 * args['wp2'] * t) *
            np.exp( 1j * (args['wp1'] * t) / 2) + args['Hcm'] +
            args['Hcp']


def run():
        options = Options()
        options.nsteps = 500000
        print(options)

        N = 201
        M = 101

        g0 = np.zeros([M,N])
        e0 = np.zeros([M,N])
        e1 = np.zeros([M,N])

        Omega_p1 = np.linspace(0.0e 3,0.1e 3,M)
        Omega_p2 = 0.2e 3
        Omega_c = 0e 3 * 2 * np.pi
        kappa = 62.5e 6 * 2 * np.pi
        gamma = 250e 6 * 2 * np.pi
        wge = (7.0786e0 * 2 * np.pi + 6.12142e0 * 2 * np.pi)/2
        we10 = 7.0786e0 * 2 * np.pi
        wp1 = np.linspace(wge (1e 3*2*np.pi),wge+(1e 3*2*np.pi),N)
        wp2 = wge (0.0e 3*2*np.pi)
        wc = 0

        state_g0 = Qobj([[1,0,0],[0,0,0],[0,0,0]])
```

```
state_e0 = Qobj([[0,0,0],[0,1,0],[0,0,0]])
state_e1 = Qobj([[1,0,0],[0,0,0],[0,0,0]])

T = 0.01 #time to solve operator over,
#works best if it changes with the drive frequency 2 * np.pi
for i in range(N):
        print(i)
        for j in range(M):

                H0, Hp1m, Hp1p, Hp2m, Hp2p, Hcm, Hcp, \
                    c_op_list = ham(Omega_p1[j],Omega_p2,
                    Omega_c,kappa,gamma,wge,we10,
                    wp1[i],wp2,wc)
            #returns the components for H and the states
                args = {'H0':H0,'Hp1m':Hp1m,'Hp1p':Hp1p,
                    'wp1':wp1[i],'Hp2m':Hp2m,'Hp2p':Hp2p,
                    'Hcm':Hcm,'Hcp':Hcp,'wp2':wp2,'wc':wc}
                #args for the time dependent hamiltonian

                U = propagator(hamiltonian_t,T,c_op_list,args)
                #get the propagator
                rho_ss = propagator_steadystate(U)
                #steady state

                rho_ss_diag = np.real(rho_ss.diag())

                g0[j,i] = abs(expect(state_g0,rho_ss.unit()))
                e0[j,i] = abs(expect(state_e0,rho_ss.unit()))
                e1[j,i] = abs(expect(state_e1,rho_ss.unit()))

np.savetxt('sweep_wp_wp_g0.txt',g0,fmt='%f',delimiter=',')
np.savetxt('sweep_wp_wp_e0.txt',e0,fmt='%f',delimiter=',')
np.savetxt('sweep_wp_wp_e1.txt',e1,fmt='%f',delimiter=',')


fig, ax = plt.subplots(figsize=(10,10))
p = ax.pcolor(wp1/2/np.pi, Omega_p1/2/np.pi,
    g0,edgecolors='none')
p.set_cmap('RdYlBu_r')
ax.set_ylabel(r'$\Omega_{p}/2\pi$', fontsize=20)
```

```
        ax.set_xlabel(r'$\omega_{p1}/2\pi$', fontsize=20)
        ax.axis('tight')
        ax.set_title(r'Darkstate_of_$\left|g0\right>$', fontsize=16)
        plt.colorbar(p)
        plt.show()


        fig, ax = plt.subplots(figsize=(10,10))
        p = ax.pcolor(wc1/2/np.pi, Omega_p1/2/np.pi,
        e0,edgecolors='none')
        p.set_cmap('RdYlBu_r')
        ax.set_ylabel(r'$\Omega_{p}/2\pi$', fontsize=20)
        ax.set_xlabel(r'$\omega_{p1}/2\pi$', fontsize=20)
        ax.axis('tight')
        ax.set_title(r'Darkstate_of_$\left|e0\right>$', fontsize=16)
        plt.colorbar(p)
        plt.show()



        fig, ax = plt.subplots(figsize=(10,10))
        p = ax.pcolor(wc1/2/np.pi, Omega_p1/2/np.pi,
            e1,edgecolors='none')
        p.set_cmap('RdYlBu_r')
        ax.set_ylabel(r'$\Omega_{p}/2\pi$', fontsize=20)
        ax.set_xlabel(r'$\omega_{p1}/2\pi$', fontsize=20)
        ax.axis('tight')
        ax.set_title(r'Darkstate_of_$\left|e1\right>$', fontsize=16)
        plt.colorbar(p)
        plt.show()



if __name__ == '__main__':
    run()
```

A.3 Two Probe Drive Time Domain

The code in this section was used to simulate the time dynamics of two probe drives. Here, ω_{p_2} is pulsed from 15μ to 30μ.

```
import matplotlib.pyplot as plt
import numpy as np

from qutip import *

def ham(kappa,gamma,wge,we10,wp1,wp2,wc,N):


        g = basis(2,0)
        e = basis(2,1)

        zero = basis(N,0)

        psi0 = tensor(g*g.dag(),zero*zero.dag())

        delta_c = wc we10
        delta_p = (wp1+wp2)/2 wge

        #matrix elements for Hamiltonian
        H0 = ( delta_c) * tensor(g*g.dag(),num(N))  + \\
             delta_c * tensor(e*e.dag(),num(N))    delta_c \\
        * tensor(e*e.dag(),qeye(N))
        Hpm = tensor(create(2),create(N))
        Hpp = tensor(destroy(2),destroy(N))
        Hcp = tensor(e*e.dag(),destroy(N))
        Hcm = tensor(e*e.dag(),create(N))
        Dc = tensor(e*e.dag(),qeye(N))

        #collapse operators (decay rates)
        p_1 = tensor(destroy(2),qeye(N))*np.sqrt(gamma)
        p_2 = tensor(qeye(2),destroy(N))*np.sqrt(kappa)
        return H0, Dc, Hpm, Hpp, Hcp, Hcm, [p_1,p_2], psi0

# Time dependent coefficients for Hamiltonian
def Hpm1_coeff(t,args):
```

```
        if (t < 15000 or t > 30000):
                return args['Op1']
        else:
                return np.exp(1j * 0.5 * args['wp1'] * t)\\
                    * np.exp( 1j * 0.5 * args['wp2'] * t) * args['Op1']

def Hpp1_coeff(t,args):
        if (t < 15000 or t > 30000):
                return args['Op1']
        else:
                return np.exp( 1j * 0.5 * args['wp1'] * t) \\
                    * np.exp(1j * 0.5 * args['wp2'] * t) * args['Op1']

def Hpm2_coeff(t,args):
        if (t < 15000 or t > 30000):
                return 0
        else:
                return  np.exp(1j * 0.5 * args['wp2'] * t) \\
                    * np.exp( 1j * 0.5 * args['wp1'] * t) * args['Op2']

def Hpp2_coeff(t,args):
        if (t < 15000 or t > 30000):
                return 0
        else:
                return np.exp( 1j * 0.5 * args['wp2'] * t) \\
                    * np.exp(1j * 0.5 * args['wp1'] * t) * args['Op2']

def Hcp_coeff(t,args):
        return args['Oc']

def Hcm_coeff(t,args):
        return args['Oc']

def Dc_coeff(t,args):
        if (t < 15000 or t > 30000):
                return  1*((args['wc1']) args['wge'])
        else:
                return  1*((args['wc1']+args['wc2'])/2 args['wge'])
```

```
def run():
        N = 301
        M = 301
        e_pop = np.zeros([M,N])

        Omega_p1 = 1*1e 3*2*np.pi
        Omega_p2 = 0.01*1e 3*2*np.pi
        Omega_c = 0
        kappa = 250e 6 * 2 * np.pi
        gamma = 62.5e 6 * 2 * np.pi
        wge = (7.0786e0 * 2 * np.pi + 6.12142e0 * 2 * np.pi)/2
        we10 = 7.0786e0 * 2 * np.pi
        wc = we10
        wp1 = wge+(5*1e 3*2*np.pi)
        wp2 = wge (5*1e 3*2*np.pi)

        nq = destroy(2)
        mq = nq.dag() * nq
        rq = tensor(mq, qeye(2))

        tfinal = 45000
        tlist=np.linspace(0,tfinal,30000)

        fig, ax = plt.subplots(figsize=(10,10))

        H0, Dc, Hpm, Hpp, Hcp, Hcm, c_op_list, psi0 = \\
            ham(kappa,gamma,wge,we10,wc1,wc2,wp,2)
            #returns the components for H and the states
        args = {'H0':H0,'Op1':Omega_p1/2,'Op2':Omega_p2/2,'wp1':wp1,\\
             'Oc':Omega_c/2,'wp2':wp2,'wc':wc,'Hpm':Hpm,'Hpp':Hpp,\\
             'Hcp':Hcp,'Hcm':Hcm,'wge':wge,'Dc':Dc}
            #args for the time dependent hamiltonian
        H = [H0,[Hcp,Hcp_coeff],[Hcm,Hcm_coeff],[Hpm,Hpm2_coeff],\\
             [Hpp,Hpp2_coeff],[Hpm,Hpm1_coeff],[Hpp,Hpp1_coeff],\\
                  [Dc,Dc_coeff]]#[1,hamiltonian_t]]
        H2 = H0 + Omega_p2/1 * (Hpm + Hpp) + Omega_p2/2 * (Hpm + Hpp) + Dc

        output = mesolve(H,psi0,tlist,c_op_list,[rq,Hpm*Hpp],\\
            args=args,progress_bar=True)
```

```
        plt.plot(tlist/1e3,np.real(output.expect[0]),linewidth=3.0)

        ax.set_ylim([0,1])
        ax.set_xlim([0,tfinal/1e3])
        ax.set_ylabel('Excited state population', fontsize=20)
        ax.set_xlabel(r'Time [$\mu$s]', fontsize=20)

        plt.show()

if __name__ == '__main__':
    run()
```

Appendix B

Experimental Microwave Equipment Setups

The Bluefors dilution refrigerator was wired with 4 lines during experimentation. Two of these lines were used for this experiment: lines A (input) and C (output). The room temperature amplifier has an amplification of 26dB.

The microwave signal was fed into the output of the splitters, to use them as adders.

B.1 Spectroscopy and Punchout

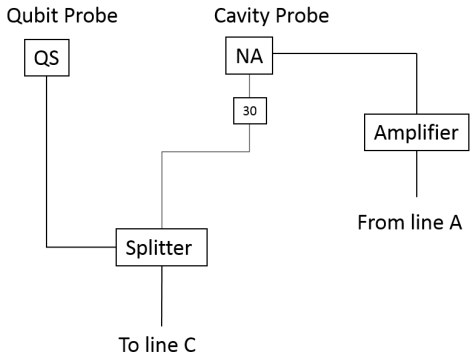

Figure B.1: Experimental setup for spectroscopy and punchout scans. The setup uses a vector network analyzer (NA) as well as a QuickSyn microwave source (QS).

B.2 Time Domain and Two Pulse Readout

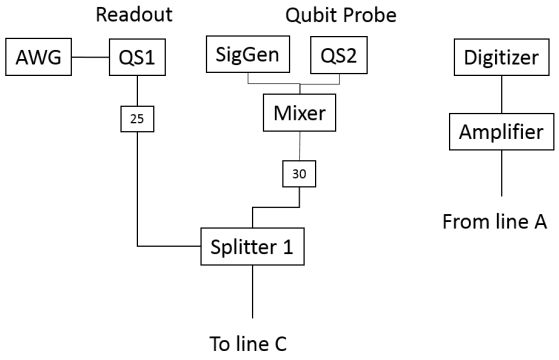

Figure B.2: Experimental setup for qubit readout during time domain measurements. Two Quicksyns are used. The first of which uses pulse modulation; the length of the on state is determined by the pulse length of a 4V DC pulse delivered by the arbitrary waveform generator (AWG). The signal generator (SigGen) is unable to be used above 6GHz and so is mixed with a 4GHz signal from the second QS to achieve signals above 6GHz.

B.3 Two Photon Drive

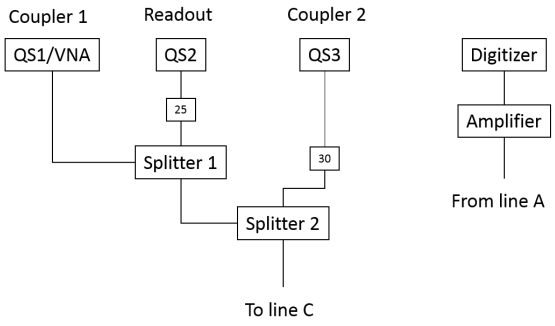

Figure B.3: Equipment setup for measurements in Section 4.7.3. Probe 1 is the high powered probe. The VNA was used for the initial detuning experiments (Figure 4.28), while QS1 was used for experiments in the rest of Section 4.7.3. QS2 is used for for qubit state readout.

B.4 Low Power Probe

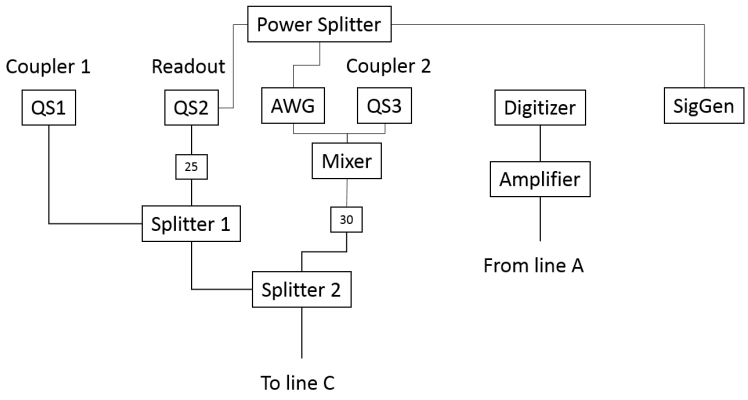

Figure B.4: Equipment setup for measurements in Section 4.7.4. Three QuickSyns (QS) are used. The first and third QS are the high power and low power probe drives, respectively. The second QS is used for state readout. The SigGen is used to pulse QS2 for the square pulse. The square pulse output is also used as a trigger for the AWG. A power splitter is used to split the signal from the SigGen to QS2 and the AWG.

Appendix C

Singal Isolation

Noise experiments were completed to determine the signal isolation through the system setup in Figure C.1 and to ensure the mixer was not allowing the frequencies from QS3 or the SigGen to bleed through. The experiment was conducted with a 5MHz sampling frequency. The experiment reports the peak power (the power at the tested frequency) and the total power seen in the 5MHz band around that power (total power). The microwave sources were setup as follows:

- QS1: 7.08GHz at 10dBm
- QS2: 6.588733333GHz at 10dBm
- QS3: 4GHz at 7dBm
- SigGen: 2.60966666GHz at 7dBm

The digitizer was inserted after the the cable to the next piece of equipment, after any attenuation shown, to account for losses and noise in the cabling.

It can be seen in Table C.1 that most of the power is at the desired frequency and hence the signal is adequately isolated. It can also be seen that there is only $\sim$ 3dB attenuation from each of the splitters. The signals input into the mixer from QS3 and the SigGen (4GHz and 2.60966666GHz, respectively) are highly attenuated out of the mixer, providing good isolation of the desired signal.

This experiment was also used to estimate the number of photons in each pulse in Section 4.7.4.

Location (After...)	**Centre Frequency (GHz)**	**Peak power (dBm)**	**Maximum Power (dBm)**
QS1	7.08	6.59409	6.60794
QS2	6.588733333	7.36517	7.38119
QS3	4	5.28024	5.28293
SigGen	2.60966666	4.080263	4.80411
Splitter 1	7.08	2.35324	2.56657
Splitter 1	6.588733333	-7.43008	-7.41265
Mixer	4	-67.2166	-59.2169
Mixer	2.60966666	-46.2582	-46.0067
Mixer	6.60966666	-13.2425	-11.2553
Splitter 2	6.60966666	-36.9564	-35.0273
Splitter 2	2.60966666	-68.0868	-58.4065
Splitter 2	4	-80.3608	-59.8849
Splitter 2	6.588733333	-11.4433	-11.435
Splitter 2	7.08	-1.59837	-1.59036

Table C.1: Signal power throughout equipment setup, showing good isolation of the desired frequencies. The peak power is the power of the centre frequency while the maximum power shows the total power within a 5MHz envelope around the centre frequency.

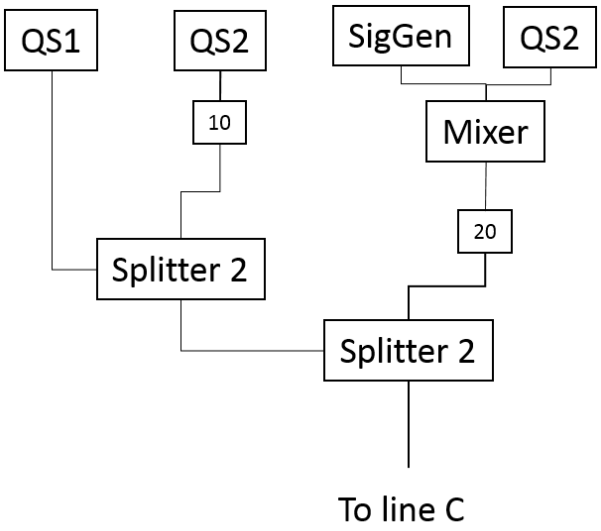

Figure C.1: Equipment setup for noise measurements. This setup is used to resemble the setups in Appendix B and to specifically test the effects of the mixer and splitters.